Design, Modelling and Control of a Modular Snake Robot with Torque Feedback for Pedal Wave Locomotion on Surfaces with Irregularities

Mohammadali Javaheri Koopaee

A thesis submitted for partial fulfilment of the degree of
Doctor of Philosophy in Mechanical Engineering
University of Canterbury
Christchurch, New Zealand

Dec 2019

Abstract

There are life forms with incredibly effective locomotion mechanisms, sensing and computation capabilities, which are invaluable sources of inspiration for researchers. One of these bio-inspired designs is snake-like robots, which their small body cross-section, intrinsic stability, manoeuvrability and hyper-redundancy make them ideal for locomotion in challenging environments. However, design, modelling and control of a snake-like robotic mechanism for effective locomotion on surfaces with irregularities is a challenging task, which requires extensive research work.

In this thesis, the design of a cost-effective modular snake robot is presented for generating pedal wave locomotion (undulatory motion in the vertical plane) on surfaces with irregularities, where the robot lifts its body parts to climb over obstacles. To design the motor torque measurement unit as a reliable and robust environmental sensing mechanism, an elastic element with the desired shape and stiffness has been designed and manufactured using easily accessible Polyurethane sheets and attached between the links and the motors to turn a conventional servo into a Series Elastic Actuator (SEA). The designed torque sensor is calibrated and the resolution and stiffness of the sensor are obtained to be $0.01 N.m$ and $1.74\ N.m.rad^{-1}$, respectively. In addition to the design of the SEAs, the snake robot modules are also designed and manufactured using cost-effective 3D printing method with Acrylonitrile Butadiene Styrene (ABS), which unlike existing snake robot designs are not equipped with wheels allows effective pedal wave locomotion on surfaces with irregularities. Experimentation results are also provided showing the effectiveness of the developed snake robot with SEAs for effective pedal wave motion generation.

Moreover, this thesis introduces the equations of motion of modular 2D snake robots moving in vertical plane employing SEAs for the first time. The kinematics of such 2D modular snake robot is presented in an efficient matrix form and the Euler-Lagrange equations have been constructed to model the robot. Moreover, using a spring-damper (Kelvin-Voigt) contact model, external contact forces, necessary for modelling pedal wave motion are taken into account, which unlike existing methods enables to model the effect of multiple contact points on surfaces with irregularities. Using the constructed model, pedal wave motion of the robot is simulated and the torque signals measured with the elastic

element from the simulation and experimentation are compared. The correlation coefficient indicating the similarity between the signals is calculated to be 83.36% showing the validity of the dynamical model. Using the simulated and the physical robot, the effect of friction on the motion of the robot is investigated, which showed that the average speed of the pedal wave is positively correlated with the friction coefficient of the surface.

Additionally, this thesis presents Local Stiffness Control strategy, which with the help of an admittance controller, enables active control of the joint stiffness to achieve adaptive, snake robot pedal wave locomotion. The effectiveness of the proposed controller in comparison to an open-loop control strategy is shown by several experiments, which demonstrates the capability of the robot to successfully climb over an obstacle with the height of more than 55% of the diameter of the snake robot modules, which was not possible with the open-loop gait based control strategy due to side instability of the robot. Moreover, to enable the snake robot to effectively use pedal wave locomotion pattern in more challenging environments, the extend Local Stiffness Control strategy, named Tail-leading Stiffness Control (TSC) strategy is also proposed, which allows propagation of the position feedback signal along the snake body. The experimental results showing the superiority of the TSC strategy compared to both open-loop controllers and the Local Stiffness Control strategy are provided, which proved that TSC strategy with the use of both position feedback between neighbouring joints and the stiffness control concept increases the side stability of the snake robot pedal wave motion. Therefore, enables the developed snake robot with SEAs to successfully use pedal wave motion to move forward in environments with multiple irregularities.

To Hanie,

My Love, My Best Friend, My Companion

Deputy Vice-Chancellor's Office
Postgraduate Research Office

UNIVERSITY OF CANTERBURY
Te Whare Wānanga o Waitaha
CHRISTCHURCH NEW ZEALAND

Co-Authorship Form

This form is to accompany the submission of any thesis that contains research reported in co-authored work that has been published, accepted for publication, or submitted for publication. A copy of this form should be included for each co-authored work that is included in the thesis. Completed forms should be included at the front (after the thesis abstract) of each copy of the thesis submitted for examination and library deposit. *Please indicate the chapter/section/pages of this thesis that are extracted from co-authored work and provide details of the publication or submission from the extract comes:*

Publication 1: Koopaee, M. J., Classens, K., Pretty, C., & Chen, X. (2019). Dynamical Modelling and Control of Modular Snake Robots with Series Elastic Actuators for Pedal Wave Locomotion on Uneven Terrain. *Journal of Mechanical Design*, (Accepted).

- The materials in Chapter 4, are presented from this publication. Chapter 5, particularly section 5.5 includes the presented experimentation results in this publication.

Publication 2: Koopaee, M. J., Bal, S., Pretty, C., & Chen, X. (2019). Design and Development of a Wheel-less Snake Robot with Active Stiffness Control for Adaptive Pedal Wave Locomotion. *Journal of Bionic Engineering*, 16(4), 593-607.

- The materials in Chapter 3, are mainly presented from this publication. Chapter 6 also presents the obtained experimentation results given in this paper.

Publication 3: Koopaee, M. J., Classens, K., Pretty, C., & Chen, X. (2019). Dynamical Modelling and Control of Snake-like Motion in Vertical Plane for Locomotion in Unstructured Environments. *The ASME 2019 International Design Engineering Technical Conferences & Computers and Information in Engineering Conference (IDETC/CIE 2019)*, Anaheim, California, USA, (Accepted).

- Parts of Chapter 4, particularly sections 4.3, 4.4 and 4.5 are presented from this publication.

Publication 4: Koopaee, M. J., Van Huijgevoort, B., Pretty, C., & Chen, X. (2018). Parameters tuning of snake robots sidewinding gait using Bayesian optimization. *The IEEE* 2018 *International Conference on Control, Automation and Robotics (ICCAR 2019)*, Auckland, New Zealand, pp. 43-49.

- Parts of Chapter 3, particularly sections 3.1, and 3.2, are presented from this publication.

Publication 5: Koopaee, M. J., Gilani, C., Scott, C., & Chen, X. (2018). Bio-Inspired Snake Robots: Design, Modelling, and Control. *In Handbook of Research on Biomimetics and Biomedical Robotics* (pp. 246-275). IGI Global.

- Chapter 2, particularly sections 2.2, 2.4, and 2.5, present part of the materials firstly appeared in this publication.

Please detail the nature and extent (%) of contribution by the candidate:

Publication 1: Methodology developed by the candidate. The code developed by the candidate with contributions from Classens. Experimentation and simulation results, and written content produced by the candidate. All the authors provided comments and review. 90% of the research, and 95% of the writing was contributed by the candidate.

Publication 2: Methodology developed by the candidate. The initial design of the sensor developed through discussions between the candidate and Pretty. Bal provided assistance in the design and testing of the manufactured sensor. The codes, experimentation and simulation results and written content produced by the candidate. Pretty and Chen provided comments and review. 85% of the research, and 95% of the writing was contributed by the candidate.

Publication 3: Methodology developed by the candidate. The code developed by the candidate with contributions from Classens. The results, and written content produced by the candidate. All the authors provided comments and review. 85% of the research, and 95% of the writing was contributed by the candidate.

Publication 4: Methodology developed by the candidate. Parts of the optimization code developed by Van Huijgevoort. Pretty and Chen provided comments and review. 95% of the research, and 95% of the writing was contributed by the candidate.

Publication 5: Methodology developed by the candidate. Gilani and Scott provided parts of the written content. All the authors provided comments and review. 95% of the research, and 85% of the writing was contributed by the candidate.

Certification by Co-authors:

If there is more than one co-author then a single co-author can sign on behalf of all

The undersigned certifies that:

- The above statement correctly reflects the nature and extent of the PhD candidate's contribution to this co-authored work
- In cases where the candidate was the lead author of the co-authored work he or she wrote the text

Name: *Christopher Pretty* Signature: **Christopher Pretty** Date: *29/08/2019*

Name: *XiaoQi Chen* Signature: *XiaoQi Chen* Date: *23/08/2019*

Acknowledgement

I would like to express my sincere appreciation to Dr Chris Pretty and Dr XiaoQi Chen from the Mechanical Engineering Department at the University of Canterbury (UC) and the Department of Mechanical and Product Design Engineering of university of Swinburne for providing me with their extensive knowledge and their endless support throughout my entire PhD study. I would like to thank XiaoQi for giving me the chance to become part of the UC family and to gain invaluable experience. I also would like to acknowledge Chris, for his invaluable support and knowledge. He is a good friend and a great teacher. I am always grateful for his support.

My gratitude to the technical staff of the UC Mechanical Engineering workshop, Gerry Kirk, Julian Murphy, Julian Philips and David Reed, who contributed the essential technical work and guidance throughout this study. Especially, I would like to acknowledge Gerry, one of the kindest person I have ever met, for sharing his extraordinary technical knowledge with me.

I also would like to thank my family and friends, who were beside me during this journey. I hope to get a chance to properly show my appreciation to them.

The work presented in this thesis was financially supported through the University of Canterbury doctoral scholarship provided by the Department of Mechanical Engineering. I would like to thank them for their support, which made this research work possible.

Contents

List of Figures

List of Tables

Nomenclature

ABS	Acrylonitrile Butadiene Styrene
ACM	Active Cord Mechanism
CAD	Computer Aided Design
CAN	Controller Area Network
CPG	Central pattern generator
DOF	Degrees of Freedom
FEA	Finite Element Analysis
FSR	Force Sensitive Resistor
IMU	Inertial Measurement Unit
PCB	Printed Circuit Board
PID	Proportional integral derivative controller
SEA	Series Elastic Actuator
TSC	Tail-Leading Stiffness Control

1 INTRODUCTION

1.1 Motivation

Mobile robotic systems are dominated by wheels as the main means of locomotion. Such mobile robots are usually the first design concept for any mobile platform because they are easy to model, control and manufacture [1]. However, such mechanisms are often effective for locomotion on relatively smooth surfaces and can become useless, when it comes to locomotion in unstructured environments, where adaptability is necessary [2].

On the other hand, there are many organisms with locomotion mechanisms that are incredibly effective in unstructured environments evolved over millions of years in response to the changing environmental conditions, which are invaluable sources for engineering inspiration [3]. One of these effective locomotion mechanisms is the snake locomotion [4]. The widespread existence of these creatures in almost every environment ranging from rivers to deserts and forests, clearly shows the effectiveness of their unique locomotion pattern. This suggests that snake-like locomotion mechanisms can be ideal alternative strategies for locomotion in unstructured environments.

In addition to effective locomotion in many environments, a snake-like robotic mechanism with similar characteristics to biological snakes provides a number of advantages over conventional robotic systems. These advantages including small body cross-section, intrinsic stability, hyper redundancy and high adaptability suggest that bio-inspired snake-like robots present a rich avenue of research for developing a robotic system capable of operation across a wide variety of environments.

1.1.1 Small body cross section

One of the desirable characteristics of snake-like mechanisms, similar to their natural counterparts is their small body cross section, which makes them suitable for locomotion in narrow and confined spaces, such as pipes, narrow canals and ducts [5]. This is shown in Figure 1.1 using the V-Rep simulation environment [6]. As it can be seen in Figure 1.1, the small cross section of the snake robot relative to its length, allows the robot to manoeuvre between two parallel planes, which is not possible to explore with

conventional wheeled robots, unless reducing the size of the robot, which limits its maximum speed and capabilities.

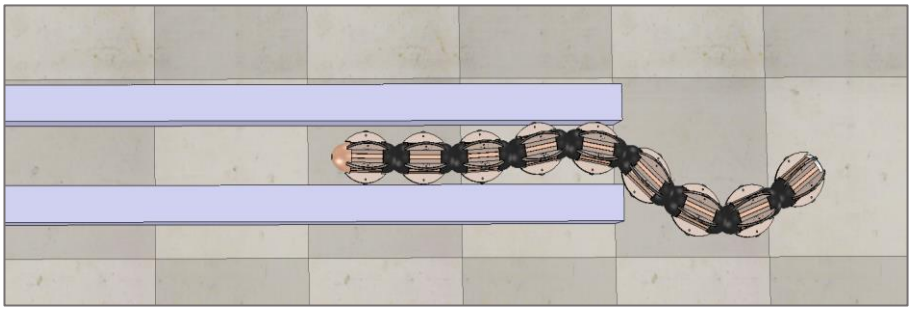

Figure 1.1. A snake robot moving forward in a confined space by pushing against the walls, simulated in V-Rep environments.

1.1.2 Intrinsic locomotion stability

In legged robots, the stability even on smooth surfaces is a major concern. However, in snake locomotion, instability of the robot is not usually an issue [7]. The reason is that unlike walking, in snake locomotion the centre of mass of the robot remains very close to the ground. This means that the projection of the centre of the gravity will be located inside the convex hull of contact points during the locomotion. Thus, compared to legged locomotion [8], the static stability of the robot during the locomotion, even on rough terrains can be guaranteed with less effort.

1.1.3 Modularity and Hyper-redundancy

Another advantage of snake robots is their modular design and hyper-redundancy. There are many cases that the robot needs to operate in remote and inaccessible environments, which makes the maintenance of a damaged robot very costly. However, the body of a modular snake robot consists of several identical modules, making it relatively inexpensive to manufacture and repair.

In addition, snake robots belong to the hyper-redundant robotic mechanism family. This means that modular snake robots can have more degrees of freedom (DoF) than the minimum required number makes them very suitable for locomotion in complex and unstructured environments, where extra DoF can be used to achieve more agile motion [9]. Moreover, the hyper redundancy of the snake robots makes them more robust in response to an actuator fault in any of the modules, when the rest of the modules can be controlled to minimize the effect of the fault on the overall robot motion [10].

1.1.4 Adaptability

Biological snakes, have demonstrated incredible abilities to move in unstructured environments, which stems from the hyper-redundancy of their body structure, effective environmental sensing and efficient locomotion patterns. Although the existing modular snake robots are not as sophisticated as biological snakes, many existing snake robot designs have also shown an impressive capability for locomotion in confined spaces [11], cluttered environments [12] and on rough terrains [13].

1.2 Aims and Scope

Snake-like robots, have the potential to be used in unstructured environments. However, because of design limitations, modelling complexity and lack of a generalized control scheme, existing snake robot mechanisms have very limited capabilities in such environments. Specifically, on surfaces with irregularities, which is a very common scenario in real world environments the sake robot capabilities should be improved.

Firstly, modular snake robots have several Degrees of Freedom (DoF) [14], numerous possible points of contact with the environment [15] and suffer from lack of a

fixed base on the chassis [16]. Hence, choosing a suitable sensory mechanism essential for achieving effective locomotion on surfaces with irregularities is very challenging [17]. Moreover, because of the limited available space inside of each robot module, acquiring a sensory system off the shelf to be used in the robot is not possible. Hence, to control the snake robot employing the environmental feedback signals, designing a snake robot with a custom-built sensory mechanism is inevitable.

Additionally, modelling a hyper-redundant snake robot with numerous contact points with the environment is a critical step towards enabling effective snake locomotion. Such simulation model can facilitate the mechanical design of the robot and allows designers to examine the effectiveness of the sensory mechanism and testing of the proposed controllers. Some works such as [18] and [19] have proposed a modelling framework for the snake-like locomotion modelling. However, dynamical modelling of the snake locomotion capable of simulating the locomotion on surfaces with irregularities is yet to be fully addressed in more details.

Moreover, incorporating the sensory information into the snake robot controller for achieving effective motion is another important issue that needs to be solved. For simple mechanical systems, such as an inverted pendulum [20] or a wheeled robot [1], traditional model-based control approaches have been used successfully. However, adaptive real-time control of snake robots on surfaces with irregularities requires novel methods to deal with the under-actuation, high nonlinearity and uncertainty of the snake robots models [21].

This thesis aims to address these issues regarding snake-like locomotion in environments with irregularities using sensory feedback. Particularly, this work addresses the following challenges:

- Design, manufacture and validation of a custom-built sensory mechanism for the snake robot to collect environmental information for effective locomotion on surfaces with irregularities.
- Dynamical modelling of the snake-like robot capable of efficient simulation of the snake locomotion on surfaces with irregularities by taking into account the external contact forces.
- Developing effective methods to incorporate the sensory feedback into the snake robot controller for achieving effective locomotion patterns on surfaces with irregularities.

1.3 Thesis Contribution

The novel contributions of this thesis can be summarized as follows:

1.3.1 Design of a cost-effective modular snake robot with Series Elastic Actuators (SEAs) for reliable torque measurement for pedal wave locomotion on surfaces with irregularities

As the basic component of this thesis, the design of a cost-effective modular snake robot is presented. To design the motor torque measurement unit as a reliable and robust environmental sensing mechanism, an elastic element with the desired shape and stiffness has been designed and manufactured using easily accessible Polyurethane sheets and attached between the links and the motors to turn a conventional servo into a SEA. This torque measurement mechanism, unlike others, which requires redesigning every module of the robot, such as [22] can easily be implemented on existing designs. Moreover, unlike

existing methods, such as [17] and [23] in which the sensing device should be attached to the surface of the links, the Polyurethane-based compliant element is embedded inside each joint, thus the final prototype is more robust in design.

In addition to the design of SEA, the snake robot modules are also designed and manufactured using a cost effective 3D printer with Acrylonitrile Butadiene Styrene (ABS), which made the prototype cost-effective. Unlike other works, such as [24] the designed snake robot modules are not equipped with wheels, which makes the robot more suitable for pedal wave locomotion in challenging environments. Using this design the robot can perform pedal wave locomotion by lifting its body sections in the vertical plane and climbing over obstacles, where wheeled snake robots might suffer from the same limitations of wheeled robots.

1.3.2 Dynamical modelling of 2D snake robots with SEAs for simulating the pedal wave locomotion on surfaces with irregularities

This thesis also introduces the equations of motion of modular 2D snake robots with SEAs in the vertical plane for the first time. In particular, the kinematics of pedal wave motion (undulation in vertical plane) of the modular snake robots is presented in matrix form, which makes the simulation more computationally efficient and enables to use the same modelling framework to simulate any 2D snake motion.

Generally speaking, utilizing a high stiffness flexible element in the design of the robot actuator, it is possible to neglect the effect of the spring and model the robot with stiff joints [25]. However, the use of very stiff elements for SEA, requires high resolution encoders for measurement of the small deflections of the flexible element, increasing the final cost of the prototype. Hence, using the Euler-Lagrange method, the equations of motion of the snake robot with SEAs are constructed, which is the first snake robot model,

which takes into account the joint flexibility. Moreover, using the well-known spring-damper (Kelvin-Voigt) contact model, external contact forces are taken into account and pedal wave locomotion on smooth and uneven surfaces is modelled and simulated, which allows investigation of the effect of joint flexibility, ground friction and other environmental conditions on the snake pedal wave locomotion.

1.3.3 Development of control strategies based on active stiffness control and position feedback for achieving pedal wave locomotion on surfaces with irregularities

As a major part of this thesis, a distributed control system is designed, which completed with the help of an admittance controller, enables active control of the joint stiffness to achieve effective snake robot pedal wave locomotion. Thus, the controller enables the robot to adaptively climb over obstacles, which unlike existing methods, such as [13] does not require prior information about the location of the obstacle. The effectiveness of the proposed controller in comparison to an open-loop control strategy has been shown by several experiments, which showed the capability of the robot to successfully climb over obstacles with the height of more than 55% of the diameter of the snake robot modules, which was not possible with open-loop gait based controllers due to the instability of the robot motion. Moreover, to improve the effectiveness of the snake robot pedal wave motion, an extended stiffness control strategy is also proposed, where the position feedback signal propagates along the snake body, allowing the robot to climb over multiple obstacles without rolling over to one side.

1.4 Thesis Outline

This thesis is organized into eight chapters. The next chapters will be presented as follows:

Chapter 2. *Literature Review* introduces the overview of the recent research carried out in snake-like locomotion. In particular, this chapter is focused on reviewing the available literature on such robotic system form design, modelling and control perspective with emphasis on locomotion in unstructured environments.

Chapter 3. *Design and Development of a Modular Snake Robot with SEAs for Locomotion on Surfaces with Irregularities* introduces the design and manufacture process of a cost effective snake robot with SEAs capable of locomotion on surfaces with irregularities. The design and manufacture process of a Polyurethane based elastic element will be presented, the snake robot modules design will be given and the details of the electronics control system architecture will be presented.

Chapter 4. *Dynamical Modelling of the Pedal wave Locomotion of Modular Snake Robots with SEA* presents the first of its kind dynamical model for modular snake robots with joint flexibility. The kinematics relations are obtained in matrix form and Euler-Lagrange equations are used to construct the equations of motion. Moreover, the spring damper contact model is employed allowing to simulate the pedal wave motion of the snake robot on surfaces with irregularities.

Chapter 5. *Pedal Wave Locomotion on Smooth Surfaces: Experimental and Simulation Results* presents the experimental and simulation results obtained by experimentation on the physical and the simulated snake robot on smooth surfaces. The effectiveness of the snake robot design is examined, the validity of the simulation model is investigated and the contributing factors in such motion is discussed.

Chapter 6. *Local Stiffness Control Strategy for Pedal Wave Locomotion on Surfaces with Irregularities* is discussed. The idea of compliant pedal wave locomotion is given and

the effectiveness of the controller is investigated through several experimentation with the physical robot.

Chapter 7. *Tail-Leading Stiffness Control Strategy for Pedal Wave Locomotion on Surfaces with Irregularities,* extends the idea of stiffness control strategy and introduces a controller for pedal wave locomotion using the measured torque signal and position feedback propagated along the snake body. Experimentation and simulation results are included and an extensive discussion on the results is provided.

Chapter 8. *Conclusion and Future research direction* presents an overview of the presented work and the key results. Moreover, in this chapter the future research directions are discussed and the some recommendations are given.

2
LITERATURE REVIEW

2.1 Introduction

Mother Nature has always been a source of inspiration for human beings. There are many life forms each using an incredible and unique locomotion mechanism adapted to the challenging environmental conditions over millions of years. These locomotion patterns, such as slithering of snakes [26], human walking [27], grasshopper jumping [28] or Leech swimming [29] are very effective in real world environments makes them ideal as the main means of locomotion for robotic systems for real world applications.

Among various bio-inspired motions, the locomotion of snakes has always been an interesting phenomenon for scientific study. The elegant locomotion of snakes on smooth and uneven surfaces [8], under the water [30] and through narrow channels [31] shows the success and efficacy of their locomotion pattern. Moreover, snake's locomotion is a relatively efficient type of locomotion, which consumes less energy compared to other biological forms with similar sizes, weights, and speeds [32]. Considering these desirable characteristics, snake-like robots effectively mimicking biological snakes locomotion patterns, have the potential to overcome the challenges of the locomotion in the real world environments to meet the emerging needs for effective exploration and operation in such environments.

In this chapter, the most important aspects of snake locomotion, with special focus on snake-like locomotion in unstructured environments will be discussed. The major studies conducted on biological snakes will be introduced and the basic characteristics of such motion will be presented. Finally, the major advancements in the field of snake robots design, modelling and control with focus on adaptive locomotion will be introduced.

2.2 Biological Snake Locomotion

The first published discussion about snake movement goes back to ancient times, when Aristotle studied the snake locomotion as a part of a book about animal locomotion capabilities [14]. However, since those early studies, scientists' knowledge on different aspects of biological snake, such as their body structures, locomotion mechanism and sensory system have increased considerably.

For centuries, the general belief even among zoologists was that snakes use their scales or tips of their ribs in a similar manner that other animals use their legs as means of locomotion [14]. In 1879, Hutchinson challenged this theory by observing a snake ascending to the top of a glass jar and argued that there should be some other justifications for the snake-like movement [33]. To explain this peculiar behavior, obviously contradicting the existing theory, Fokker [34] came up with an alternative explanation, which can be considered as the first accurate description of the snake movement mechanism. In this work, originally published in Dutch, the snake is modelled as a thin elastic body confined in a groove curved into a board, and it is argued that snakes move in such a way that the total potential energy of their body decreases. Mosauer, in [35], without mentioning Fokker's results, categorized snake locomotion into three different groups, however did not discuss mechanical modelling or the mathematical foundation of each type of movement. Later on, Jones motivated by the simplified model of Fokker, modelled the snake body as serially connected spools and showed that Mosauer results can indeed be supported theoretically [36].

In the 1940s, motivated by Fokker and Mosauer's work, Gray conducted a comprehensive study on the snake locomotion by observing a common grass snake (Tropidonotus natrix) [37]. He searched for the answer to the basic question that "How can axial muscular activity generate propulsive force?" To address this question, he considered the snake as a serially connected rigid rods hinged together, where axial muscles are regarded as elastic elements operating laterally to the hinges. Using this model, he empirically explained the mechanism of each type of the snake locomotion. One of the most important consequence of Gray's experiments was that each part of the body of the snake should be in contact with the external obstacles preventing from moving in the direction

normal to that segment of the snake body to enable the snake move forward. Finally, Gans in [38] further discussed limbless locomotion patterns and described the dynamics of four major locomotion patterns qualitatively, which complemented by the Gray's studies gave a comprehensive description of the snake movement.

2.2.1 Biological snake locomotion patterns

As a result of the leading studies of Gray [37] and Gans [38], it was found that skeleton structure of the snake plays a major role in snake locomotion. As shown in Figure 2.1, the skeleton consists of flexible vertebrae connected to each other with a ball and socket mechanism to form the backbone of the snake [39]. Each vertebra is also connected to two ribs on its sides, similar to fish, which also use a very similar locomotion pattern for swimming. Vertebrae and ribs are connected together with the help of three types of muscle (semispinalis-spinalis, longissimus dorsi and iliocostalis) [40], which their contraction and relaxation play the critical role in the snake motion generation. The relative movement of the vertebrae caused by the muscular contraction is limited. However, the number of vertebrae is large enough, to result in large overall motion.

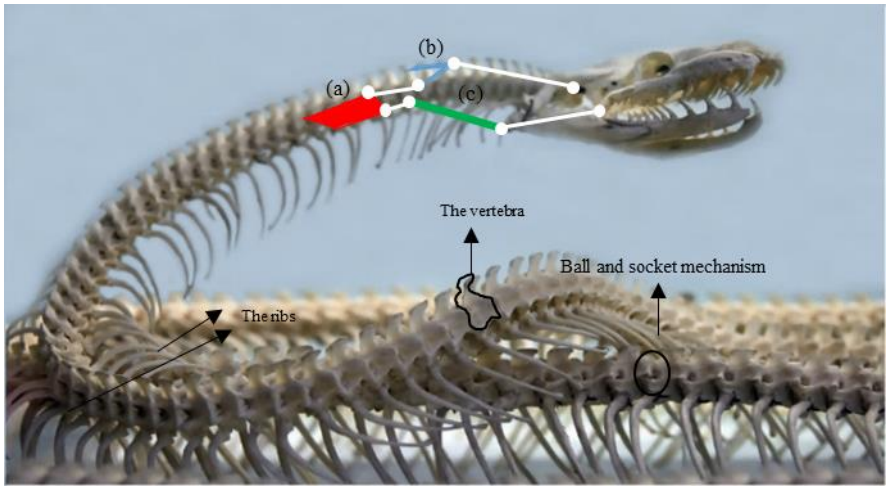

Figure 2.1. The skeleton structure of a snake, showing the vertebra and the ribs, where (a), (b) and (c) show the approximate position and shape of longissimus dorsi, iliocostalis and semispinalis, respectively and tendons shown in white (see [40] for more details).

Although different species of snakes have a very similar body structure, they use different locomotion patterns, depending on their size, habitat and instincts. Among these locomotion patterns some are more common than others. Not all snakes can perform every possible locomotion pattern. However, four locomotion patterns, namely lateral undulation, concertina, sidewinding, and rectilinear motion are the most common motion patterns.

Generally speaking, there are two methods to mathematically describe these locomotion patterns: considering a highly articulated body consisting of discrete, rigid elements connected by joints or a continuous curve capturing the macroscopic shape of the snake body. In early works, such as [36] and [37] the segmented mechanical model of snakes is considered to explain the fundamentals of their locomotion patterns. Others, such as [41], considered the snake as an elastic rod confined in a hard wall without friction and explained the movement of the snake based on the elastic energy of the snake body. This model has recently been extended in [42] to encompass the case when just part of the snake body is in contact with the wall. Other similar methods, such as [43] have also been proposed recently, which instead of considering a wall around the snake body, the snake is modelled as a planar curve.

Although both segmented and curve-based models have been adopted in the literature to describe snake movement, the hyper redundancy of the biological snake skeleton makes the curve-based approach more advantageous for qualitative description of the snake locomotion. Hence, to describe the motion of the snake in the next section, the body of the snake is considered as a continuous curve and the basics of the snake locomotion is explained based on the macroscopic shape of the snake body, similar to the curve-based approach in [43].

2.2.1.1 Lateral undulation (serpentine locomotion)

Lateral undulation or serpentine locomotion is the most common type of locomotion among snakes, which has been studied extensively. In the early studies, such as [37], the serpentine mode of locomotion is studied considering the existence of a number of pegs, against which the snake can push and move forward. The snake produces a periodic wave traveling backwards from its head to its tail and pushes against the pegs (irregularities of the terrain) to generate a propulsive forward force enabling the snake to move. Figure 2.2 shows this type of locomotion.

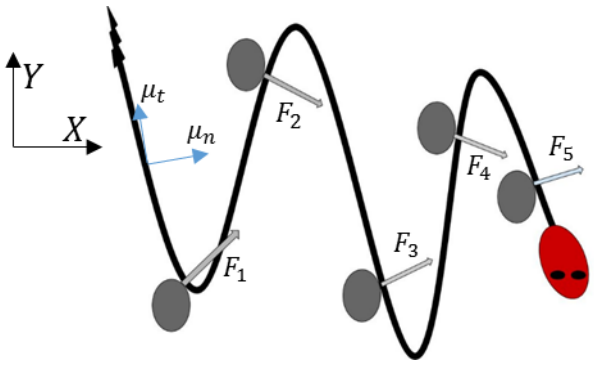

Figure 2.2. Summary of Lateral undulation, showing the external forces and the obstacles the snake pushes against to move forward in XY plane and the tangential and normal friction coefficients.

Recently, it has been found that the most important requirement of lateral undulation in biological snakes is the existence of anisotropic ground friction force, which enables the snake to move forward even on relatively smooth surfaces [43]. In [43], as a result of an experimentation with a real snake (Pueblan milk, *Lampropeltis triangulum campbelli*) on an inclined plane, the existence of anisotropic friction property is proved and it is shown that the incredible ability of the snakes to generate propulsive forward forces from a lateral motion is because of the special structure of the ventral scales of the snake leading to the anisotropic friction property between snake belly and the surface beneath the snake. This

means that the snake belly scales has directional friction property. Hence, friction coefficient in the direction tangential to body (μ_t) is smaller than the friction coefficient in the normal direction (μ_n). This is very similar to a wheel, which can rotate easily, but it is difficult be moved sideways. Another important result of [43] is that the weight distribution of the snake body is not uniform in this type of locomotion. Hence this type of locomotion is in fact a 3D motion performed in both dorsal and lateral plane [43].

2.2.1.2 Concertina locomotion

Concertina locomotion, which is demonstrated in Figure 2.3 is among the first type of snake locomotion that has been studied because of its simple mechanism, compared to other types of locomotion. In this type of locomotion, usually observed among snakes travelling through narrow channels, some parts of the body are in static contact with the wall of the channel, acting as an anchor, to push against the wall in order to translate the rest of the body forward [44].

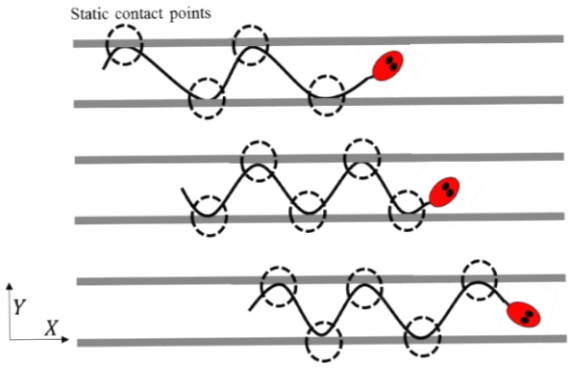

Figure 2.3. Summary of Concertina locomotion, showing the snake between two parallel walls, parts of the body in contact with the walls are shown inside the circles.

2.2.1.3 Sidewinding locomotion

Sidewinding locomotion, first studied in [33], is another type of snake locomotion, which can usually be observed among the snakes moving on soft and slippery surfaces, such as

sandy deserts. In this type of locomotion, the snake uses two separate parts of the body as static contact points to lift and bend the remaining parts [45]. As shown in Figure 2.4, the best way to imagine sidewinding in snakes is to consider the sidewise rolling of a spring coil [45], which leaves a series of disconnected tracks like the tracks left by a snake on a sandy surface.

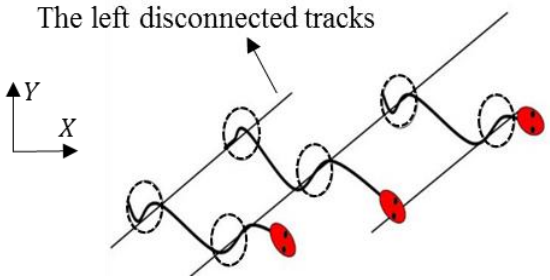

Figure 2.4. Summary of sidewinding locomotion, where the parts of the body in contact with the ground are shown inside the circles.

2.2.1.4 Rectilinear (pedal wave) locomotion

This type of locomotion, which is also named caterpillar locomotion in [35] is mostly exhibited in heavy snakes. Former studies on this type of locomotion suggested that, in rectilinear locomotion snake ribs act as legs, similar to walking, however snake does not "travel on its ribs", [46] or in the other word the snake ribs are not the main means of locomotion. Figure 2.5 shows the rectilinear motion.

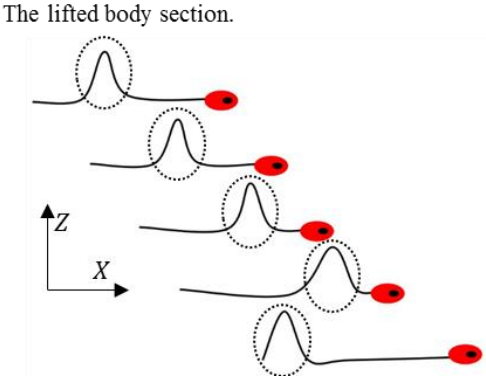

Figure 2.5. Summary of Rectilinear (pedal wave) locomotion, showing the lifted body sections in ZX plane.

In rectilinear motion, similar to earthworms the snake travels on a straight line and unlike the other type of locomotion, sideways interaction with the environment is not essential [47]. Instead, the contraction and relaxation wave pass over the ventral muscles along with the lifting body parts is the main means of locomotion [48]. Figure 2.5 displays the side view of the body shape of the snake performing rectilinear locomotion.

2.2.2 Contributing factors in biological snake locomotion

In addition to the research on mechanical modelling of snakes, there are other important aspects of snake locomotion, which have received considerable attention. Closely related to their interesting locomotion capability is the tribological behavior of the snake skin. In [49], it is shown that the friction properties of the snake skin in tangential and normal direction are not similar, which is also mathematically justified in [43]. It is mentioned in [44] that snakes can actively control the friction between its ventral scales and the ground. In [50], it is argued that the microstructure of snake skin is not the only contributing factor in anisotropic friction and indeed the underlying structure of snake skin is also a critical factor and in [51] a snake-like surface is developed by modifying the surface of metallic pins made of Titanium alloy.

Other researches have been conducted to find out the true mechanism of gait selection in snakes. Although, it is still not clear that how and when they change their locomotion pattern [52], it is argued that studies on the energetic cost of snake locomotion can help to solve this mystery [53]. In [53], by measuring the oxygen consumption of a real snake during the locomotion, it is concluded that energetic cost of lateral undulation in limbless species is equal to that of running in limbed animals, with the same weight. Hence, there might be other explanations for evolution of limbless species than efficiency of

motion. In [54], the energy cost of different locomotion patterns is compared and it is argued that the energy efficiency of different motion patterns are different even among same species, which can explain why the snake chooses different gait pattern in different environments.

2.2.3 Biological snake locomotion in unstructured environments

In addition to the studies on the snake locomotion in structured environments, some researchers have targeted snake locomotion in unstructured environments, where adaptation is necessary. However, compared to the existing literature on the snake locomotion in structured environment, the number of works in this field is limited.

In [55], it is demonstrated that in lateral undulation, the space between the pegs directly affects the speed of the snake, which showed the critical role that environmental features plays in this kind of motion. In [56], focusing on sidewinding and lateral undulation locomotion, the kinematics of the snake locomotion on variety of substrates are further analysed using cinematographic films and the relationship between the maximum speed, the substrate and locomotion mode is discussed. In [57], the muscle activity of the snake during lateral undulation is studied and it is suggested that the bending of the snake body around the pegs generate the translation force, which can modelled as a type of a cam-follower. In 2012, Marvi recognized that the aforementioned experiments have been done in an artificial environment and conducted series of studies in [44] by observing the snake's behaviour in a simulated real world conditions, such as studies on concertina locomotion, when the snake moves in a channel with a varying inclination and width. Sidewinding of snakes is also further studied in sandy slopes in [58], which revealed the behaviour of snake in varying slippery environmental conditions.

More recently in [8], recognizing that the aforementioned works on real snakes in unstructured environments, still cannot explain the adaptation mechanism of snake locomotion, series of experiments have been conducted on biological snakes traversing over 3D objects. As a result of these experiments, it is found that in such environments the snake actually partitions its body based on the external forces sensed by its skin. Hence, each section of the body is performing a different kind of motion, which cannot be described by a single motion pattern.

2.3 Snake-inspired Robots Design

Although the studies on biological snakes continued, the critical findings of Gray and his predecessors enabled Hirose to further analyze biological snakes movement and fabricate the world's first snake robot, mimicking the movements of biological snakes [14] (see Figure 2.6). Hirose modelled the snake body assuming that the whole body is comprised of serially connected joints with infinitesimal length and then approximated the acting forces in tangential and normal direction to the ground, resulted from snake muscle activity. Based on these equations and considering continuity of muscle activity, he proposed the "Serpenoid Curve" for describing the body shape of the snake performing lateral undulation and used the same concept to control a wheeled snake robot to perform lateral undulation.

Development of Active Cord Mechanism (ACM) by Hirose was the beginning of a new era in snake-inspired locomotion studies, which inspired engineers to study snake locomotion with a close collaboration with biologists, and develop more capable snake-like robots. In the rest of this thesis, the main focus will be on the results closely related to modular snake-inspired locomotors, similar to biological snakes. Hence, the related works,

such as [59] and [60], which contain results on soft robots and snake inspired soft manipulators, respectively will not be discussed.

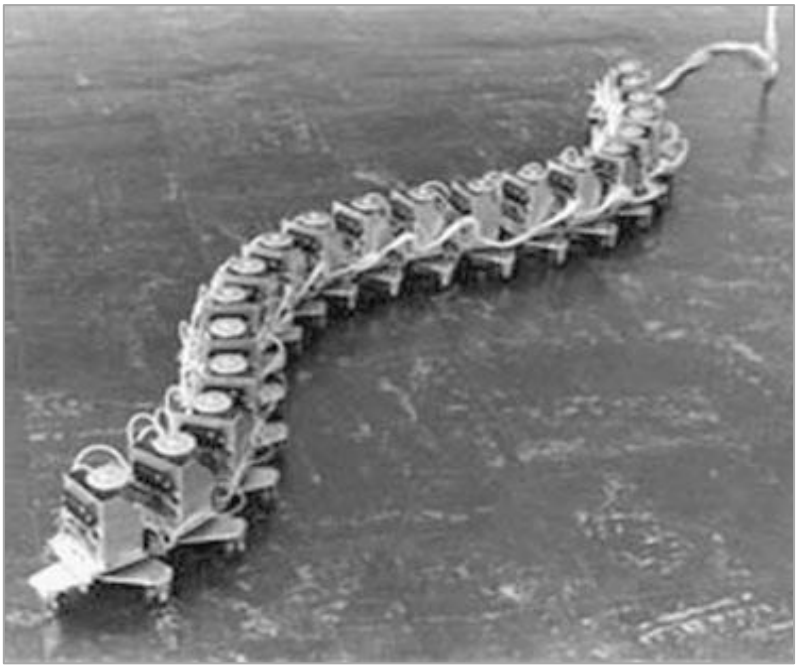

Figure 2.6. Active Cord Mechanism (ACM), equipped with passive wheels [14], performing lateral undulation on a smooth surface.

2.3.1 Mechanical design of the modules

To mimic snake locomotion, Hirose in [14], considered sideslip constraints, which is implemented by installing passive wheels on the sideways of the robot. Although this design is not in harmony with the body structure and anisotropic friction property of biological snakes, many recent studies, such as [41-43] have considered snake robots with sideslip constraint to generate similar anisotropic friction force exist in biological snakes (See Figure 2.7). These robots can perform lateral undulation similar to biological snakes. However, they are still equipped with wheels, thus suffer from the basic limitations of wheeled robots [44].

Figure 2.7. A snake robot with passive wheels climbing over a stair, knowing the position and height of the stair [64].

Other works, such as [65] and [66] have used active wheels or tread with each link having its own means of propulsion. Although these robots, shown in Figure 2.8 and Figure 2.9 have shown impressive capabilities to operate in real world environments, their locomotion mechanism is fundamentally different from biological snakes, hence they can hardly be categorizes as snake-like robots.

Snake-like mechanisms without sideways wheels, such as [67] or the one in [68], shown in Figure 2.10 are not equipped with active means of propulsion other than the motors at each joint. Although these wheel-less snake robots, cannot perform lateral undulation due to the lack of anisotropic friction property, they have a similar structure to biological snakes and can perform rectilinear (pedal wave) [69] or its 3D generalization sidewinding [70] locomotion, which are highly adaptive and effective locomotion patterns. Moreover, it has been shown that these robotic mechanisms can also perform gait patterns, such as rolling and corkscrewing [50,51] not seen to be performed by biological snakes. Such abilities could be very beneficial in real word environments, where it has been shown that not a single structured gait pattern can be used to mimic snake motion [8].

Figure 2.8. ACM-R4 with active wheels [65].

Figure 2.9. Omni Tread snake-like robot with active tread climbing over a stair [66].

Figure 2.10. Uncle Sam [68], a wheel-less snake-like robot.

2.3.2 Sensory system

Sensing is the key to adaptation in any robotic mechanism because a smart controller needs to gather information from the environment and employ it to adaptively control the behavior of the system. However, designing such sensing mechanism in snake robots is a challenging task. Unlike humanoid robots, where head cameras and Light Detection and Ranging devices (LiDAR) [72] have been used extensively to perceive the environments, in snake robots placing an on-board camera is challenging due to constant movements of all the robot modules [16]. Hence, most of the existing snake robots designed for locomotion in unstructured environments are equipped with some kind of torque, force or pressure sensors to gather information about the environment by sensing the interactions with the surroundings.

To achieve this goal, some works such as [73] have installed sideways contact switches to detect sideways contact with the environments. Others, such as [74] have used pressure sensors attached beneath the robot modules. More recent works have considered a design with Force Sensor Resistors (FSRs) [67], strain gauges [23], and a complex, custom made torque sensing system based on a cam mechanism [22] to equip the snake robots with sensitive torque/force mechanisms. A Snake robot equipped with Series Elastic Actuators (SEA), capable of torque measurement is presented in [68] and [75]. Although the manufacture process requires compression mouldings and a relatively complicated process for bonding the rubber to a metallic material, the overall performance of the sensing system seems to be satisfactory [76].

Overall, despite the recent progress, development of a wheel-less snake robot equipped with a torque/force sensing mechanism for investigation of adaptive control strategies remains to be challenging. The main reason is that in modular snake robots, the

available space in each joint is limited. Thus, commercially available torque sensors cannot be used. Moreover, a force sensing mechanism attached to the surface of the links is vulnerable to contact with the environment. Hence, development of a cost-effective modular snake robot with a specially designed torque sensor allowing to investigate adaptive control strategies based on force/torque feedback is one of the main parts of this thesis.

2.4 Dynamical Modelling of Modular Snake Robots

Similar to biological snakes, there exists two general methods to model wheel-less modular snake-like mechanisms, namely the Continuum model to capture only the macroscopic shape of the snake [77] or the well-known segmented model used in many works, such as [78]. Although both of these models can capture essentials of the snake locomotion, they have some advantages and disadvantages depending on the application and the structure of the robotic mechanism, which will be discussed in more details.

2.4.1 Continuum models

A major contributing factor in snake locomotion is the macroscopic shape of the snake body and the changes in response to the environmental forces. For this reason, a flexible shape based modeling method like "Backbone Curve" approach proposed in [9] has been shown to be a beneficial tool for modelling snake-like mechanisms.

Consider a curve as a differentiable map $\alpha: I \rightarrow \mathbb{R}^3$ of an open interval $I = (a, b)$ of the real line $\mathbb{R}$ into $\mathbb{R}^3$ as follows [79]:

$$\alpha(s) = (x(s), y(s), z(s)), \tag{2.1}$$

where the functions $x(s), y(s), z(s)$ are differentiable functions and s is the curve parameter, usually chosen to be the arc length of the curve. By definition, the arc length of the curve from an initial point $s_0$to arbitrary point s can be calculated as:

$$L(s) = \int_{s_0}^{s} |\alpha'(\sigma)|\, d\sigma, \tag{2.2}$$

where $|\alpha'(s)| = \sqrt{\left(\frac{dx}{ds}\right)^2 + \left(\frac{dy}{ds}\right)^2 + \left(\frac{dz}{ds}\right)^2}$. Choosing the the curve parameter s to be the arc length:

$$L(s) = s - s_0, \tag{2.3}$$

which results that:

$$|\alpha'(s)| = 1. \tag{2.4}$$

This is an important results because it shows that, if we choose the curve parameter to be the curve arc length, the magnitude of $\alpha'(s)$ is always equal to one. This allows to define Curvature and Torsion functions and assign the well-known Frenet-Serret frames to each point on the curve [77]. Using this parameterization method, the position of each point on a snake body relative to the origin of a frame attached to the tail of the snake specified in Cartesian coordinate can be obtained as follows:

$$\vec{x}(s,t) = \int_{s_0}^{s} \vec{u}(\sigma,t)\, d\sigma, \tag{2.5}$$

where t stands for time, $\vec{u}(\sigma,t) = \frac{\partial \alpha(\sigma,t)}{\partial \sigma}$ and $s \in I = (0,1)$, is the normalized length of the snake, which will not change with respect to time as the modular snakes are considered to

be inextensible. An intuitive way to understand relation (2.5) is to consider the integral over σ of $\vec{u}(\sigma, t)$, as sum of all tangent vector from base to the specific point s, hence the resultant position vector would be $\vec{x}(s, t)$ as shown in Figure 2.11.

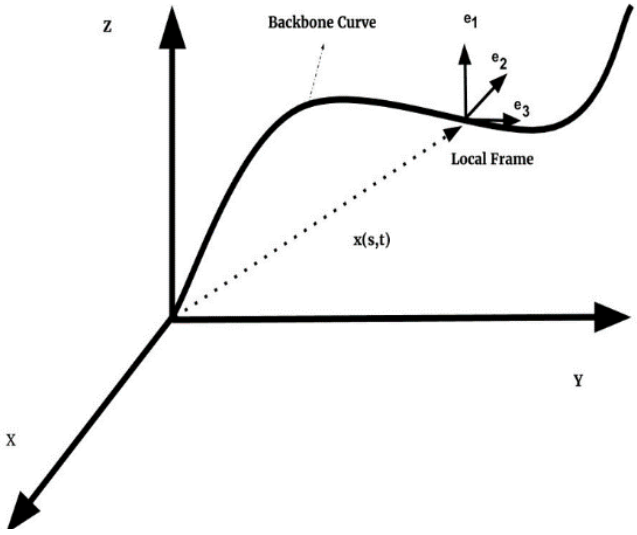

Figure 2.11. Backbone curve and its set of reference frame.

Although, this curve-based modelling framework is mainly proposed for modelling hyper-redundant and/or continuum robots, they can be adapted for modeling of modular snake robots as well. This can be done using discretization methods, such as anneal chain fitting [80], where an optimization algorithm is used to find the optimum values of joint angles, which best fit the desired body shape of the robot described by $\vec{x}(s, t)$.

Continuum modelling together with the annealed chain fitting algorithm [80], are very useful for the modelling of soft robots and hyper redundant mechanisms [9]. However, for modular snake robots with a finite number of modules, such methods becomes computationally expensive and theoretically complicated, without any major benefit [81] . Hence, for modelling modular snake robots, which is the main focus of this thesis a segmented model is more advantageous.

2.4.2 Segmented models

A segmented modelling approach can be used to precisely model the mechanical structure of a modular snake robot, the dynamics of the actuator and the environmental external forces [82]. The following figure demonstrates the segmented body shape of a snake robot with six links moving in the vertical plane:

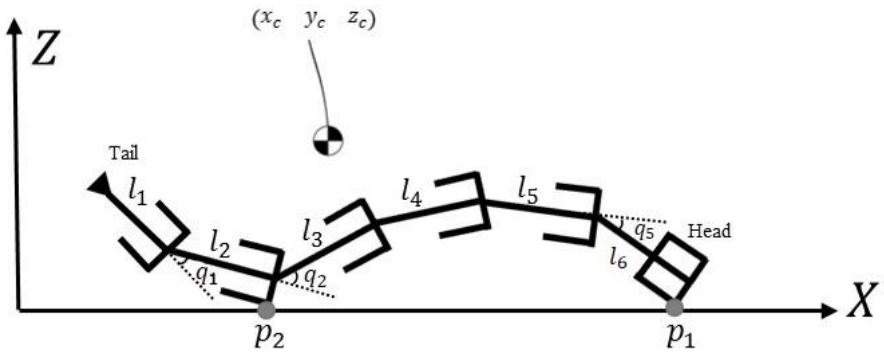

Figure 2.12. The simplified segmented model of the snake robot moving forward in the vertical plane XZ.

where $q_i;\ i = 1,2,\dots,N$ are joint angles controlled by the actuators attached between the links, P_1 and P_2 are the contact points between the robot and the ground and (x_c, y_c, z_c) denotes the centre of mass of the robot.

Considering this segmented model, in [83] based on the balance equation in vertical direction, the total external forces acting on the centre of mass of the robot is obtained without the need for using a continuum model. Using such model, it is possible to comment on the controller input. For example, it is argued in [83] that during rectilinear motion the motor torque closer to the centre of mass of the robot should generate more output torque, which is very advantageous, providing useful information facilitating the design process and the sensor selection procedure. Additionally, using such models one can investigate the effect of varying the robot design parameters, such as link lengths, mass and friction

properties, which is complicated using a continuum model. Other works, such as [84] have also considered the segmented models of the robot, because they offer a meaningful insight into the robot mechanism, enables effective modelling of the motion of the robot and can relate the actuators angular position and velocity to the kinematics of the robot.

2.5 Snake Robot Control Strategies

Unlike many processes and simple mechanical systems, in which the traditional model based control approaches have been used successfully, these approaches are not useful for real time control of snake robots. The reason is that snake robots, which are not equipped with passive wheels and do not have anisotropic friction property of belly scales of their natural counterpart belong to the under-actuated robotic systems family, for which conventional model based control methods are computationally expensive and difficult to implement. Consequently, most of the locomotion control strategies for wheel-less snake robots are based on generating biologically inspired periodic joint angle commands (gait patterns) to achieve a desired type of motion by tuning its parameters [85].

2.5.1 Control strategies in structured environments

To control the snake robot in structured environments, the majority of the works, such as [86] and more recently [87] have proposed gait patterns with different properties, such as robustness. However, most of the proposed gait patterns have a very similar structure. For example, in flat surfaces, most of the designed controllers are based on a sinusoidal gait pattern generating the joint angles as follows [17]:

$$q_i = A\,sin\big(\omega t + \phi(i-1)\big) \tag{2.6}$$

where $q_i;\ i = 1,2,\dots,N$ are joint angles, N is the number of links, ω is the temporal frequency, ϕ is the spatial frequency and A is the amplitude of the sinusoidal wave.

Instead of using nonlinear oscillators, such as (2.6) a bio-inspired oscillator, namely Central Pattern Generator (CPGs) is introduced in [88]. This system consists of a network of connected "Neurons" capable of producing rhythmic motor patterns without using any external input. Using such oscillators, the rhythmic reference for each joint will be generated by the CPG network. Hence, with the help of a series of successive rhythmic signals with certain phase difference, one can generate the joint angle references for producing the snake-like locomotion. In some of the recent papers, such as [89] smooth switching between different snake locomotion is also included and in [90] the relation between CPG parameters (similar to A, ω and ϕ) and the snake body shape is investigated, which makes this approach very suitable for snake robot control in structured environments.

2.5.2 Control strategies in environments with irregularities

Snake robots should be able to effectively move in real world, unstructured environments. However, most of the existing works have only considered locomotion in structured lab environments, which does not align with the initial motivation for designing the snake robots. Sensing the environment and adaptation is not necessary in structured environments, since the predetermined gait patterns, such as (2.6) can be used in open-loop without incorporating any external feedback from the environment [15]. However, intelligent and effective snake robot locomotion in unknown and real-world environments requires the snake robot to sense the environment and adapt its body shape and movements accordingly.

In general, there are two types of irregularities that snake robots should deal with in real word environments. The first type is lateral irregularities, where obstacles/irregularities are to the side of the snake robot. The second type is vertical irregularities, occur when the robot is moving forward on non- smooth surfaces, i.e., the robots move forward on uneven terrain. Hence, it is worthwhile to categorize the available literature into two groups as follows.

2.5.2.1 Locomotion in environments with lateral irregularities

The first type of irregularities that a snake robot should deal with is the case when there exist some obstacles to the sides of the robot, which the snake robot can either avoid or use them as push points. To deal with this situation, some works, such as [91] and [82] have proposed obstacle assisted locomotion patterns, in which the robot uses the obstacles in the environment to push against and move forward instead of trying to avoid them. More specifically, in [91] using the information from tactile sensors mounted on the side of the joints, an algorithm for achieving obstacle assisted locomotion is proposed. In this paper, based on the observation of real snakes during progressive motions, each section of the snake body is enforced to faithfully follow the path taken by the head module. As a result, when the robot's head module makes contact with a new push point, a curve fitting algorithm followed by a discretization method computes the reference angle for the rest of the joints for the future step times until a new obstacle comes in contact with the head module.

To deal with the same scenario, in [15] a jam resolution scheme is proposed, that is activated, when the robot is jammed between the obstacles, which is a very common situation in real world environments. In this situation, the links in contact with the obstacles are rotated to increase the propulsive component of the contact force. This means that the

adaptive component of the proposed hybrid controller activates, only when the robot is jammed. A combination of such adaptive schemes with a non-adaptive gait pattern and a switching law, which selects the appropriate controller at appropriate time is shown to be effective in simulation studies and experimentation in [82] and [12], respectively. However, in this approach the robot still needs to use visual feedback from a camera above the robot not available in real world environments.

Other proposed method for achieving adaptive snake locomotion in environments with lateral irregularities are shape-based control strategies, such as the ones in [11] and [92]. Under typical operation, trajectories should be generated for the snake robot's joints based on the parametrized gait functions. However, in [11] it is argued that for some reasons, such as the actuator limitations or environmental constraints, the actual joint angles rarely match with these commands. Hence, one can approximately describe the robot's actual shape using estimated gait parameters and use that information to achieve adaptive locomotion. Using this method in [11], adaptive control for the snake robot in a pipe with varying diameters is proposed, which showed satisfactory results in the experiments. Similar work has also been reported by Travers in [93], where the authors use the measured motor torque and employ it as a feedback signal from the environment to modulate the gait parameters for obstacle-aided locomotion in XY plane, similar to a CPG based controller with environmental feedback.

2.5.2.2 Locomotion on surfaces with irregularities

The next group of works are concerned with the locomotion on uneven terrain. Such irregularities on the surface beneath the robot could be very small compared to the size of the robot link, hence they can be modelled by varying the friction property of the surface. To design an adaptive locomotion pattern suitable for such environments, some works such

as [94] and [95] have used body friction and tilt angle feedback, respectively to adaptively change parameters of a gait pattern. Similar methods has also been employed with the use of CPGs, where the CPG parameters are tuned for achieving a desired locomotion pattern by changing the frequency, amplitude, phase lags, or waveforms of the GPC output [62].

Unlike adaptive locomotion on surfaces with varying friction property, the number of works on adaptive locomotion of wheel-less snake robots in environments with large irregularities (compared to the dimension of the modules) are quite limited. In such environments the robot should climb over the obstacles to move forward, similar to walking on uneven terrain [8]. For the snake robot to deal with this situation, some works such as [64] have considered off-line path planning based on a segmented model and prior information about the obstacle size to generate a sequence of suitable body shape for the robot to climb over an obstacle. Other works, such as [13] have proposed a shape-based control scheme based on a curve-based approach, which also requires prior information about the environment. Others, such as [96], have targeted this issue by employing genetic programming to optimize the simulated snake motion, which is also an offline approach not suitable for online adaptive locomotion.

Overall, effective locomotion on surfaces with irregularities are less studied. However, such scenario, in which the robot should lift its body to climb over obstacles is very common in real world environments and very important for the snake robot to deal with. Although, the aforementioned control methods partially address this problem, these approaches cannot be implemented on modular snake robots in real-time. This suggests that, more research is required to design an effective controller for the snake robot moving on surfaces with irregularities employing on board sensing devices.

2.6 Summary

In this chapter, the most important aspects of snake-like, wheel-less locomotors were discussed and available literature were reviewed. A background on early works in the field of biological snake mechanism was presented and the major works concerning design, modelling and control of snake robots with focus on their locomotion capabilities were investigated. The provided comprehensive literature review revealed that, more research on design, modeling and control of snake robot is required to develop a snake robot capable of locomotion in environments with irregularities. In particular, the provided literature review showed that, design of a cost-effective snake robot with an effective force/torque sensing mechanism with a simple manufacture process requires more research. Moreover, this chapter showed that modelling of such robotic mechanism capable of efficient handling of contact forces should be investigated in more details. Additionally, the provided results also showed that to adaptively control a wheel-less snake robot on surfaces with irregularities more research should be conducted and new methods should be developed.

3

DESIGN AND DEVELOPMENT OF A MODULAR SNAKE ROBOT WITH SEAs FOR LOCOMOTION ON SURFACES WITH IRREGULARITIES

3.1 Introduction

In unstructured environments, there are different challenges, such as obstacles, uneven terrains and confined spaces, which are difficult to overcome by a robotic system. Snake robots have desirable characteristics, similar to their natural counterparts, which make them suitable for locomotion in such environments. However, development of effective snake-like mechanisms requires sensing devices, mechanical parts and electronic systems to be carefully designed and work in harmony. This chapter introduces the design of a modular

snake robot for effective locomotion on surfaces with irregularities. The development process of this modular snake robot with a torque sensing system embedded inside of each joint is presented, the snake robot modules design is given and the electronics system architecture of the robot is introduced.

3.2 Design Considerations

Choosing a suitable sensing mechanism, designing the robot modules and devising a digital control system to ensure effectiveness of the robot design for locomotion on surfaces with irregularities with emphasis on the simplicity and cost-effectiveness of the manufacturing process are the most important considerations in designing the snake robot.

3.2.1 Sensing mechanism

To design an effective control scheme for snake-like robots for operation in real word environments, sensing is a necessary ingredient. Unlike in human walking, where a visual feedback signal from the eyes is available, biological snake gathers information from the environment by sensing the contact forces. As these contact forces between the robot and the environment are responsible for generating the motion, such sensing mechanism seems to be suitable for a snake-like robot as well. Such information can be gathered via force sensors on the surface of the robot links or a torque sensor at each joint.

Considering the limited available space when dealing with snake robots, designing a custom built compact force/torque sensing mechanism is required. Hence, many researches have targeted design of snake robots with force/torque sensors in order to take advantage of torque/force feedback signal for more intelligent and agile snake locomotion. Prior works,

such as [17] with FSRs (force sensitive resistors), [23] with strain gauges and [22] with a complex custom made torque sensing system based on a cam mechanism, have tried to equip their snake robots with a sensitive torque/force sensing system. However, such systems are either complex or require the sensing device to be attached to the surface of the links, which put them at the risk of damage. Other works, such as [68], have proposed a snake robot equipped with Series Elastic Actuators (SEA), which are capable of measuring the small values of torque by measuring the displacement of the elastic element. However, manufacturing of such SEA requires compression moldings and a relatively complicated process for bonding the rubber to the metallic material at each joint.

The use of Polyurethane-based compliant elements for turning conventional servos into a SEA has proven to be very effective for robotic arms in [97]. Employing this idea reduces the cost of the prototype considerably while still providing precise torque feedback, which can be used for effective snake locomotion on surfaces with irregularities. Consequently, designing a Polyurethane based elastic element attached between the robot links and the servo motor at each joint, i.e. embedded inside each joint, has been considered the first step toward designing the snake robot. This will be discussed in section 3.3.

3.2.2 Snake robot module design

The most important factor in the mechanical design of the snake robot modules is the locomotion pattern that the robot should be capable to perform. Hence, it is critical to choose a snake-like locomotion pattern suitable for dealing with surfaces with irregularities and then design the robot modules accordingly.

Among the snake robot locomotion patterns, rectilinear (pedal wave) motion [13], which is similar to caterpillar motion [98], is an effective locomotion pattern very similar

to lateral undulation but performed in vertical plane. Unlike in biological snakes in which the amplitude of such vertical waves propagating along the snake body is very small [35], in a snake robot the maximum amplitude of such vertical waves can be larger. Hence, snake robots can potentially generate the rectilinear motion with higher amplitude, which makes it more suitable for climbing over obstacles compared to the rectilinear motion performed by biological snakes. In the rest of this thesis, inspired by early studies on this motion, such as [13], this locomotion pattern is just referred to as pedal wave motion when performed by the snake robot to emphasize on its difference with rectilinear motion of biological snakes.

Using pedal wave motion, the robot can lift its body to climb over the obstacles making it useful for locomotion on surfaces with irregularities, where lateral (horizontal) undulation might not be an applicable locomotion pattern. Using the pedal wave motion the robot can take advantage of the small cross section of its body to move in confined spaces. Moreover, because the robot pushes against the ground to move forward, existence of sideways push points no longer have an effect on the generation of such movement. Hence, a snake robot capable to perform such locomotion pattern has the potential to overcome the difficulties of moving in very challenging environments, where other robotic platforms have difficulties to operate in.

Consequently, to design the robot modules allowing the snake robot to perform pedal wave motion, design of the modules with octagonal cross-section was considered to make sure the surface in contact with the ground is smooth and the space inside the robot module is enough to accommodate the servo motor and the sensory system. Such design also allows to use the designed snake robot to perform undulation in horizontal plane due to the symmetrical design of the modules. This will be discussed in section 3.4 giving more details about the proposed design.

3.2.3 Control system architecture

The control system is a very important aspect of the snake robot design. As the snake robot will have many actuated joints, each with a torque sensor, the control system will be necessarily complex. The local controller at each joint depends not only on the feedback from its own torque sensor but from the torque and position sensor of neighboring joints and the input from a high level controller (operator). Such control system is shown in Figure 3.1.

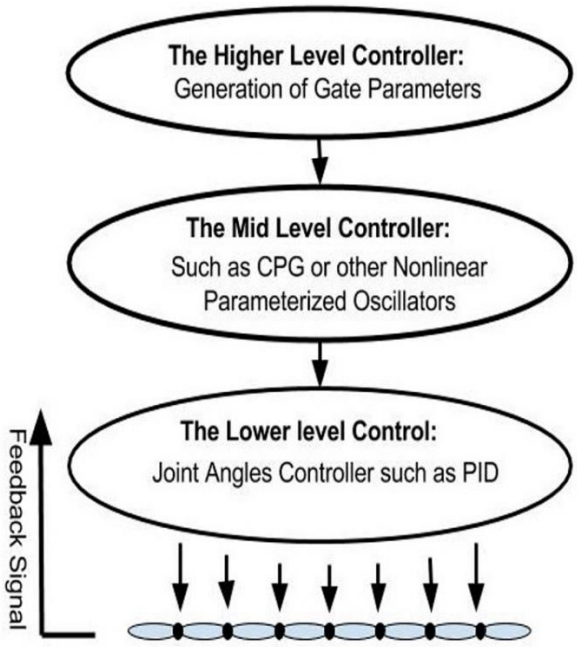

Figure 3.1. The snake robot control structure.

As it can be seen in Figure 3.1, the first layer (Lower level controller), makes sure that the measured angles of each joint matches with the desired angles with the use of a proportional-integral-derivative (PID) controller. The second layer (Mid-level), is responsible for generating the desired joint angles that feed into the first control layer, similar to the gait pattern presented in (2.6). Finally, the High-Level controller can be considered similar to the brain of the animal or the operator of the robot. This layer

determines the overall trajectory of the snake robot as a whole (by controlling the parameters of the oscillator) and feed into the Mid-level controller.

To design a control structure according to Figure 3.1, in addition to a central microcontroller, each joint should be equipped with local microcontrollers, responsible for communicating with the master controller, processing the sensory information and possibly sending messages to the neighbouring joints. Hence, to implement such control system a sophisticated communication system is also required to be designed, which will be discussed in section 3.5.

3.3 Design of the SEA

In snake-like robots, the size, joint design and the weight of the robot restrict our choices for the actuators. It is possible to use highly geared servo systems to achieve high output torque and reduce the size of the actuator. However, these highly geared servo systems, introduce several disadvantages, such as backlash, friction and gear break down [99], which makes torque estimation based on motor current very inaccurate. One way to solve this issue is to make the actuator "softer" and sacrifice the position control loop bandwidth to measure the motor output torque [100].

With this idea, the motor torque can be measured directly on the shaft by measuring the deflection of an elastic element (with known stiffness) between the load and the motor output shaft. These Series Elastic Actuators (SEA) are proved to be effective devices [101], making it possible to measure the torque based on the deflection of the spring like material. Moreover, using these types of actuators any external, sudden, and large force on the output

shaft, which is the main reason for gear damage will be minimized makes the interaction between the robot and environment much safer. Energy storage is another advantage of these actuators, which makes some tasks, such as producing legged locomotion more efficient [102].

Design and manufacture of an elastic element to be attached between the motor and the link is problematic. Existing designs, such as [101] typically use steel based torsional springs, suitable for large motors. Other designs, such as [68] requires compression moldings with a complicated manufacture process. However, Polyurethane-based compliant elements for robotic arm [97] have a less complicated design and manufacturing process, which can also be used for snake robots. In the following section the steps toward designing such a compliant element will be discussed.

3.3.1 Design and manufacture of a Polyurethane-based elastic element

To design the Polyurethane-based elastic element to be placed between the servo motor and each robot link, it is necessary to determine the material, the size of the element depending on the servomotor and the desired stiffness. For the snake robot design, the main consideration is to make the joints of the robot as light as possible, maximize the deflection of the elastic element when applying $0.05\ N.m$ (less than 5% of the maximum torque of the selected servo motor) and make sure that small displacement of the elastic element (based on the range of the motion of each joint) is enough for spanning the whole range of the change of the motor torque (based on the estimated length of the links, weight of the selected servo motor and the range of the motion of each joint) using a 12-bit encoder. For the elastic material, Polyurethane sheet with a thickness of 6mm and Shore Hardness of 95A proved

to be suitable and accessible, hence it was chosen as the material of the design. To decide on the shape of the element, motivated by the work in [97] an initial design with “S” shape blades connecting two concentric rings as shown in Figure 3.2 were chosen to be modified based on Finite Element Analysis (FEA) and optimization process to achieve desired specifications.

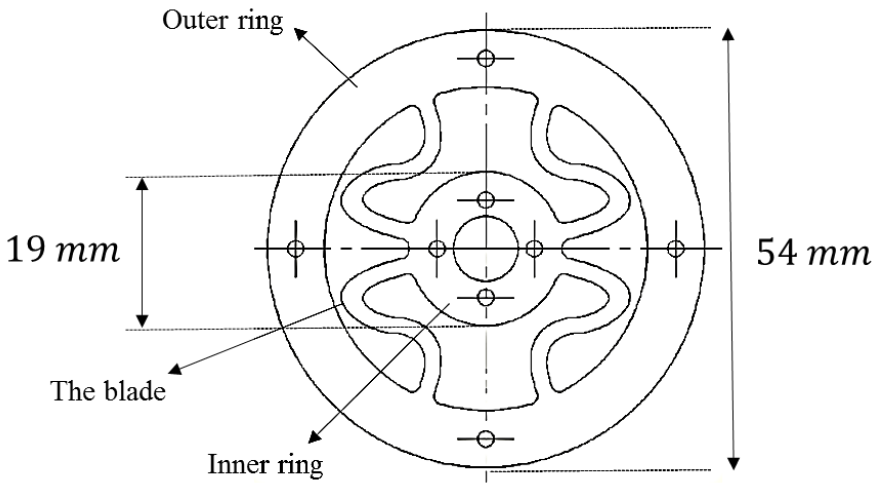

Figure 3.2. The initial design of the elastic element, showing the inner ring, outer ring and the "S" shaped blades

The simulation based tests conducted by applying $0.05\ N.m$ torque to the outer ring while holding the inner ring fixed, which revealed that the compliance predominantly depends on the shape and thickness of the "S" shape blades. Considering the design specifications, these two factors have been modified and as a result, the optimum width of the blades was found to be $2.5\ mm$ with the blades shape shown in Figure 3.3. The results of the FEA conducted on the final prototype is also shown in Figure 3.4, where the maximum displacement is shown in red.

Although in [97], it is claimed that the final part can be manufactured with a CNC router without using any refrigeration fluid, this method was found to be impractical, due to the flexibility of the material. Hence, once the design was optimised based on simulation

results, the final part was manufactured by waterjet cutting method as shown in Figure 3.5, which is a relatively simpler and more cost-effective manufacturing process, compared to compression molding used in [68].

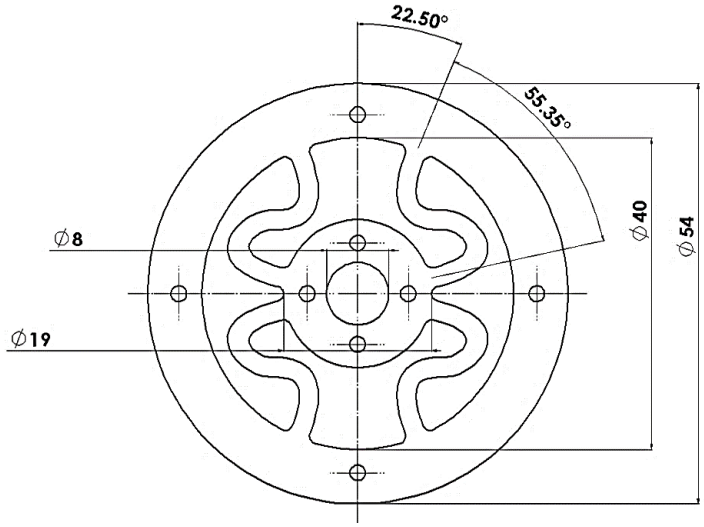

Figure 3.3. Computer Aided Design (CAD) model of the final elastic element design (dimensions are in millimetres).

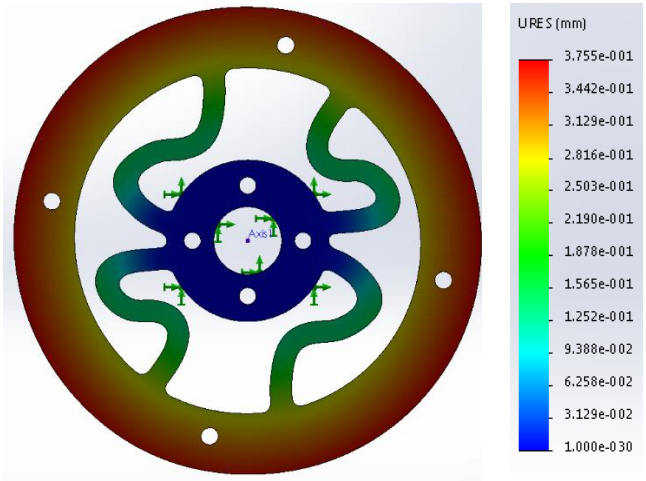

Figure 3.4. Finite element analysis results, showing the maximum displacement in red, with curvature based mesh with maximum and minimum element size of 2 mm and 0.7 mm, respectively, where the mass density of the material is 1.22 $gr.cm^{-3}$ and the elastic, modulus is 0.150 Gpa.

It should be mentioned that the initial dimensions of the elastic element, was chosen to be as shown in Figure 3.2 because the inner ring of the elastic element should be attached

to a servo motor, which is chosen to be Herkulex smart servo (DSR-0101). This will be discussed in more details in the following sections.

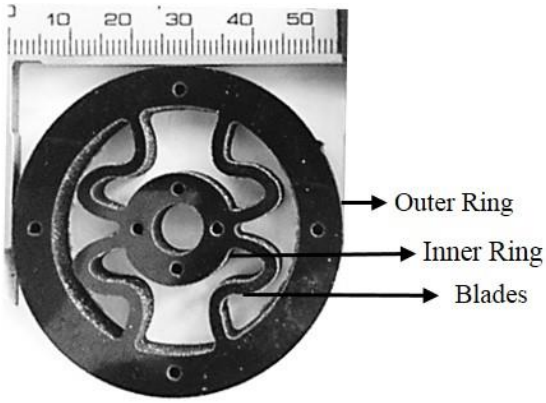

Figure 3.5. The final manufactured elastic element.

To calibrate and test the final manufactured part, a 12bit digital magnetic encoder (Ams, AS5145), was acquired and a specific sensor holder was designed specifically to accommodate the sensor as shown in Figure 3.6. Figure 3.7 also shows how these elements should be assembled.

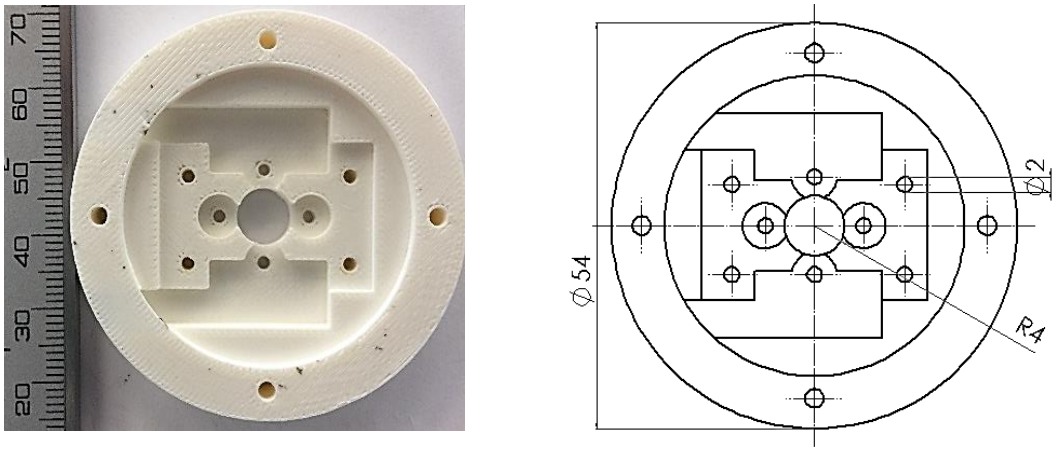

(a) 3D printed sensor holder with Acrylonitrile Butadiene Styrene (ABS).

(b) CAD model of the sensor holder.

Figure 3.6. The sensor holder designed to accommodate the encoder, manufactured by a 3D printer with ABS.

As shown in Figure 3.7, the magnet will be attached to the inner ring of the elastic element and the sensor will be attached to the sensor holder, which is attached to the outer ring. Hence, only one encoder (the green plate (d) in Figure 3.7) is required to measure the relative displacement of the inner and outer ring.

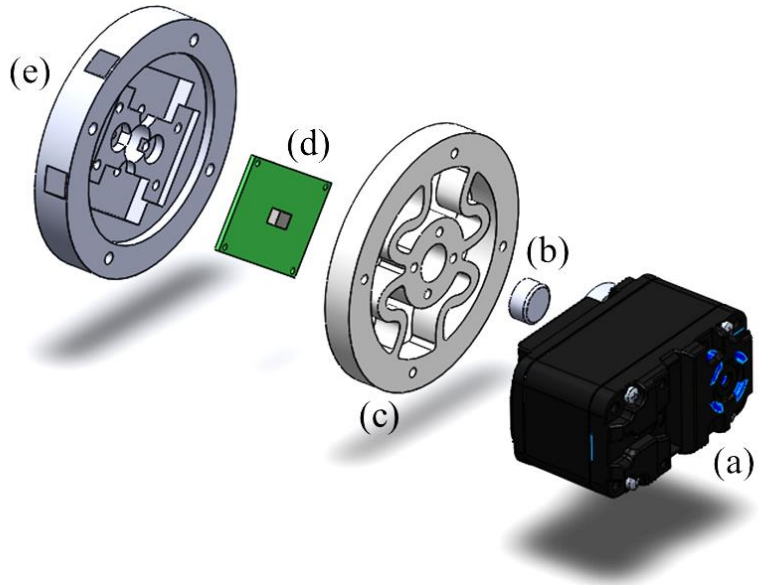

Figure 3.7. The final assembly of the sensing mechanism, where (a) is the servomotor (Herkulex, DSR-0101), (b) is the magnet for the sensor, (c) is the elastic element, (d) is the sensor board (Ams, AS5145) and (e) is the sensor holder.

Table 3.1 shows the specifications of the servo motor (Herkulex, DSR-0101) which is shown in Figure 3.7(a). As it can be seen in Table 3.1, the gear ratio of this servo motor is relatively high. This means that the value of the torque at the motor side (before the gear ratio), which can be estimated using the motor current is very small. Hence, it is hard to measure and very sensitive to noise. On the other hand, in a snake robot, a servo system with such high gear ratio is required due to the space limitation inside each joint of the robot. This is the reason why SEAs are suitable choices for measuring the motor torque in the proposed snake robot design.

Table 3.1 Specifications of the servo motor

Dimensions (mm)	45(W)×24(D)×31(H)
Weight (g)	45
Nominal input voltage (v)	7.4
Stall torque (kg.cm)	12
Maximum speed (rad/sec)	6.30
Rotation angle range (rad)	5.58
Gear ratio	1:256

3.3.2 Modelling and Calibration

To calibrate the elastic element a test rig was designed to use known weights to exert known forces to the outer ring while the inner ring is fixed and the relative angular displacement is being measured. The test rig manufactured by 3D printing using Acrylonitrile Butadiene Styrene (ABS). The test rig was designed to be as similar as possible to the final joint of the robot based on the initial desired specifications with the servo motor attached, even though it was not strictly necessary for the task.

To calibrate the elastic element, the servo motor was fixed at a complete horizontal position and the elastic element modelled as a torsional spring. The static equation then was obtained to be as shown in (3.1),

$$\tau_j + \tau_{arm} = K(\theta - q), \tag{3.1}$$

where τ_j (Nm) is the external moment acting on the link due to the weights attached to it, τ_{arm} is the moment due to the weight of the link, K $(N.m.rad^{-1})$ is stiffness coefficient of the spring to be obtained, θ is the motor angle and q (rad) is the link angle. Considering that weights will be attached to the link with the elastic element is in normal shape (i.e., $\theta =$

0), the distance between the point of the action of the external force to the center of rotation is known and the motor is fixed at a certain angle, (3.1) can be simplified to:

$$|\tau_j| = mgdcos(q) = K|q|, \tag{3.2}$$

where m is the mass of the attached weight and d the distance between the point of the action of the external force and the centre of rotation (see Figure 3.8).

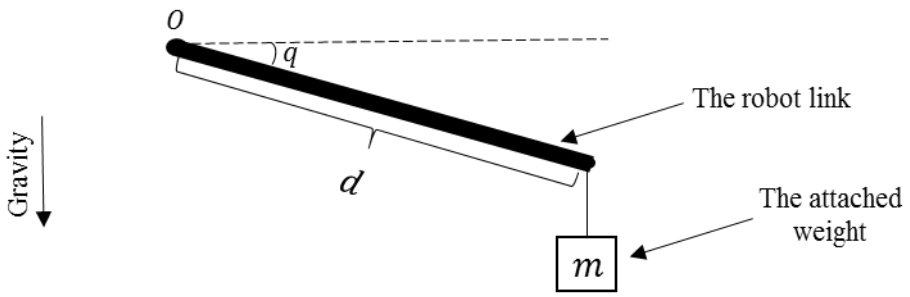

Figure 3.8. Diagram of the calibration test, showing the known weight m, and the link, which can rotate about the axis passing through O.

Using equation (3.2) the elastic element characteristics obtained and the results are shown in Figure 3.9. The resolution of the sensor was obtained to be $0.01\ N.m$, exceeding the design requirements. Based on the calibration results and considering a zero order system, the SEA modelled as a torsional spring with no damping, and spring constant $K = 1.74\ N.m.rad^{-1}$.

As can be seen in Figure 3.9, the elastic element showed a relatively linear behaviour. Although, any possible nonlinear behaviour due to the characteristics of the material or the shape of the blades could be taken into account, this behaviour of Polyurethane is highly desirable. No failure in the material was observed during testing with external torques up to $0.7\ N.m$. The only limitation towards testing the material subject to higher torque values was the blades coming into contact with the outer ring due to extreme deformation, i.e. relative angular deformation higher than 21 degrees, which makes the sensor reading

inaccurate. The maximum measurable torque can be increased, by increasing the difference between the diameter of the inner and outer ring or adjusting the shape of the blades.

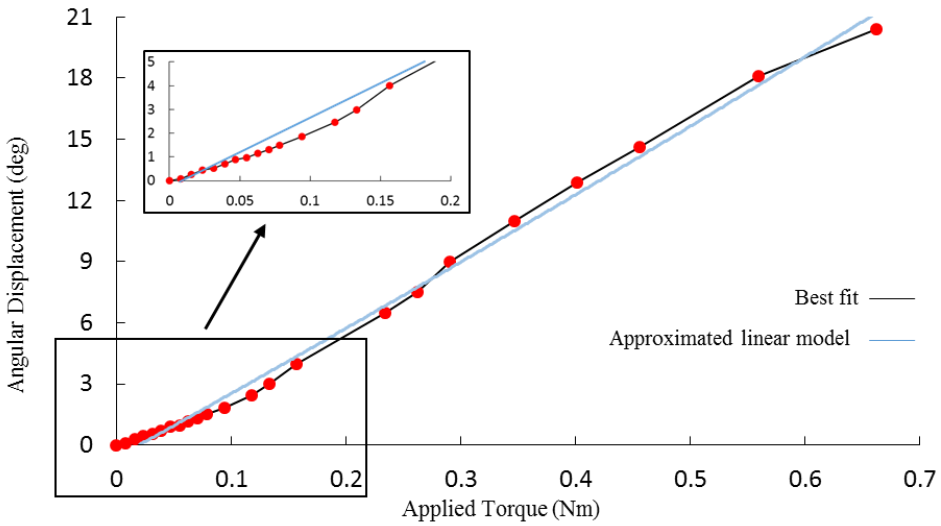

Figure 3.9. The calibration results for the elastic element, where the blue line shows the linear approximation.

3.4 Design of the Snake Robot Modules

In this section, design and manufacture of the snake robot modules, equipped with the SEA will be presented. Unlike other works, such as [24], the designed snake robot modules will not be equipped with wheels. Hence, this robot will be more suitable for locomotion in challenging environments, such as unstructured confined spaces and uneven terrains.

As shown in Figure 3.10, each module of the proposed design of the robot consists of two main parts. The link housing as shown in Figure 3.10 (a), is designed to accommodate the actuator, the custom made control board and the elastic element without interfering with the joint motion. The link connector in Figure 3.10 (b), connects each module to the following module, where hollow spaces are included for easy wiring.

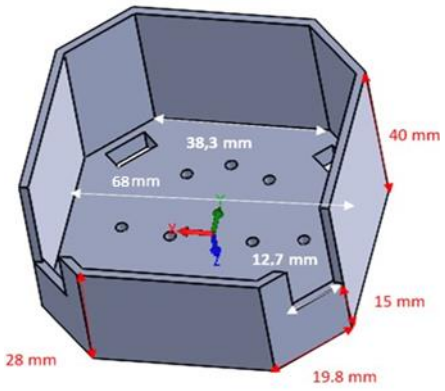

(a) Link housing with octagonal cross section.

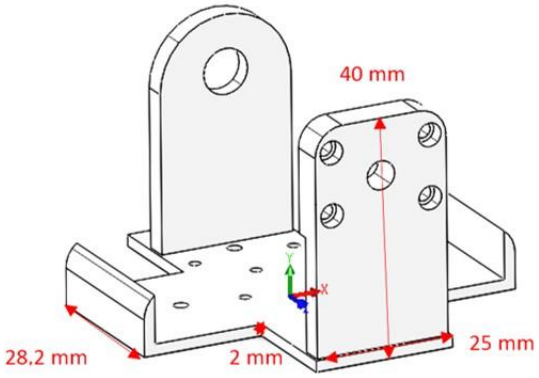

(b) Link connector.

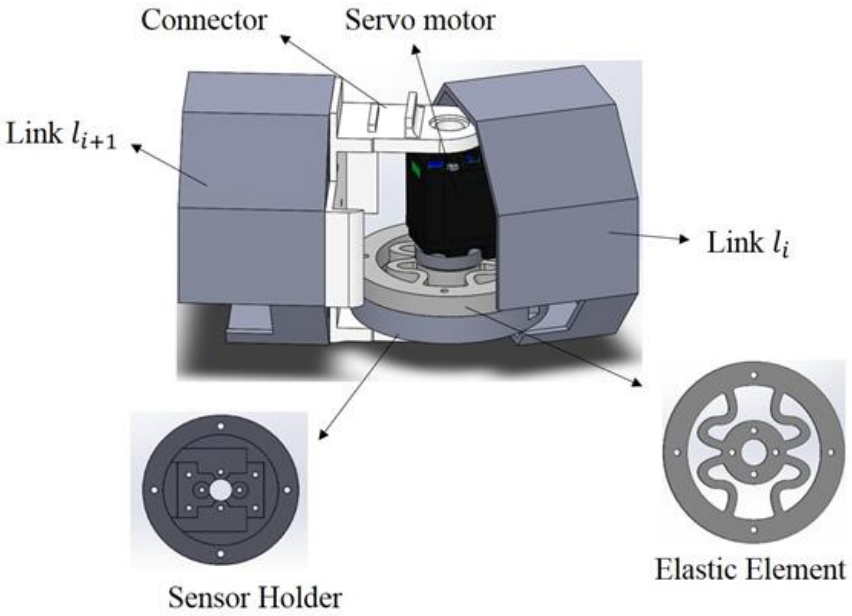

(c) Joint assembly.

Figure 3.10. Important concepts of each module.

Screw holes on the connector and the link housing are designed such that each joint can be connected to the previous joint with 0 or 90 degrees relative rotation about longitudal axis for possible 3D structure. This together with the symmetrical octagon shape of the links enable the same design to be used, without major changes for generating pedal wave motion,

lateral undulation in confined spaces, or 3D motion patterns. The final robot modules, were manufactured by cost-effective 3D printing using ABS with the elastic element embedded inside of each joint, which makes the torque measurement mechanisms more robust compared to existing designs with strain gauges, which are attached to the surface of the links [23].

The tail module of the snake robot is also a critical part of the robot because it connects the joints to the power supply and also to the master microcontroller. Thus, the tail module as shown in Figure 3.11, is designed to be similar to the rest of the body and as short as possible because the tail should be attached to the last link of the robot and a long tail can interfere with the locomotion of the snake robot. Moreover, as the robot is connected to an external power supply and the master microcontroller, a slip ring was also adapted to make sure the wires will not interfere with the robot motion, which is major concern especially if the robot is performing 3D gait patterns, such as rolling [85] or sidewinding [58] .

3.5 Control System Architecture

An electronic system is needed to be designed to equip each link of the robot with a custom made circuit board for power distribution, communication, data acquisition and control. Teensy microcontroller with 32 bit ARM Cortex-M4 72MHz CPU (Teensy 3.2, PJRC) was chosen as a microcontroller with embedded Controlled Area Network (CAN) bus module and an on-board $3.3\,V$ voltage regulator ideal for powering the magnetic encoder. Additionally, a voltage regulator (STMicroelectronics, L7805CV) is used to power the micro-controller and a proper CAN bus transceiver (Texas Instruments, SN65HVD23X) is also employed for converting the digital data into suitable physical signal on the bus.

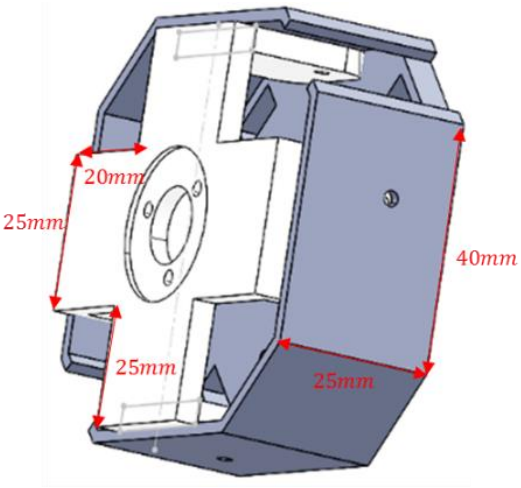

Figure 3.11. Tail module design.

Implementation of serial communication for sending and receiving data to and from the servo systems and managing the extra wiring for gathering data from the digital encoder requires designing a custom made Printed Circuit Board (PCB). For this purpose a circuit board is designed using Altium Designer (Version 16.1.12) and manufactured, which could be embedded inside of each joint. The manufactured PCB is shown in Figure 3.12.

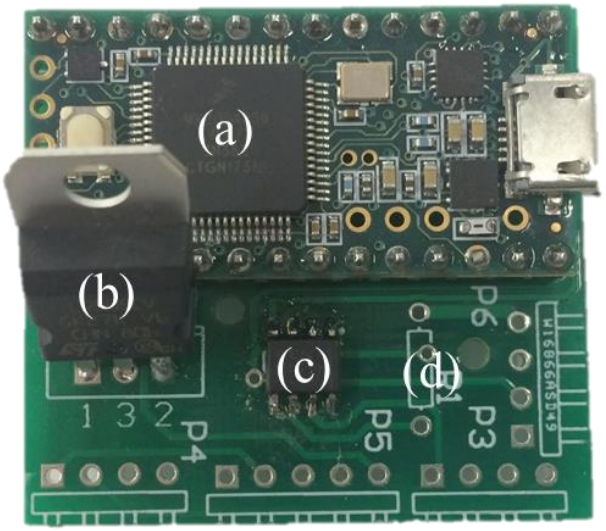

Figure 3.12. The Printed Circuit Board (PCB) of the joint controller with dimensions 38mm× 34mm, where (a) is the Teensy 3.2 microcontroller, (b) is the voltage regulator (STMicroelectronics, L7805CV), (c) is the CAN transceiver (Texas Instruments, SN65HVD23X) and (d) is the termination resistor.

By using this control board, which is also used as the main controller, each module can directly receive information as a command from the externally located main controller (implemented on the same PCB) using the communication system designed based on CAN bus. Moreover, each module can request data form other joints on the bus or the central controller, which makes the design versatile and allows implementation of closed-loop motion controllers, where feedback from neighbouring joints is necessary.

The final cost of each module, including the magnetic encoder (12 USD), the 3D printed module (3 USD), the elastic element (4 USD) and the PCB (18 USD) obtained to be 37 USD. This is an estimated final cost including the shipping and labour cost in Christchurch, New Zealand excluding the servo motor price (39.50 USD), which can be replaced by cheaper servo motors by modifying the joint dimensions.

3.6 Final Snake Robot Prototype Overview

Using the modular design concept with the details revealed in the previous sections, a snake robot with six links is manufactured and assembled as shown in Figure 3.13.

Figure 3.13. The final manufactured snake robot.

As shown in Figure 3.13, identical robot modules are connected to each other to assemble the snake robot, with servos connecting each joint to the next one, with parallel axes of rotation. The specifications of the snake robot are presented in Table 3.2.

Table 3.2 Overview of the developed snake robot

Dimensions	Total length: 445 *mm* Diameter: 68 *mm*
Total weight	956 g
Number of links	6
Nominal input voltage	9.2 V
Communication	Can Bus (1 Mbit/sec)
Maximum joint angular displacement	$\pm 60°$
Sensing	Joint angle (with the resolution of 0.32°) Output torque (with the resolution of 0.01 $N.m$)

The modular design of the robot, as shown in Figure 3.13 has the flexibility to increase or decrease the length of the robot by connecting more joints (without the need to change the embedded electronics). This can be beneficial to achieve more degrees of freedom and fault tolerance. However, attaching more joints will increase the weight, the number of required servo motors and consequently the power consumption and cost of the robot. Hence, in this thesis, the robot with six links was assembled, which its effectiveness for achieving forward pedal wave motion will be discussed in the following chapters.

3.7 Summary

This chapter presented the design of a cost-effective wheel-less snake robot with a torque sensing mechanism achieved using a polyurethane based elastic element between the links and the motors. Employing this idea, an elastic element with the desired shape and stiffness using easily accessible polyurethane sheet with the thickness of $6\,mm$ was designed and manufactured to be attached between the links and the motors. The sensor was calibrated and the resolution and stiffness of the sensor obtained to be $0.01\,N.m$ and $1.74\,N.m.rad^{-1}$, respectively. This torque measurement mechanism is embedded inside of each joint. Hence, unlike existing ones, such as [23], in which the sensing device should be attached to the surface of the links is more robust. The robot modules were also manufactured with a cost effective 3D printer with ABS based on a symmetrical octagonal-shaped design, which together with the digital control system with local microcontrollers embedded at each joint allowed development of a snake robot with six identical links potentially suitable for pedal wave locomotion on surfaces with irregularities.

4

DYNAMICAL MODELLING OF PEDAL WAVE LOCOMOTION OF MODULAR SNAKE ROBOTS WITH SEAs

4.1 Introduction

Development of a dynamical model for the snake robot presented in chapter 3 is a critical step towards understanding the fundamentals of pedal wave motion and investigation of the effect of varying environmental conditions, such as friction, external forces and terrain features on the motion of the robot. However, several degrees of freedom, flexibility at the joints and the contact forces exerted on the robot from the environment make the dynamical modelling of the snake robot developed in the previous chapter very challenging.

In this chapter, the Euler-Lagrange equations of motion of modular 2D snake robots with SEAs (i.e. all joints have parallel axis of rotation) will be introduced. Considering a segmented model of the robot, kinematics of the robot in the vertical plane will be obtained in an efficient matrix form. Moreover, with the use of a spring-damper contact model (Kelvin–Voigt model), the environmental forces will be modelled and incorporated into the dynamical equations, which enables to simulate the robot pedal wave motion on surfaces with irregularities. Finally, to generate pedal wave motion with the use of the presented dynamical model, a position controller will be designed at the joint level allowing to track the desired gait pattern.

4.2 Euler-Lagrange Equations of Motion

Considering the number of degrees of freedom of the snake robot, Euler-Lagrange method is a straightforward approach, which can be employed to obtain the equations of motion of the snake robot [103]. Using this method, the external contact forces can be incorporated into the equations, the effect of the springs at each joint can be taken into account through the expression for the potential energy of the system and the gravitational forces can easily be handled. Thus, compared to Newton's method, Euler-Lagrange method can be used to derive the dynamical equations of the snake robot pedal wave motion in the vertical plane with less effort.

Choosing the generalized coordinates, i.e. the minimum number of variables required to fully describe the system, to be denoted by $\boldsymbol{q}$, the Euler-Lagrange equations of motion can immediately be constructed as follows:

$$\frac{d}{dt}\left(\frac{\partial(T_1+T_2)}{\partial \dot{\boldsymbol{q}}}\right)-\frac{\partial(T_1+T_2)}{\partial \boldsymbol{q}}+\frac{\partial(V_1+V_2+V_3)}{\partial \boldsymbol{q}}=\boldsymbol{\mathcal{B}U}+\boldsymbol{Q}^c \tag{4.1}$$

where T_1 and T_2 are the kinetic energy of the links and the rotors respectively, V_1 is the potential energy stored in the flexible elements (torsional spring) at the joints, V_2 and V_3 are the potential energy of the links and the rotors due to the gravitational force, $\boldsymbol{\mathcal{B}}$ is a matrix of size $2N+1\times(N-1)$, $\boldsymbol{U}$ is the column vector of $N-1$ control inputs (motor torques), N is the number of robot links and $\boldsymbol{Q}^c$ is the vector of non-conservative contact forces, such as contact or friction forces.

To fully obtain the Euler-Lagrange equations of motion, clearly one should obtain the expression for the kinetic and potential energy of the system at the first place and then model the external forces acting on the robot. However, considering the number of degrees of freedom of the system, it is convenient to first obtain the kinematics of such motion in a matrix form and use the obtained relations to derive the expressions for both kinetic and potential energy of the system.

4.3 Kinematics of 2D Snake Robots with Flexible Joints

A modular snake robot with N identical links ($l_i; i=1,2,\dots,N$) and $N-1$ actuators ($r_j; j=1,2,\dots,N-1$) with the same gear ratio of n attached in series with a spring to the corresponding link, is illustrated in Figure 4.1. In this figure, θ_i^l and θ_j^r are the absolute link and rotor angles, respectively, which are measured from the positive x-axis. $\alpha_j=\theta_j^l-\theta_{j+1}^l$ is the angle between the consecutive links j and $j+1$, $\beta_j=\theta_j^l-\theta_j^r$ is the j^{th} rotor angle relative to its stator reflected through the link side (after the gear train), $\left[x_i^l, z_i^l\right]^{\mathrm{T}}$ and

$[x_j^r, z_j^r]^{\mathrm{T}}$ are the position of the centre of mass of link l_i and rotor r_j in the global coordinate frame, respectively and $[p_x, p_z]^{\mathrm{T}}$ denotes the centre of mass of the robot.

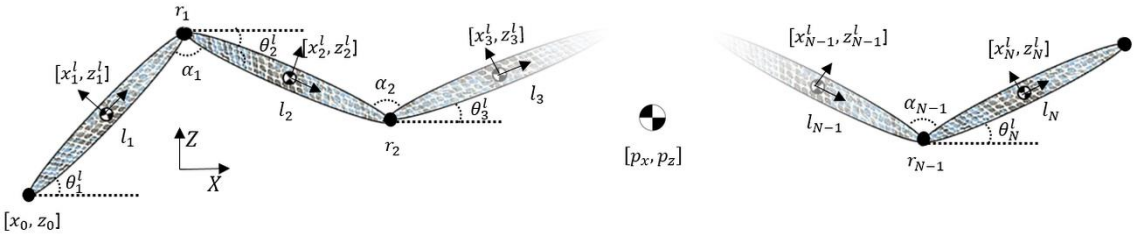

Figure 4.1. 2D snake robot body shape.

It should be noted that the rotor angles and the flexible elements at each joint are not shown in Figure 4.1. The reason is that, considering the relative link angles α_j, the body shape of the robot is independent of the rotor angles β_j, hence they were neglected for more clear presentation. The Figure 4.2 better shows the angles defined for a single joint of a snake robot with SEAs, where the stator is directly attached to the link.

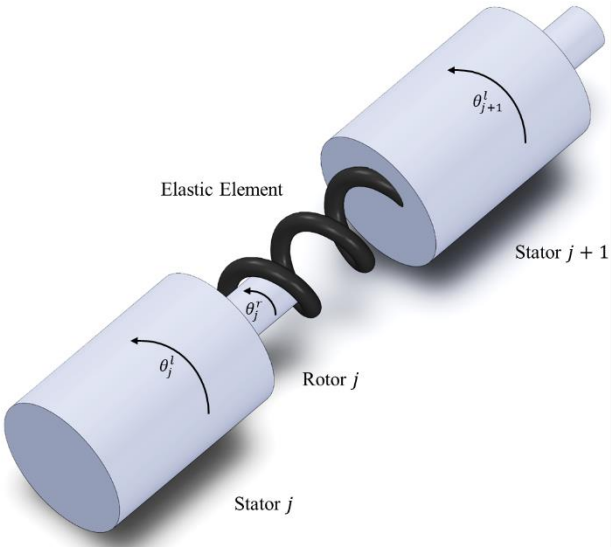

Figure 4.2. The defined angles in each snake robot joints.

To obtain the expression for the kinematics and dynamics of the snake robot in matrix form, it is convenient to define several matrices and vectors as follows:

$$\mathcal{H}^l = \begin{bmatrix} l & 0 & 0 & \dots & 0 \\ 2l & l & 0 & \dots & 0 \\ 2l & 2l & l & \dots & 0 \\ \vdots & \vdots & \vdots & \vdots & \vdots \\ 2l & 2l & 2l & \dots & l \end{bmatrix}_{N\times N}, \qquad \mathcal{H}^r = \begin{bmatrix} 2l & 0 & 0 & \dots & 0 & 0 \\ 2l & 2l & 0 & \dots & 0 & 0 \\ 2l & 2l & 2l & \dots & 0 & 0 \\ \vdots & \vdots & \vdots & \vdots & \vdots & 0 \\ 2l & 2l & 2l & \dots & 2l & 0 \end{bmatrix}_{N-1\times N},$$

$$\boldsymbol{C\theta} = \begin{bmatrix} cos(\theta_1^l) \\ cos(\theta_2^l) \\ \vdots \\ cos(\theta_N^l) \end{bmatrix}, \boldsymbol{S\theta} = \begin{bmatrix} sin(\theta_1^l) \\ sin(\theta_2^l) \\ \vdots \\ sin(\theta_N^l) \end{bmatrix}, \qquad \mathcal{F} = \begin{bmatrix} 1 & 1 & 1 & \dots & 1 \\ 0 & 1 & 1 & \dots & 1 \\ 0 & 0 & 1 & \dots & 1 \\ \vdots & \vdots & \vdots & \vdots & \vdots \\ 0 & 0 & 0 & \dots & 0 \end{bmatrix}_{N\times N-1},$$

$$\mathcal{S}_\theta = diag(\boldsymbol{S\theta}) = diag\left(sin(\theta_1^l), sin(\theta_2^l), \dots, sin(\theta_N^l)\right),$$

$$\mathcal{C}_\theta = diag(\boldsymbol{C\theta}) = diag\left(cos(\theta_1^l), cos(\theta_2^l), \dots, cos(\theta_N^l)\right),$$

$$\mathcal{O}_l = \mathcal{O}_r = 0_{N\times(N-1)}.$$

where $0_{N\times(N-1)}$ is an $N \times (N-1)$ zero matrix. Moreover, the denominator-layout notation is employed to calculate various derivatives with respect to vectors and scalars as defined in the following:

$$\frac{\partial \boldsymbol{X}_m}{\partial y} = \begin{bmatrix} \frac{\partial x_1}{\partial y} & \frac{\partial x_2}{\partial y} & \dots & \frac{\partial x_m}{\partial y} \end{bmatrix}$$

$$\frac{\partial \mathcal{W}\boldsymbol{X}_m}{\partial \boldsymbol{X}_m} = \mathcal{W}^{\mathrm{T}}$$

$$\frac{\partial \boldsymbol{X}_m{}^{\mathrm{T}}\mathcal{W}\boldsymbol{X}_m}{\partial \boldsymbol{X}_m} = (\mathcal{W} + \mathcal{W}^{\mathrm{T}})\boldsymbol{X}_m$$

where y is a scalar, $\boldsymbol{X}_m = [x_1 \quad x_2 \quad \dots \quad x_{\mathrm{m}}]^T$ and $\mathcal{W}_{m\times m}$ is an $m \times m$ matrix.

4.3.1 The links linear and angular velocity

Considering the body shape of the robot in Figure 4.1 and assuming that $l_1 = l_2 = \cdots = l_N = 2l$ for simplicity, the position of the centre mass of each link can be derived as the function of absolute joint angles as follows:

$$x_i^l = x_0 + 2l\sum_{k=1}^{i-1} cos(\theta_k^l) + l\,cos(\theta_i^l) \tag{4.2}$$

$$z_i^l = z_0 + 2l\sum_{k=1}^{i-1} sin(\theta_k^l) + l\,sin(\theta_i^l), \tag{4.3}$$

which with little effort can be written in matrix form as below:

$$\boldsymbol{X}^l = \boldsymbol{V}^l x_0 + \mathcal{H}^l \boldsymbol{C\theta} \tag{4.4}$$

$$\boldsymbol{Z}^l = \boldsymbol{V}^l z_0 + \mathcal{H}^l \boldsymbol{S\theta}, \tag{4.5}$$

where $\boldsymbol{X^l} = [x_1^l \quad x_2^l \quad ... \quad x_N^l]^{\mathrm{T}}$, $\boldsymbol{Z^l} = [z_1^l \quad z_2^l \quad ... \quad z_N^l]^{\mathrm{T}}$and $\boldsymbol{V}^l = [1 \quad 1 \quad ... \quad 1]^T$.

Considering that $p_x = 1/N(\boldsymbol{V^l})^{\mathrm{T}} X^l$ and $p_z = 1/N(\boldsymbol{V^l})^{\mathrm{T}} Z^l$, x_0 and z_0 can be eliminated from (4.4) and (4.5). Hence, taking their derivative with respect to time, the velocity of the centre of mass of each link can immediately be obtained to be:

$$\dot{\boldsymbol{X}}^l = \boldsymbol{V}^l \dot{p}_x + \frac{1}{N}\boldsymbol{V}^l(\boldsymbol{V}^l)^T \mathcal{H}^l \mathcal{S}_\theta \dot{\boldsymbol{\theta}}^l - \mathcal{H}^l \mathcal{S}_\theta \dot{\boldsymbol{\theta}}^l \tag{4.6}$$

$$\dot{\boldsymbol{Z}}^l = \boldsymbol{V}^l \dot{p}_z - \frac{1}{N}\boldsymbol{V}^l(\boldsymbol{V}^l)^T \mathcal{H}^l \mathcal{C}_\theta \dot{\boldsymbol{\theta}}^l + \mathcal{H}^l \mathcal{C}_\theta \dot{\boldsymbol{\theta}}^l, \tag{4.7}$$

where $\dot{\boldsymbol{\theta}}^l = [\dot{\theta}_1^l \quad \dot{\theta}_2^l \quad ... \quad \dot{\theta}_N^l]^{\mathrm{T}}$ is the vector of angular velocities of the links around the common Y axis, $\dot{\boldsymbol{X}}^l = [\dot{x}_1^l \quad \dot{x}_2^l \quad ... \quad \dot{x}_N^l]^{\mathrm{T}}$, $\dot{\boldsymbol{Z}}^l = [\dot{z}_1^l \quad \dot{z}_2^l \quad ... \quad \dot{z}_N^l]^{\mathrm{T}}$ and $\dot{p}_x$ and $\dot{p}_z$ are the linear velocities of the centre of mass of the robot in X and Z direction, respectively.

Noting that $\theta_i^l = \sum_{k=i}^{N-1}(\alpha_k) + \theta_N^l$ and defining the generalized coordinates to be $\boldsymbol{q} = \left[\alpha_1, \dots, \alpha_{N-1}, \theta_N^l, p_x, p_z, \beta_1, \dots, \beta_{N-1}\right]^{\mathrm{T}}$, it is possible to represent equations (4.6) and (4.7) explicitly as a function of $\boldsymbol{q}$ and $\dot{\boldsymbol{q}}$ as below:

$$\dot{\boldsymbol{X}}^{\boldsymbol{l}} = \left[\left(\mathcal{B}_1^l + \mathcal{A}^l \mathcal{S}_\theta \mathcal{C}\right) \quad \mathcal{O}_l\right]\dot{\boldsymbol{q}} \tag{4.8}$$

$$\dot{\boldsymbol{Z}}^{\boldsymbol{l}} = \left[\left(\mathcal{B}_2^l - \mathcal{A}^l \mathcal{C}_\theta \mathcal{C}\right) \quad \mathcal{O}_l\right]\dot{\boldsymbol{q}} \tag{4.9}$$

$$\dot{\boldsymbol{\theta}}^{\boldsymbol{l}} = [\mathcal{C} \quad \mathcal{O}_l]\dot{\boldsymbol{q}}, \tag{4.10}$$

where $\mathcal{B}_1^l = [0_{N\times N} \quad \boldsymbol{V}^l \quad 0_{N\times 1}]$, $\mathcal{B}_2^l = \left[0_{N\times(N+1)} \quad \boldsymbol{V}^l\right]$, $\mathcal{A}^l = -\mathcal{H}^l + \frac{1}{N}\boldsymbol{V}^l(\boldsymbol{V}^l)^{\mathrm{T}}\mathcal{H}^l$ and $\mathcal{C} = [\mathcal{F} \quad \boldsymbol{V}^l \quad 0_{N\times 2}]$ and $0_{N\times N}$ is N by N with all zero elements.

4.3.2 The robot rotor velocity

In addition to linear velocity of the centre of mass and the angular velocity of each link, the angular velocity of the rotor and the linear velocity of the centre of mass of the rotors should also be obtained to calculate the kinetic energy of the system. Considering the body shape of the robot shown in Figure 4.1, the position of the centre of mass of rotor r_j can be obtained to be:

$$x_j^r = x_0 + 2l\sum_{k=1}^{j} cos\left(\theta_k^l\right) \tag{4.11}$$

$$z_j^r = z_0 + 2l\sum_{k=1}^{j} sin\left(\theta_k^l\right), \tag{4.12}$$

which, similar to the previous section, can be written as:

$$\boldsymbol{X}^r = \boldsymbol{V}^r x_0 + \mathcal{H}^r \boldsymbol{C\theta} \tag{4.13}$$

$$\boldsymbol{Z}^r = \boldsymbol{V}^r z_0 + \mathcal{H}^r \boldsymbol{S\theta}, \tag{4.14}$$

where $\boldsymbol{X}^r = [x_1^r \quad x_2^r \quad \ldots \quad x_{N-1}^r]^{\mathrm{T}}$, $\boldsymbol{Z}^r = [z_1^r \quad z_2^r \quad \ldots \quad z_{N-1}^r]^{\mathrm{T}}$ and $\boldsymbol{V}^r = [1 \quad 1 \quad \ldots \quad 1]^{\mathrm{T}}_{(N-1)\times 1}$. Obtaining the derivate of the vector $\boldsymbol{X}^r$ and $\boldsymbol{Z}^r$ with respect to time, the velocity of the centre of mass of each rotor can be obtained to be:

$$\dot{\boldsymbol{X}}^r = [(\mathcal{B}_1^r + \mathcal{A}^r \mathcal{S}_\theta \mathcal{C}) \quad \mathcal{O}_r]\dot{\boldsymbol{q}}, \tag{4.15}$$

$$\dot{\boldsymbol{Z}}^r = [(\mathcal{B}_2^r - \mathcal{A}^r \mathcal{C}_\theta \mathcal{C}) \quad \mathcal{O}_r]\dot{\boldsymbol{q}}, \tag{4.16}$$

$$\dot{\boldsymbol{\theta}}^r = \mathcal{L}\dot{\boldsymbol{q}} \tag{4.17}$$

where $\mathcal{B}_1^r = [0_{(N-1)\times N} \quad \boldsymbol{V}^r \quad 0_{(N-1)\times 1}]$, $\mathcal{B}_2^r = [0_{(N-1)\times(N+1)} \quad \boldsymbol{V}^r]$, $\mathcal{A}^r = -\mathcal{H}^r + \frac{1}{N}\boldsymbol{V}^r(\boldsymbol{V}^l)^{\mathrm{T}}\mathcal{H}^l$, $\boldsymbol{V}^r = [1 \quad 1 \quad \dots \quad 1]^{\mathrm{T}}_{(N-1)\times 1}$, $\mathcal{L} = [\mathcal{C}_1 \quad -\mathcal{P}]$, $\mathcal{C}_1$ is the first $(N-1)$ rows of $\mathcal{C}$ (i.e. $\mathcal{C} = \left[\frac{\mathcal{C}_{1(N-1)\times(N+2)}}{\mathcal{C}_{2\,1\times(N+2)}}\right] = [\mathcal{F} \quad \boldsymbol{V}^l \quad 0_{N\times 2}]$ **)** and $\mathcal{P}$ is a $(N-1)$ by $(N-1)$ diagonal matrix of identical gear ratio (n) of the motors.

The presented procedure for obtaining the kinematic relations for the links and the rotors made it possible to obtain the position and velocity of the centre of mass of each link/rotor as a function of the joint angles α_i, the rotor angle β_j, the absolute angle of the head module and the position of the centre of mass of the robot in matrix form. Hence, to implement such equations, no symbolic computation is necessary, making the implementation of equations of motion to be presented in the next section very convenient. It should also be mentioned that, although the kinematic relations were obtained for the snake robot in vertical plane XZ, the same equations can describe the kinematics of lateral undulation in the horizontal plane, i.e., OXY, by only replacing Z axis with Y axis, without the need to consider the difference in the contact forces, which only affect the dynamics of the robot.

4.4 Derivation of the Kinetic Energy of the System

To fully derive the equations of motion of the robot in vertical plane, first, the expression for the kinetic energy of the system should be obtained. Considering the kinematic relations

obtained in the previous section, this can be done by obtaining the kinetic energy of the links and rotors to find the total kinetic energy of the system.

4.4.1 The kinetic energy of the links

Considering the generalized coordinates $\boldsymbol{q}$, it can be seen that the expression for the kinetic energy of the links, necessary for constructing the Euler-Lagrange equation is independent of rotor angles β_is, i.e. the body shape of the robot is independent of β_is. Hence, T_1 can be obtained to be only the sum of the kinetic energy of the links due to their own linear and angular velocity as follows:

$$T_1 = \frac{1}{2}\left(\dot{\boldsymbol{X}}^l\right)^T \mathcal{M}^l \left(\dot{\boldsymbol{X}}^{\boldsymbol{l}}\right) + \frac{1}{2}\left(\dot{\boldsymbol{Z}}^l\right)^T \mathcal{M}^l \left(\dot{\boldsymbol{Z}}^l\right) + \frac{1}{2}\left(\dot{\boldsymbol{\theta}}^l\right)^T \mathcal{J}^l \left(\dot{\boldsymbol{\theta}}^l\right) \tag{4.18}$$

where $\dot{\boldsymbol{X}}^l = [\dot{x}_1^l \quad \dot{x}_2^l \quad \dots \quad \dot{x}_N^l]^{\mathrm{T}}$, $\dot{\boldsymbol{Z}}^l = [\dot{z}_1^l \quad \dot{z}_2^l \quad \dots \quad \dot{z}_N^l]^{\mathrm{T}}$, $\dot{\boldsymbol{\theta}}^l = [\dot{\theta}_1^l \quad \dot{\theta}_2^l \quad \dots \quad \dot{\theta}_N^l]^{\mathrm{T}}$ and $\mathcal{M}^l$ and $\mathcal{J}^l$ are N by N diagonal matrices of mass and moment of inertia of the links, respectively. It is worthwhile to mention that, for a snake robot with stiff joints, the kinetic energy of the links as presented in (4.18) will be the only terms required to calculate the kinetic energy of the system and construct the equations of motion. The only consideration is that in this form the mass of each link should be the sum of the mass of the rotors and the links.

4.4.2 The kinetic energy of the rotors

To fully obtain the expression for the kinetic energy of the system, the kinetic energy of the rotors should also be taken into account. Similar to the method used in the previous section, the kinetic energy of the rotors can be obtained to be:

$$T_2 = \frac{1}{2}\left(\dot{\boldsymbol{X}}^r\right)^{\mathrm{T}} \mathcal{M}^r \left(\dot{\boldsymbol{X}}^r\right) + \frac{1}{2}\left(\dot{\boldsymbol{Z}}^r\right)^{\mathrm{T}} \mathcal{M}^r (\mathrm{Z}^r) + \frac{1}{2}\left(\dot{\boldsymbol{\theta}}^{\boldsymbol{r}}\right)^{\mathrm{T}} \mathcal{J}^r \left(\dot{\boldsymbol{\theta}}^{\boldsymbol{r}}\right) \tag{4.19}$$

where $\dot{\boldsymbol{X}}^r = [\dot{x}_1^r \quad \dot{x}_2^r \quad \dots \quad \dot{x}_{N-1}^r]^{\mathrm{T}}$, $\dot{\boldsymbol{Z}}^r = [\dot{z}_1^r \quad \dot{z}_2^r \quad \dots \quad \dot{z}_{N-1}^r]^{\mathrm{T}}$ are the linear velocities of the rotors at each joint, independent of the rotor angle β_j, $\dot{\boldsymbol{\theta}}^{\boldsymbol{r}} = [\dot{\theta}_1^r \quad \dot{\theta}_2^r \quad \dots \quad \dot{\theta}_{N-1}^r]^{\mathrm{T}}$, and $\mathcal{M}^r$ and $\mathcal{J}^r$ are $(N-1)$ by $(N-1)$ diagonal matrices of mass and moment of inertia of the rotors.

4.5 Derivation of the Potential Energy of the System

For lateral undulation in the horizontal plane performed by snake robots with stiff joints, the robot is not subject to any gravitational force [17]. However, in pedal wave motion the robot lifts its body part from the ground altering the gravitational potential energy. Moreover, due to the flexible elements attached between the robot links and the motors, additional terms also appear to capture the potential energy stored in the springs and this must be added to obtain the expression for the potential energy of the system.

Generally speaking, utilizing a high stiffness flexible element in the design of the robot actuator, it is possible to neglect the effect of the spring and model the robot with stiff joints [25]. However, the use of very stiff elements for SEAs, requires high-resolution encoders for measurement of the small deflections of the flexible element, losing the desirable features of SEAs and increasing the final cost of the prototype. Moreover, the effect of joint flexibility on the snake locomotion, due to using a passive compliant element or a SEA is still not fully investigated. For example, recently, in [104], a passive compliant element was added in series between the robot joints, and in [105] a soft bodied snake robot with passive compliance has been developed. However, both studies are based on experimentation and no mathematical justification is presented. This suggests that considering the effect of joint flexibility and therefore modelling the snake robot with flexible joint presents an interesting research opportunity.

4.5.1 Potential energy of the system due to the flexible elements at the joints

The first part of the potential energy of the snake robot as shown in Figure 4.1 is due to the springs attached between the actuators and links. Hence, the total potential energy of the system due to the torsional springs at the joints can be obtained as below:

$$V_1 = \frac{1}{2}(\boldsymbol{\beta} - \boldsymbol{\alpha})^{\mathrm{T}} K (\boldsymbol{\beta} - \boldsymbol{\alpha}), \tag{4.20}$$

where K is the $N-1$ by $N-1$ diagonal matrix containing stiffness of the flexible elements of the joints, $\boldsymbol{\alpha} = [\alpha_1, \dots, \alpha_{N-1}]^{\mathrm{T}}$ and $\boldsymbol{\beta} = [\beta_1, \dots, \beta_{N-1}]^{\mathrm{T}}$. This expression can also be represented as a function of generalized coordinates as follows:

$$V_1 = \frac{1}{2}\boldsymbol{q}^{\mathrm{T}} K_E \boldsymbol{q} \tag{4.21}$$

with K_E defined to be:

$$K_E = \begin{bmatrix} K_{(N-1)\times(N-1)} & 0_{(N-1)\times 3} & -K_{(N-1)\times(N-1)} \\ 0_{3\times(N-1)} & 0_{3\times(N-1)} & 0_{3\times(N-1)} \\ -K_{(N-1)\times(N-1)} & 0_{(N-1)\times 3} & K_{(N-1)\times(N-1)} \end{bmatrix} \tag{4.22}$$

where $0_{3\times(N-1)}$ and $0_{3\times 3}$ are null matrices with the specified dimensions.

4.5.2 Potential energy due to the gravity

Considering the body shape of the robot in the XZ plane, the robot lifts some parts of its body from the ground and push against the ground to move forward. Thus, the expression for the potential energy of the system due to the mass of the robot link and rotor should be obtained separately. Considering the body shape of the robot in Figure 4.1, the expression for the potential energy of the system due to the mass of the links (V_2) can be obtained as:

$$g(\boldsymbol{V^l})^{\mathrm{T}}\mathcal{M}^l\boldsymbol{Z^l} = \mathrm{g}(\boldsymbol{V^l})^{\mathrm{T}}\mathcal{M}^l\boldsymbol{V^l}z_0 + \mathcal{H}^l\boldsymbol{S\theta}. \tag{4.23}$$

Noting that that $p_z = 1/N\sum_{i=1}^{N} z_i^l$ and substituting z_0 from the expression of the centre of mass of the robot, (4.23) can be written as follows:

$$V_2{=}\mathrm{g}(\boldsymbol{V^l})^{\mathrm{T}}\mathcal{M}^l\boldsymbol{Z^l} = \mathrm{g}(\boldsymbol{V^l})^{\boldsymbol{T}}\mathcal{M}^l\left(\mathcal{B}_2^l - \mathcal{A}^l\mathcal{C}_\theta\mathcal{C}\right)\boldsymbol{q}. \tag{4.24}$$

Moreover, the centre of mass of the rotors are located at $\left[x_j^r, z_j^r\right]$ and not at the centre of mass of the links, thus similar procedure should be repeated to calculate the potential energy of the rotors due to its elevation, which will result in the following expression for the potential energy of the rotors:

$$V_3{=}\mathrm{g}(\boldsymbol{V^r})^{\mathrm{T}}\mathcal{M}^r\boldsymbol{Z}^r = \mathrm{g}(\boldsymbol{V^r})^{\mathrm{T}}\mathcal{M}^r(\mathcal{B}_2^r - \mathcal{A}^r\mathcal{C}_\theta\mathcal{C})\boldsymbol{q}. \tag{4.25}$$

4.6 Modelling the Contact Forces

Modelling the contact between the robot links and the environment is an essential part of modeling the pedal wave motion of the snake robot in vertical plane. To address this issue, some recent works, such as [106] and [69] have proposed a simplified contact model for such motion. However, in both of these methods, it is assumed that the number of contact points remains constant during the motion, and the normal forces are obtained based on the force and moment balance. Hence, such models are not suitable for modelling a snake robot with multiple contact points on surfaces with irregularities, where the robot might be in contact with several contact points in different planes.

To address this issue, one can use the well-known Kelvin–Voigt contact model [107]. Figure 4.3 shows the general case, where a single link of the robot is in contact with an

obstacle and f_k^N and f_k^T are the normal and tangential forces being exerted on the robot at the point of contact p_k by the environment.

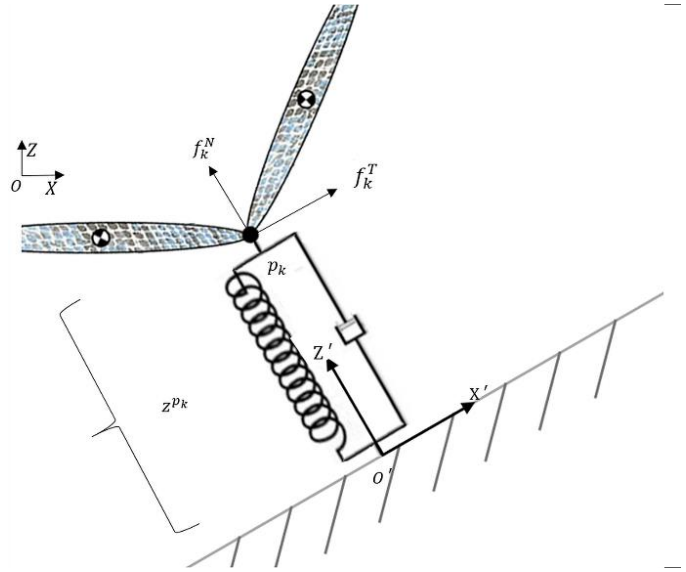

Figure 4.3 Kelvin–Voigt (spring-damper) contact model, shown the contact between the joint and the environment.

Assuming that p_k is in contact with the obstacle, i.e. $z^{p_k} \leq 0$, and considering a spring-damper contact model, f_k^N can be calculated as follows:

$$f_k^N = Max(\kappa z^{p_k} - d\dot{z}^{p_k}, 0) \tag{4.26}$$

where z^{p_k} is the coordinate of the point of contact p_k along Z'(z axis of the attached coordinate to the obstacle), κ is the spring and d is the damping constant of the environment. It should be noted that to calculate f_k^N, it is assumed that the contact forces, will always push the robot away from the contact surface, i.e. the robot link cannot be pulled towards the object. After obtaining f_k^N, it is straight forward to calculate f_k^T as follows:

$$f_k^T = -f_k^N \mu_C sign(\dot{x}^{p_k}) \tag{4.27}$$

where $\dot{x}^{p_k}$ is the velocity of point p_k along the direction tangent to the surface and μ_C is the friction coefficient between the robot link and the environment.

Having derived f_k^N and f_k^T for each contact point p_k, these forces should be incorporated into the equations of motion to calculate $\boldsymbol{Q}^c$ as follows:

$$\boldsymbol{Q}^c = \boldsymbol{Q}_1^c + \boldsymbol{Q}_2^c \tag{4.28}$$

where $\boldsymbol{Q}_1^c$ and $\boldsymbol{Q}_2^c$ are the vector of contact forces exerted at the center of the links and the joints (and the tip of the head and tail), respectively, which should be obtained separately as will be discussed, shortly.

If the point of contact p_k is located at the centre of mass of one of the links, it is enough to calculate the Jacobian matrix obtained in the previous section and calculate $\boldsymbol{Q}_1^c$ as follows:

$$\boldsymbol{Q}_1^c = \left[\frac{\partial \dot{\boldsymbol{X}}^{\boldsymbol{l}}}{\partial \dot{\boldsymbol{q}}} \;\middle|\; \frac{\partial \dot{\boldsymbol{Z}}^{\boldsymbol{l}}}{\partial \dot{\boldsymbol{q}}}\right]\left[\frac{\boldsymbol{F}_{\boldsymbol{1}}^{\boldsymbol{x}}}{\boldsymbol{F}_{\boldsymbol{1}}^{\boldsymbol{z}}}\right], \tag{4.29}$$

where $\frac{\partial \dot{\boldsymbol{X}}^{\boldsymbol{l}}}{\partial \dot{\boldsymbol{q}}} = \left[\left(\mathcal{B}_1^l + \mathcal{A}^l \mathcal{S}_\theta \mathcal{C}\right) \quad \mathcal{O}_l\right]^{\mathrm{T}}$, $\frac{\partial \dot{\boldsymbol{Z}}^{\boldsymbol{l}}}{\partial \dot{\boldsymbol{q}}} = \left[\left(\mathcal{B}_2^l - \mathcal{A}^l \mathcal{C}_\theta \mathcal{C}\right) \quad \mathcal{O}_l\right]^{\mathrm{T}}$ and $\boldsymbol{F}_{\boldsymbol{1}}^{\boldsymbol{x}} = [f_1^x \quad f_2^x \quad \dots \quad f_N^x]^{\mathrm{T}}$, $\boldsymbol{F}_{\boldsymbol{1}}^{\boldsymbol{z}} = [f_1^z \quad f_2^z \quad \dots \quad f_N^z]^{\mathrm{T}}$ are the vectors of all non-conservative forces along the global *X* and *Z* direction, respectively.

On the other hand, to obtain a more realistic simulation model of the snake robot, one should also consider the effect of contact forces on the robot joints, tip of the head and the tail to calculate $\boldsymbol{Q}_2^c$. This means that for a snake robot with N links and $N-1$ joints, $2N+1$ points on the robot should be tested at each time-step to see if a contact has occurred or not. Once the set of contact points, i.e. $p_k; k = 1, \dots, K$ have been obtained, the tangential and normal forces at these points can be calculated based on (4.26) and (4.27). If the contact

point is located on the centre of mass of the link, one can use (4.29), otherwise the expression (4.30) can be employed:

$$\boldsymbol{Q}_2^c = \left[\frac{\partial \dot{\boldsymbol{X}}^0}{\partial \dot{\boldsymbol{q}}} \quad \middle| \quad \frac{\partial \dot{\boldsymbol{Z}}^0}{\partial \dot{\boldsymbol{q}}}\right]\left[\frac{\boldsymbol{F}_2^x}{\boldsymbol{F}_2^z}\right], \tag{4.30}$$

where $\boldsymbol{F}_2^x = [f_1^x \quad f_2^x \quad \dots \quad f_{N+1}^x]^{\mathrm{T}}$, $\boldsymbol{F}_2^z = [f_1^z \quad f_2^z \quad \dots \quad f_{N+1}^z]^{\mathrm{T}}$, $\dot{\boldsymbol{X}}^0$ and $\dot{\boldsymbol{Z}}^0$ are the velocity vectors of the possible point of contacts, which can be obtained as follows:

$$\dot{\boldsymbol{X}}^0 = \left[(\mathcal{B}_1^0 + \mathcal{A}^0 \mathcal{S}_\theta \mathcal{C}) \quad \mathcal{O}_{(N+1)\times(N-1)}\right]\dot{\boldsymbol{q}}, \tag{4.31}$$

$$\dot{\boldsymbol{Z}}^0 = \left[(\mathcal{B}_2^0 - \mathcal{A}^0 \mathcal{C}_\theta \mathcal{C}) \quad \mathcal{O}_{(N+1)\times(N-1)}\right]\dot{\boldsymbol{q}}, \tag{4.32}$$

where $\mathcal{B}_1^0 = \left[0_{(N+1)\times N} \quad \boldsymbol{V}^0 \quad 0_{(N+1)\times 1}\right]$, $\mathcal{B}_2^0 = \left[0_{(N+1)\times(N+1)} \quad \boldsymbol{V}^0\right]$, $\mathcal{A}^0 = -\mathcal{H}^0 + \frac{1}{N}\boldsymbol{V}^0\left(\boldsymbol{V}^l\right)^{\mathrm{T}}\mathcal{H}^l$, $\boldsymbol{V}^0 = [1 \quad 1 \quad \dots \quad 1]^{\mathrm{T}}_{(N+1)\times 1}$, $\mathcal{C} = [\mathcal{F} \quad \boldsymbol{V}^l \quad 0_{N\times 2}]$, $0_{N\times N}$ is an N by N matrix with all zero elements and $\mathcal{H}^0 = \left[\frac{\mathbf{0}_{1\times(N+1)}}{\mathcal{H}^r}\right]$.

In the general case shown in Figure 4.3, f_k^N and f_k^T are expressed in the stationary coordinate frame $OX'Z'$, which is not necessarily aligned with the global coordinate frame. Thus, these forces should be expressed in the global coordinate frame to construct $\left[\frac{\boldsymbol{F}_1^x}{\boldsymbol{F}_1^z}\right]$ and $\left[\frac{\boldsymbol{F}_2^x}{\boldsymbol{F}_2^z}\right]$, then equations (4.29) and (4.30) can be used to incorporate these forces into the dynamical model. Moreover, it is worthwhile to emphasize that the components of vectors $\left[\frac{\boldsymbol{F}_1^x}{\boldsymbol{F}_1^z}\right]$ and $\left[\frac{\boldsymbol{F}_2^x}{\boldsymbol{F}_2^z}\right]$ will be calculated using the contact model in (4.26) and (4.27). Hence, if there is no contact between the centre of mass of link i or the robot joints and the

environment, the corresponding component will become zero, without having any effect on the dynamical equations.

Another advantage of this flexible contact model is that it allows to simulate the motion of the robot in environments with irregularities. A spring and a damper can be attached to any surfaces that the robot might contact with. After detecting the contact, the external forces normal and parallel to that surface can be calculated using the presented method. For example, to model a stair-type obstacle, it is enough to attach a spring-damper to the sides and top of the obstacle as shown in Figure 4.4. Hence, in addition to the contact forces from the ground, the contact forces due to collision with the obstacle can also be incorporated into the model.

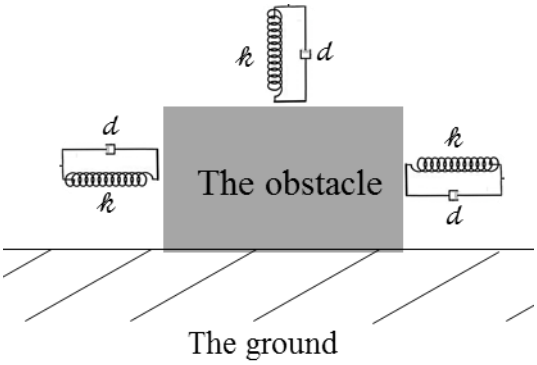

Figure 4.4 Kelvin–Voigt (Spring-damper) model, attached to the sides and top of an obstacle located on the ground for modelling the contact forces.

4.7 Equations of Motion of the Snake Robot with SEAs in the Vertical Plane

Obtaining the expression for the kinetic and potential energy of the system and the contact forces, the next step towards obtaining the final equations of motion of the robot is the calculation of the gradient of the kinetic energy of the system with respect to $\boldsymbol{q}$ and $\dot{\boldsymbol{q}}$. Considering the introduced matrix notation, this is a straight forward procedure. For

example, considering the expression for the kinetic energy of the links (T_1) in (4.18), one can calculate $\frac{d}{dt}\left(\frac{\partial T_1}{\partial \dot{\boldsymbol{q}}}\right)$ as follows:

$$\frac{d}{dt}\left(\frac{\partial T_1}{\partial \dot{\boldsymbol{q}}}\right) = \frac{d}{dt}\left(\frac{1}{2}\frac{\partial \left(\dot{\boldsymbol{X}}^l\right)^{\mathrm{T}} \mathcal{M}^l \left(\dot{\boldsymbol{X}}^l\right)}{\partial \dot{\boldsymbol{q}}} + \frac{1}{2}\frac{\partial \left(\dot{\boldsymbol{Z}}^l\right)^{\mathrm{T}} \mathcal{M}^l \left(\dot{\boldsymbol{Z}}^l\right)}{\partial \dot{\boldsymbol{q}}} + \frac{1}{2}\frac{\partial \left(\dot{\boldsymbol{\theta}}^l\right)^{\mathrm{T}} \mathcal{J}^l \left(\dot{\boldsymbol{\theta}}^l\right)}{\partial \dot{\boldsymbol{q}}}\right). \tag{4.33}$$

Replacing $\dot{\boldsymbol{X}}^l$, $\dot{\boldsymbol{Z}}^l$ and $\dot{\boldsymbol{\theta}}^l$ from (4.15)-(4.17), equation (4.33) can be written as a function of $\boldsymbol{q}$ and $\dot{\boldsymbol{q}}$. Thus, knowing that the kinetic energy of each link is independent of the relative rotor angles $\boldsymbol{q}_2 = [\beta_1, \dots, \beta_{N-1}]^{\mathrm{T}}$, (4.33) can be calculated to be as follows:

$$\begin{aligned}
\frac{d}{dt}\left(\frac{\partial T_1}{\partial \dot{\boldsymbol{q}}_1}\right) = \Big[& \left(\mathcal{B}_1^l + \mathcal{A}^l \mathcal{S}_\theta \mathcal{C}\right)^{\mathrm{T}} \mathcal{M}^l \left(\mathcal{B}_1^l + \mathcal{A}^l \mathcal{S}_\theta \mathcal{C}\right) \\
& + \left(\mathcal{B}_2^l - \mathcal{A}^l \mathcal{C}_\theta \mathcal{C}\right)^{\mathrm{T}} \mathcal{M}^l \left(\mathcal{B}_2^l - \mathcal{A}^l \mathcal{C}_\theta \mathcal{C}\right) + \mathcal{C}^{\mathrm{T}} \mathcal{J}^l \mathcal{C} \Big] \ddot{\boldsymbol{q}}_{\boldsymbol{1}} \\
& + \Big[{\mathcal{B}_1^l}^{\mathrm{T}} \mathcal{M}^l \mathcal{A}^l \mathcal{C}_\theta diag\left(\dot{\boldsymbol{\theta}}^l\right) \mathcal{C} + \mathcal{C}^{\mathrm{T}} \mathcal{C}_\theta diag\left(\dot{\boldsymbol{\theta}}^l\right) {\mathcal{A}^l}^{\mathrm{T}} \mathcal{M}^l \mathcal{B}_1^l \\
& + \mathcal{C}^{\mathrm{T}} \mathcal{S}_\theta {\mathcal{A}^l}^{\mathrm{T}} \mathcal{M}^l \mathcal{A}^l \mathcal{C}_\theta diag\left(\dot{\boldsymbol{\theta}}^l\right) \mathcal{C} + \mathcal{C}^{\mathrm{T}} \mathcal{C}_\theta diag\left(\dot{\boldsymbol{\theta}}^l\right) {\mathcal{A}^l}^{\mathrm{T}} \mathcal{M}^l \mathcal{A}^l \mathcal{S}_\theta \mathcal{C} \\
& + {\mathcal{B}_2^l}^{\mathrm{T}} \mathcal{M}^l \mathcal{A}^l \mathcal{S}_\theta diag\left(\dot{\boldsymbol{\theta}}^l\right) \mathcal{C} + \mathcal{C}^{\mathrm{T}} \mathcal{S}_\theta diag\left(\dot{\boldsymbol{\theta}}^l\right) {\mathcal{A}^l}^{\mathrm{T}} \mathcal{M}^l \mathcal{B}_2^l \\
& - \mathcal{C}^{\mathrm{T}} \mathcal{C}_\theta {\mathcal{A}^l}^{\mathrm{T}} \mathcal{M}^l \mathcal{A}^l \mathcal{S}_\theta diag\left(\dot{\boldsymbol{\theta}}^l\right) \mathcal{C} \\
& - \mathcal{C}^{\mathrm{T}} \mathcal{S}_\theta diag\left(\dot{\boldsymbol{\theta}}^l\right) {\mathcal{A}^l}^{\mathrm{T}} \mathcal{M}^l \mathcal{A}^l \mathcal{C}_\theta \mathcal{C} \Big] \dot{\boldsymbol{q}}_{\boldsymbol{1}}
\end{aligned} \tag{4.34}$$

where $\boldsymbol{q}_{\boldsymbol{1}}$ is the first $N+2$ elements of the state vector $\boldsymbol{q}$, i.e. $\boldsymbol{q}_1 = \left[\alpha_1, \dots, \alpha_{N-1}, \theta_N^l, p_x, p_z\right]^{\mathrm{T}}$.

Considering the Lagrange-Euler equations of motion in (4.1), and the kinetic and potential energy of the system introduced in a matrix notation, other terms of the dynamical equations of the system can be obtained. Thus, the equations of motion of a flexible joint modular snake robot with N links ($N-1$ joints) can be obtained as follows:

$$\begin{bmatrix} \mathbb{M}(\boldsymbol{q_1}) + \mathbb{S}_1 & \mathbb{S}_2 \\ \mathbb{S}_2^{\mathrm{T}} & \mathbb{S}_3 \end{bmatrix} \ddot{\boldsymbol{q}} + \begin{bmatrix} \mathbb{C}(\boldsymbol{q_1}, \dot{\boldsymbol{q}}_1) \\ \boldsymbol{0} \end{bmatrix} + \boldsymbol{\mathcal{G}} + K_E \boldsymbol{q} - \boldsymbol{Q}^c = \mathbb{B} \tag{4.35}$$

where $\mathbb{M}(\boldsymbol{q_1})_{(N+2)\times(N+2)}$ is a positive definite inertia matrix, $\mathbb{C}(\boldsymbol{q_1}, \dot{\boldsymbol{q}}_1)_{(N+2)}$ is the vector of Coriolis and centrifugal terms, $\boldsymbol{\mathcal{G}}$ is a column vector of gravitational forces, $\mathbb{B} = \begin{bmatrix} \boldsymbol{0}_{1\times(N+2)} & | & \boldsymbol{U}^{\mathrm{T}} \end{bmatrix}^{\mathrm{T}}$, $\boldsymbol{U}$ is the column vector of $N-1$ control inputs (motor torques), $\boldsymbol{Q}^c$ is the vector of non-conservative contact forces and

$$\begin{bmatrix} \mathbb{S}_1 & \mathbb{S}_2 \\ \mathbb{S}_2^{\mathrm{T}} & \mathbb{S}_3 \end{bmatrix} = \mathcal{L}^T \mathcal{J}^r \mathcal{L}$$

where $\mathcal{L}$ is defined in (4.17), $\mathbb{S}_1$ and $\mathbb{S}_2$ are appeared due to the angular velocity of the rotors depending on $\dot{\boldsymbol{\theta}}^l$, and $\mathbb{S}_3$ depends on the inertia and gear ratio of the rotors. (See Appendix A giving the structure of the matrices in (4.35)).

Equations of motions of the snake robot as presented in (4.35) can be seen as two sets of equations. The first $N+2$ equations are under-actuated dynamics of the system containing relative joint angles, position of the centre of mass and the orientation of the robots head module, in which the friction forces and other environmental forces will appear and the last $N-1$ equations are fully actuated motor-side equations. Generally speaking, in serial robots with large gear ratio one can assume that the angular velocity of the rotor is only due to its own angular velocity before the gear box [108]. Hence, to better analyse the equations of motion of the robot, it is worthwhile to replace $\dot{\boldsymbol{\theta}}^{\boldsymbol{r}}$ with $\dot{\boldsymbol{\beta}}$ in (4.19) and rewrite the equations of motion of the snake robot in the vertical plane as two coupled equations as follows:

$$\begin{aligned} \mathbb{M}(\boldsymbol{q_1})\ddot{\boldsymbol{q}}_1 + \mathbb{C}(\boldsymbol{q_1}, \dot{\boldsymbol{q}}_1) + \boldsymbol{\mathcal{G}}' - \boldsymbol{Q}^{c\prime} &= \begin{bmatrix} \tau_J \\ 0_{3\times 1} \end{bmatrix} \\ \mathbb{S}_3 \ddot{\boldsymbol{\beta}} + \tau_J &= \boldsymbol{U} \end{aligned} \tag{4.36}$$

where $\boldsymbol{\mathcal{G}}'$and $\boldsymbol{Q}^{c\prime}$ are the first $N+2$ components of $\boldsymbol{\mathcal{G}}$ and $\boldsymbol{Q}^{c}$, respectively and $\tau_J = K(\boldsymbol{\alpha}-\boldsymbol{\beta})$.

As it can be seen from the separated equations in (4.36), the first $N+2$ equations are coupled with the last $N-1$ ones only through the spring torque τ_J. Moreover, one can see that, if the stiffness matrix K has large elements (a snake robot with stiff joints), $\boldsymbol{\alpha} \to \boldsymbol{\beta}$ and eventually $\tau_J \to \boldsymbol{U}$. This shows that, one can use the measured spring deflection to get an estimate of the output torque of a position controlled servo motor. Additionally, considering the snake robot with stiff joints the equations of motion of the snake robot in vertical plane can easily be obtained from (4.36) by ignoring the last $N-1$ equations as follows:

$$(\mathbb{M}(\boldsymbol{q_1}) + \mathbb{S}_3)\ddot{\boldsymbol{q}}_{\boldsymbol{1}} + \mathbb{C}(\boldsymbol{q_1}, \dot{\boldsymbol{q}}_{\boldsymbol{1}}) + \boldsymbol{\mathcal{G}}' - \boldsymbol{Q}^{c\prime} = \boldsymbol{U}, \tag{4.37}$$

which can be used to model any snake-like motion in vertical plane.

This dynamical model provides the opportunities to:

- Understand the fundamentals of biological snake locomotion patterns and identify the key contributing factors in such motions.
- Investigate the effect of varying environmental conditions, such as friction on the robot motion.
- Examine the effect of physical robot design parameters, such as weight of the modules and length of the links on the robot motion.
- Employ model-based motion optimization methods to achieve more agile locomotion patterns while minimizing the energy consumption.

4.8 Position Control Design for Snake Robots with SEAs

To achieve simulated pedal wave motion, the dynamical model (4.35) should be accompanied by a position controller at each joint. Considering the control structure in Figure 3.1, the first step towards generating such motion is to design the Mid-level controller. For this purpose, one can generate joint position references using the following gait pattern [14]:

$$\alpha_j^d = A\,sin\big(\omega t + \phi(j-1)\big) \tag{4.38}$$

where $\alpha_j^d; j = 1,2,\dots,N-1$ are the desired joint angles, ω is the temporal frequency, ϕ is the spatial frequency (phase shift) and A is the amplitude of the sinusoidal wave. By controlling the parameters of such gait equation, which unlike the parameters of CPG based oscillators like [88], have more physical meaning, one can change the body shape of the robot to achieve the desired motion. For example, one can intuitively increase the spatial frequency ϕ to increase the number of waves along the body of the snake.

To design the Lower-level controller for the snake robot, as the second step towards generating the pedal wave motion, a control scheme should be devised such that the error between the desired joint angle (α_j^d) and the measured relative joint angles (α_j) becomes as small as possible during the motion by only using the servo motor angular position (β_j) and velocity ($\dot{\beta}_j$) feedback, which are easily available for measurement. Generally speaking, due to the flexibility of the robot joint, designing such a tracking controller for flexible joint manipulators requires using back stepping control techniques [25]. However, in a snake-like motion, $\ddot{\alpha}_j^d$ and $\dddot{\alpha}_j^d$ (joint acceleration and jerk) are sufficiently small due to the upper limits on A, ω imposed by the mechanical limitation of the designs. Hence, motivated by the controller proposed in [109] for trajectory tracking of manipulators with flexible joints, we

propose the following Proportional-Derivative (PD) controller (C_p) to track the desired joint angles generated by (4.38):

$$\boldsymbol{U} = -K_p\left(\beta_j - \alpha_j^d\right) - K_D\left(\dot{\beta}_j - \dot{\alpha}_j^d\right), \tag{4.39}$$

where K_p and K_D are positive gains to be chosen and $\boldsymbol{U}$ is the control input to the motors as appeared in dynamical model (4.35). Figure 4.5 better shows the block diagram of the proposed controller designed for each robot joint.

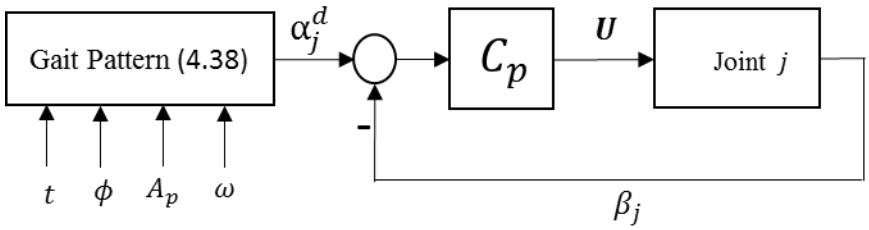

Figure 4.5. The block diagram of the joint level position controller.

Controller (4.39) with carefully tuned control gains guarantees that β_j will converge to α_j^d due to the stability of the system, and other variables θ_N^l, p_x, p_z remain to be only constrained by dynamics (4.35). In other words, (4.39) is used to only control the relative joint angles and other under-actuated degrees of freedom of the system, i.e., θ_N^l, p_x, p_z remain to be uncontrolled. Moreover, it should be noted that considering the potential energy of the system due to the gravity as presented in (4.40),

$$V_2 + V_3 = m^l g \sum_i^N z_i^l + m^r g \sum_i^N z_i^r\,, \tag{4.40}$$

one can argue that m^r is relatively small compared to m^l. Hence, the total potential energy of the system due to gravity can be approximated to be:

$$V_2 = m^l g \sum_{i=1}^{N} z_i^l = N m^l g p_z, \tag{4.41}$$

which is only a function of p_z. This means that the gravity terms only appear in the $(N+2)^{th}$row of the equations of motion and other components of $\boldsymbol{\mathcal{G}}$ are zero. Because of this the effect of gravity only appears in the equations of motion of the uncontrolled degree of freedom p_z and not the joint angles, hence no gravity compensation term has been added to the controller (4.39). This is an important result because unlike manipulators with fixed base, in snake robots, z_i^ls and θ_N^l cannot be uniquely determined by the joint angles. Hence, without a need for additional sensory feedback, like Inertial Measurement Units (IMUs), controller (4.39) makes it possible to easily generate pedal wave motion by only using easily accessible motor side measurements.

4.9 Summary

In this chapter, a novel generalized modelling framework for modelling locomotion of modular snake robots with SEAs in the vertical plane was presented. The potential and kinetic energy of the system were calculated using a novel matrix notation and equations of motion of the robot using Euler-Lagrange method obtained. Utilizing a spring-damper (Kelvin–Voigt) contact model the contact forces between the robot and the environment were modelled and incorporated into the equations of motion to obtain dynamical model of the snake robot locomotion in the vertical plane allowing to simulate the snake motion with SEA on surfaces with irregularities for the first time. The final structure of the model was presented and a position control for the robot joints was also designed to help tracking the desired joint trajectory generated by a parametrized gait pattern.

5

PEDAL WAVE LOCOMOTION ON SMOOTH SURFACES: EXPERIMENTAL AND SIMULATION RESULTS

5.1 Introduction

The design process and modeling framework presented in the previous chapters facilitate achieving the ultimate goal of this thesis, which is effective snake-like pedal wave motion on surfaces with irregularities. However, it is still critical to analyze such motion on smooth surfaces by conducting experimentation on the physical and simulated snake robot. This will help us to examine the effectiveness of the proposed snake robot design, investigate the reliability of the simulation model, and identify key characteristics of pedal wave motion.

To achieve these goals, the position controller in (4.39) is implemented on the physical snake robot to show the effectiveness of the robot design and further investigate the fundamentals of the pedal wave motion. Additionally, the equations of motions in (4.35) is used to simulate pedal wave motion on smooth surfaces and the validity of the model is examined by comparing the torque signal measured by the elastic element with the one obtained from the simulation. Moreover, the effect of varying gait parameters on the robot motion is examined and the effect of friction on the forward speed of the robot is investigated to identify contributing factors in pedal wave locomotion on smooth surfaces performed by the designed and simulated snake robot with SEAs.

5.2 Pedal Wave Motion on Smooth Surfaces Performed by the Snake Robot

Employing the proposed controller shown in Figure 4.5, the body shape of the snake robot designed in Chapter 3 can be controlled and consequently pedal wave motion with the physical snake robot can be achieved using gait pattern (4.38). To experimentally support this claim, the gait parameters of (4.38) were chosen to be $A = \frac{\pi}{6}\ rad$, $\omega = \pi\ rad.s^{-1}$ and $\phi = \frac{-2\pi}{5}\ rad$ and the master controller programmed to send these parameters, i.e. A, ω and ϕ to the local microcontrollers at each joint using the CAN bus communication system. Figure 5.1 shows the snake robot performing pedal wave motion on a smooth surface. In this experiment ϕ was chosen to be equal to $\frac{-2\pi}{N-1}$ to make sure the snake body shape covers one full wave at each step-time and two contact points are established while the robot is in motion. Moreover, the input voltage was chosen to be $9.4\,V$, which is higher than the

nominal voltage of the servo motor to compensate for the possible voltage drop due to transmission.

The experiment, as demonstrated in Figure 5.1, showed that although a flexible element is attached between the motor and the joints, the robot could generate pedal wave motion on smooth surfaces and move forward with the use of controller (4.39) with the forward speed of $2.8\ cm.s^{-1}$. Moreover, this experiment showed the potential of pedal wave locomotion mechanism for moving on surfaces with irregularities because as shown in Figure 5.1, during the motion, the robot lifts its body part and pushes against the ground to move forward, which is a desirable behaviour and can potentially be used for locomotion on surfaces with irregularities (See Appendix C, Supplementary Material C.1).

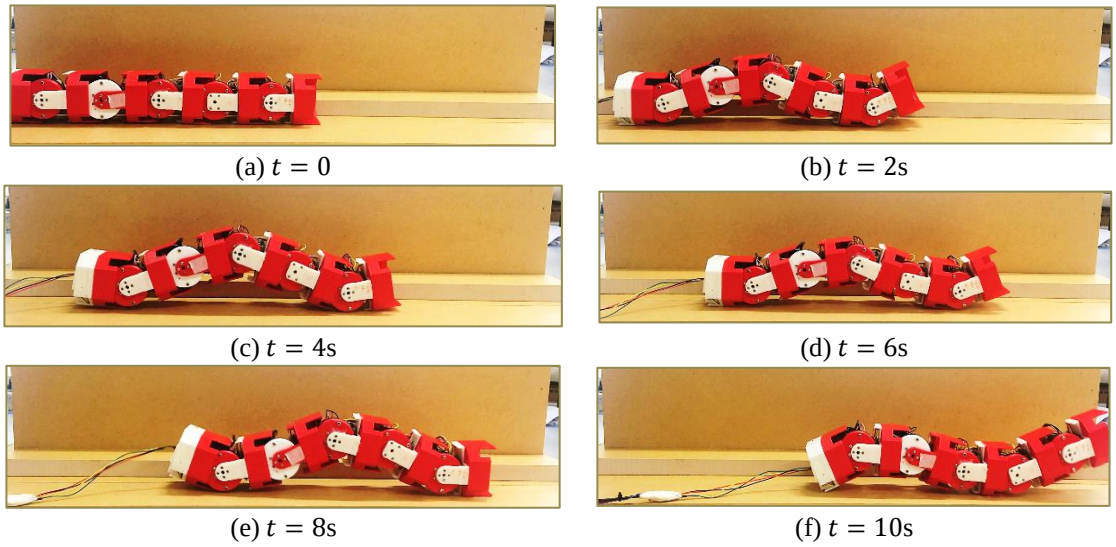

(a) $t = 0$ (b) $t = 2$s

(c) $t = 4$s (d) $t = 6$s

(e) $t = 8$s (f) $t = 10$s

Figure 5.1. Snake robot progression with pedal wave motion with $A = \frac{\pi}{6} rad$, $\omega = \pi\ rad.s^{-1}$ and $\phi = \frac{-2\pi}{5}\ rad$ and average speed of $2.8\ cm.s^{-1}$.

To better investigate the performance of the robot while performing pedal wave motion, Figure 5.2 is given, shows the error between the relative link angles, i.e. α_js, and the commanded relative link angles generated by gait pattern (4.38). As it can be seen in

Figure 5.2, controller (4.39) has been used to track the commanded relative links angles, when the maximum error was 18%, due to the flexible element at the joint and the employed position controller. When there is a contact between the links and the ground, due to the physical obstacle, the robot joint cannot reach to its commanded position. Hence, although the error signals seem to follow similar patterns, this error cannot be compensated. This means that the error between the commanded and measured joint angle increases during the contact and as the third joint is closer to the centre of mass of the robot the position error of the middle joint is the highest. This might not be a desired behaviour, when accurate position control is required, (such as a manipulation task with a robotic arm equipped with SEA, see [110] for more details). However, the most important factor in snake-like locomotion is the interaction between the robot and the environment. Hence, it is worthwhile to still use the position control with motor side measurements and estimate the external contact force by measuring the deflection of the elastic element. In the next chapter, we will show that such torque feedback signal obtained by measuring the deflection of the elastic element can be used for effective pedal wave motion generation on surfaces with irregularities.

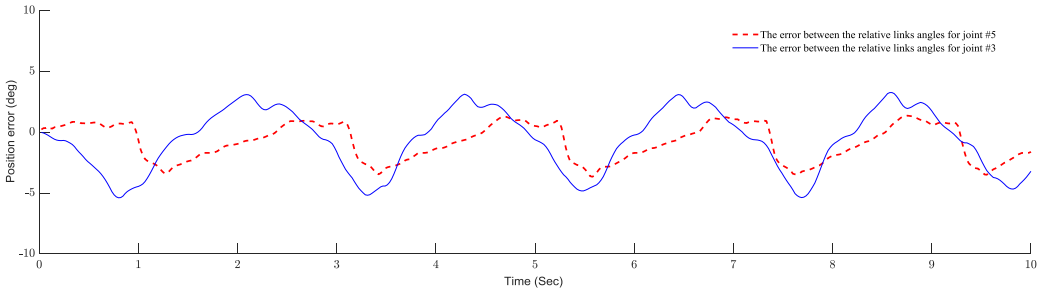

Figure 5.2. Performance of the position controller (4.39) while performing pedal wave motion with $A = \frac{\pi}{6} rad$, $\omega = \pi\, rad.s^{-1}$ and $\phi = \frac{-2\pi}{5}\, rad$.

To estimate the torque feedback signal, an elastic element with higher stiffness and a magnetic encoder with higher resolution could be used. However, using an elastic element with lower stiffness can better protect the servo-motors from excessive external forces due

to the repetitive contact with the environment. Moreover, although such compliance can affect the performance of the controller, it provides intrinsic adaptability due to the joint capability to flex, which can be advantageous in unstructured environments.

5.3 Simulated Snake Robot Pedal Wave Motion on Smooth Surfaces

To show the accuracy of the equations of motion presented in (4.35) and examine the reliability of such model to capture the fundamentals of pedal wave motion, the equations of motion (4.35) were implemented in MATLAB (2017, The Mathworks). Controller (4.39) then employed as the joint controller to track gait equation (4.38), where the gait parameters were selected to be the same as the experiment shown in Figure 5.1, i.e., $A = \frac{\pi}{6}\ rad,\ \omega = \pi\ rad.s^{-1}$ and $\phi = \frac{-2\pi}{5}\ rad.$ Figure 5.3 shows the pedal wave motion, with the simulation parameters given in Table 5.1. (See Appendix C, Supplementary Material C.1).

As it can be seen in Figure 5.3 the model has been successfully used to simulate the pedal wave motion of the modular snake robot with SEAs moving on a smooth surface with the same physical parameters of the real snake robot, which unlike existing works, such as [69] is the only model that takes into account the joint flexibility. An important consideration is that, the simulation step time is chosen to be sufficiently small to make sure the fast dynamics of the system, i.e., last $N-1$ rows of (4.35) are being captured. Moreover, one should note that using a spring damper contact model, the link should penetrate the object to calculate the contact forces. Hence, to make sure that during the simulation of the pedal wave motion on the ground, the potential energy will not become negative, it is assumed that the links will come into contact with the ground when $z^{p_k} \leq 0.01m.$

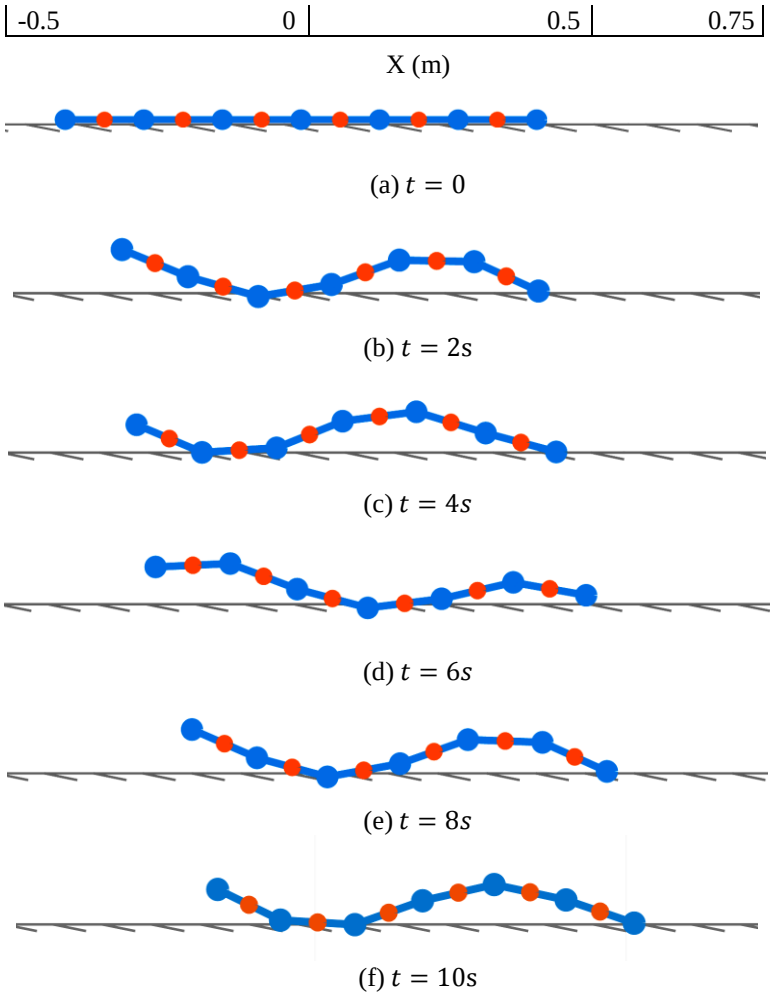

Figure 5.3. The simulated snake robot pedal wave motion with $A = \frac{\pi}{6} rad$, $\omega = \pi\ rad.s^{-1}$ and $\phi = \frac{-2\pi}{5} rad$, where the large blue circles denote the joints, tip of the head and the tail module and the small red circles denote the centre of mass of the links.

Table 5.1 Simulation parameters

Sampling time	$0.0001s$
PD tracking controller gains	$K_p = 60\ N.m.rad^{-1}$ $K_D = 25\ N.m.s.rad^{-1}$
Spring-damper contact model parameters	$\mu_C = 0.6$ $k = 550\ N.m^{-1}$ $d = 10\ N.s.m^{-1}$
Parameters of the robot	$m_r = 0.02\ kg$ $m_l = 0.15\ kg$ $J_l = 1.52\ e^{-5}\ kg.m^2$ $J_r = 2.45e^{-7}\ kg.m^2$

Considering the simulation results, one can comment on the validity of the obtained equations of motion, by comparing the measured torque signal by the one obtained from the simulation model as this captures the dynamic interaction between the robot and the environment that results in motion. For this purpose, the torque signal obtained by measuring the deflection of the elastic element of joint 2, joint 3 and joint 5 of the robot recorded and as shown in Figure 5.4 have been compared with the torque signal obtained from the simulation.

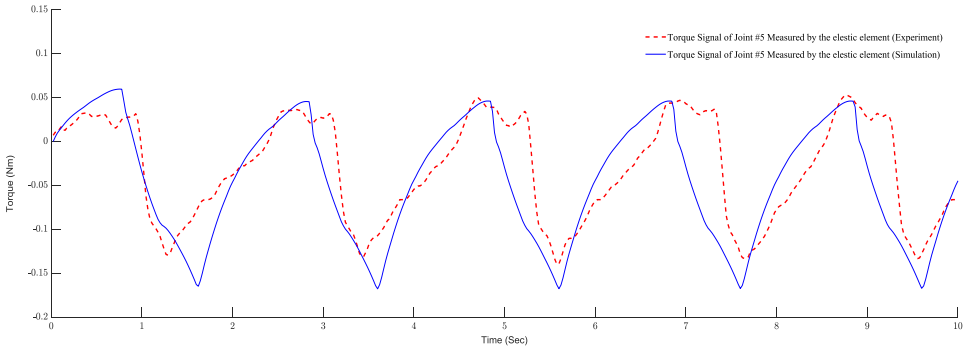

(a) Head module (joint 5), measured and simulated torque signal.

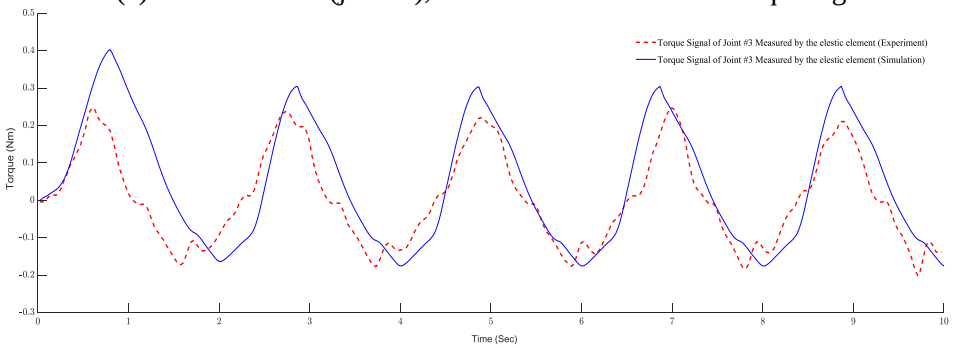

(b) Middle body module (joint 3), measured and simulated torque signal.

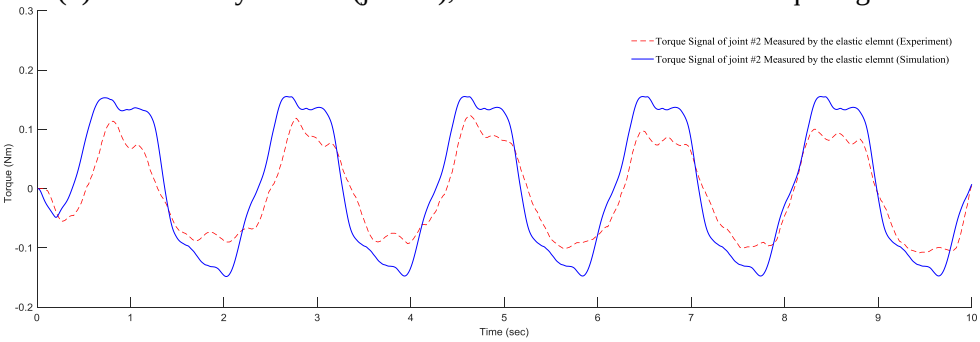

(c) Joint 2, measured and simulated torque signal.

Figure 5.4. Comparison of the torque signal measured by the elastic element from the simulation and experimentation with the physical robot with $A = \frac{\pi}{6} rad$, $\omega = \pi\ rad.s^{-1}$ and $\phi = \frac{-2\pi}{5}\ rad$.

As can be seen in Figure 5.4, the experimental data closely resembles the simulation data with some expected error. To better quantify the error between the simulation and experimentation results, Figure 5.5 is provided showing the torque signal of all joints obtained from the simulation and experiment plotted together, where the best linear fit is shown and the correlation coefficient R (see Appendix B) indicating the similarity between the signals is calculated to be 0.8336. As it can be seen in Figure 5.5, there is some error due to the complexity of the modelling and the required assumptions. The differences between the model and the actual robot primarily stem from the difficulty in accurate modelling of the contact forces. Other reasons potentially responsible for the inaccuracy of the simulation model are the uneven distribution of the mass within the links, varying characteristics of the elastic element due to change in the room temperature and the assumed uniform friction property of the surface.

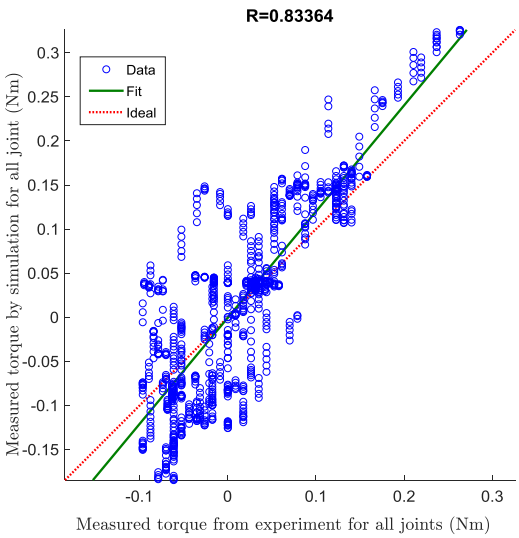

Figure 5.5. The regression result, showing the measured torque data of every robot joint during one period obtained from the simulation and experimentation.

Although there exist some expected discrepancy between the model and the robot, it can be seen from Figure 5.4, that in both the simulation and experimentation with the

physical robot, joint 3, which is closer to the centre of mass of the robot should generate more output torque relative to joint 5 and joint 2, which are far from the centre of mass of the robot. This result, which is also mentioned in [83], shows that despite some expected differences, the simulation model has successfully predicted the behaviour of the robot performing pedal wave motion.

Another important result is that the motor output toque can be approximated by the torque signal measured by the elastic element as discussed in Section 4.7. Figure 5.6, shows these two quantities plotted together for every joint of the simulated snake robot performing pedal wave motion, where correlation coefficient R is calculated to be 0.9972.

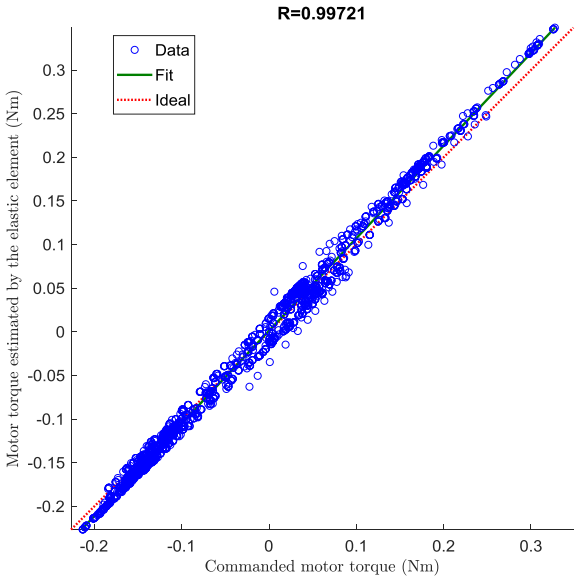

Figure 5.6. Comparison between the measured torque signal by the elastic element of each module with the commanded motor output torque for simulated pedal wave motion with $A = \frac{\pi}{6}\ rad$, $\omega = \pi\ rad.s^{-1}$ and $\phi = \frac{-2\pi}{5}\ rad$.

As can be seen in Figure 5.6, the motor torque and the torque signal measured with the elastic element have a great degree of similarity as expected from model (4.35). This is

very important and will be used in the next chapter for designing the pedal wave motion controller based on motor torque feedback.

5.4 The Effect of Gait Parameters on the Average Speed of Pedal Wave Motion

To further examine the validity of the simulation model, it is critical to compare the average speed of the robot obtained from the simulation and experimentation with the physical robot as a result of varying the gait parameters. The result of this experiment is shown in Table 5.2, where the average speed of the robot is calculated by measuring the distance the robot has travelled in 10 seconds. It should be noted that in the experiment, ω was selected to be constant and equal to $\pi\ rad.s^{-1}$. The reason for constant ω is that the body shape of the robot can be determined by knowing the amplitude and the spatial frequency of the gait pattern and increasing the frequency of the wave clearly makes the robot move faster, without changing the body shape of the robot.

From Table 5.2, one can see that the speed of the robot predicted by the simulation model is close to the experimentation results with some expected error, where the highest error (38.7%) is for the case with $A = \frac{\pi}{6}, \phi = \frac{-2\pi+0.4}{5}$, the lowest error (4%) obtained when $A = \frac{\pi}{3}, \phi = \frac{-2\pi-0.4}{5}$ and the average error obtained to be 22.2%.

Four major factors are mainly responsible for such error. The most important reason for the discrepancy between the average speed obtained from the simulation and experimental result is that due to the computation limitation, only certain points on the robot (i.e. the joints, the tip of the head and tail module) can be checked at each step time for the

possible contact with the ground. The second factor is the effect of the mass of the cable connecting the snake to the power supply, which even in some cases observed to have an effect on the direction of the motion. The third factor is slipping between the robot links and the ground, which has considerable effect on the forward speed of the robot, which can be minimized by decreasing the speed or increasing the frictional characteristics of the robot. The final reason is that the average velocity is obtained when the robot moving forward for ten seconds. This means the error between the simulation and the physical robot will be accumulated, which results in a relatively poor prediction of average robot speed compared to the motor torque measurement comparison results.

Table 5.2 The average speed of the robot ($cm.s^{-1}$)
obtained from the simulation (S) and experimentation (E)
by varying gait parameters A and ϕ.

	Amplitude					
	$A=\frac{\pi}{6}$		$A=\frac{\pi}{4}$		$A=\frac{\pi}{3}$	
Phase shift	S	E	S	E	S	E
$\phi=\frac{-2\pi-0.4}{5}$	1.9	3.1	2.9	4.1	5.9	6.2
$\phi=\frac{-2\pi}{5}$	1.8	2.8	3.3	4.7	4.9	5.8
$\phi=\frac{-2\pi+0.4}{5}$	1.7	2.7	3.1	4.5	4.6	6.0

Additionally, as a result of experimentation and simulation, it can be concluded that increasing the amplitude of the wave, the speed of the robot increases. Moreover, from the experimentation and simulated motion of the robot it was possible to see that the point of contact moves along the body of the snake periodically, which resembles the parodic contact between a rotating wheel and the ground. Hence, one can intuitively model pedal wave

motion performed by the snake robot as the motion of a wheeled mobile robot along a straight line, where the number of wheels, i.e. number of contact points at each time, depends on ϕ, the radius of wheels depends on A and the rotational velocity of wheels depends on ω (see Figure 5.7). This makes it easy to intuitively understand the effect of gait parameters on the forward speed of the robot. For example, to increase the speed of the snake robot one can increase the amplitude of the sinusoidal gate, which is limited by the mechanical design of the robot (i.e.$A_{max} = \frac{\pi}{3}$) or the temporal frequency ω as long as satisfactory tracking can be guaranteed.

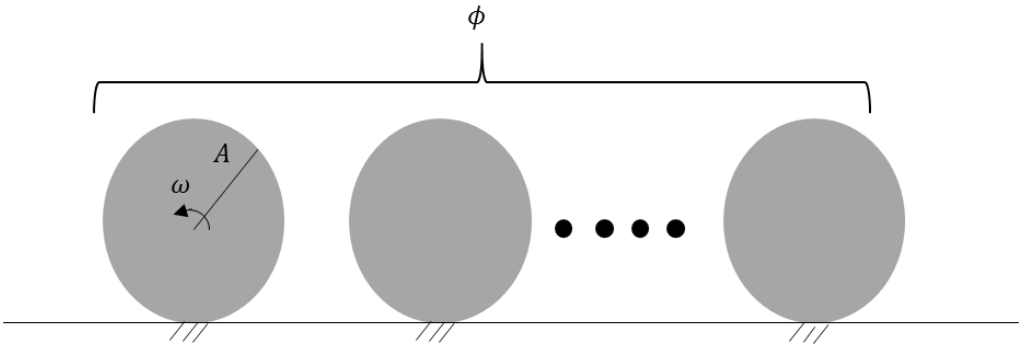

Figure 5.7. The simplified pedal wave motion model.

5.5 The Effect of Friction on the Snake Robot Pedal Wave Motion

Another important experimentation is to investigate the effect of varying the friction property of the surface to obtain more insight into pedal wave motion of the simulated and physical robot. As it can be seen in Figure 5.8, an experiment was designed, where the robot is first moving on the top of a high friction surface (black plate) with $\mu_C = 0.82$ and then on a low friction surface with $\mu_C = 0.40$, where the friction coefficients are obtained experimentally using a force sensor measuring the required force to drag an object with a known weight on each surface.

From the experiment, it could be seen that the forward velocity of the robot on the surface with higher friction was approximately 20.3% higher than the velocity on the lower friction surface. Considering (4.35), one may expect that the velocity of the robot on high friction to be almost two times higher than the velocity on the lower friction surface as the external force in X direction linearly depends on μ_C. However, both the simulation results (13.7 percent increase) and experimental results suggested that, increasing the friction between the robot will cause the forward velocity to increase, but they are not linearly proportional. This suggests that in the future development of the robot, using materials with to cover the surface of the modules to increase the friction between the robot links and the environment is advised.

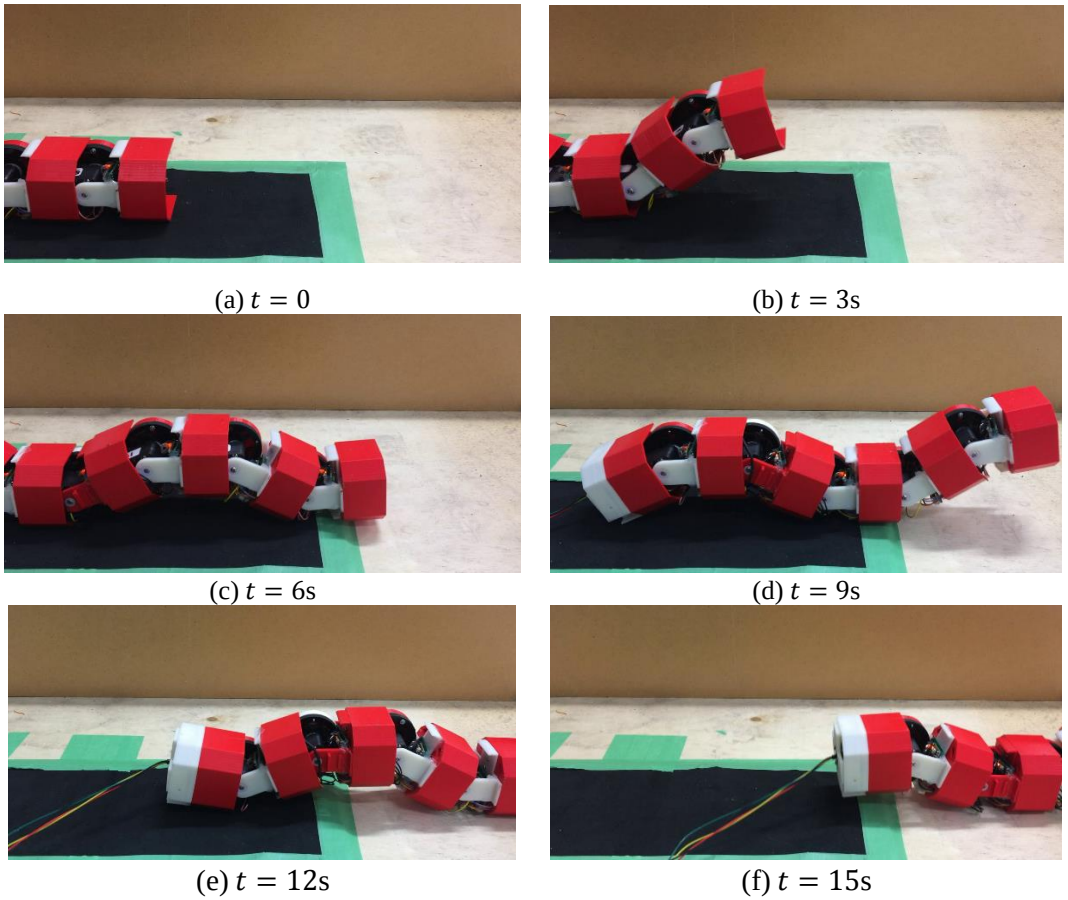

(a) $t = 0$ (b) $t = 3$s

(c) $t = 6$s (d) $t = 9$s

(e) $t = 12$s (f) $t = 15$s

Figure 5.8. Snake robot progression with pedal wave motion with $A = \frac{\pi}{4} rad$, $\omega = \pi\ rad.s^{-1}$ and $\phi = \frac{-2.2\pi}{5}\ rad$ first on high friction (black) and then on low friction surface.

As can be seen in Figure 5.9, after 7.5s, when the head module is touching the surface with low friction, the magnitude of the negative peaks of the torque signal have decreased slightly by about 2%. This phenomena was also observed in the experimental data, where the peak decreased by at least 4%, when moving from the high friction to low friction, which could be due the servo motor pushing harder against the ground and consequently exerting more torque on the surface with high friction. This result shows that such model is reliable enough for development, investigation and understanding of the pedal wave motion and can capture the fundamentals of such complex motion with reasonable accuracy. These results also support the idea that environmental contact forces and inadequate accuracy to model the friction are the main reasons why the simulation model cannot accurately model the physical snake robot.

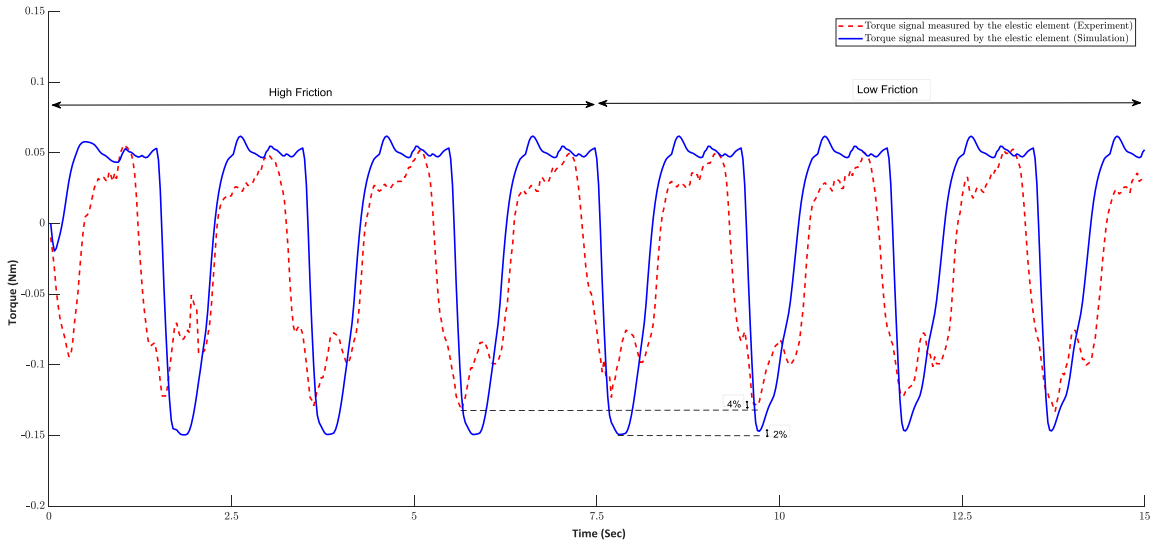

Figure 5.9. Comparison between the torque signals experimentally measured by the elastic element of the head joint (joint 1) and the same quantity obtained from the simulation.

The experimental results presented in this chapter, showed that the snake robot developed with SEA is an effective robotic mechanism, which can generate pedal wave motion. The simulation results also showed that such complicated motion can be described

by the developed equations of motion in (4.35) with expected discrepancies and the model can capture the fundamentals of pedal wave motion. Thus, it provides us with a powerful tool to investigate pedal wave motion in more details.

5.6 Summary

In this chapter, the position control (4.39) was implemented on both the physical robot and the simulated model to generate pedal wave motion on smooth surfaces. It was shown that such controller can be used successfully to generate pedal wave motion by both the simulated and experimental model on smooth surfaces. Moreover, simulation and experimental results were compared, which demonstrated an acceptable level of model accuracy, where correlation coefficient R indicating the similarity between the signals was calculated to be 0.8336. The effect of gait parameters on the pedal wave motion of the robot were examined, which showed that the average speed of the robot predicted from the simulation was 22.2% lower than the speed obtained from the experimentation mainly due to the inaccuracy of contact modelling. The effect of friction on the motion of the robot was investigated, which showed that the robot average speed is positively correlated with the friction coefficient of the surface supported by both the simulation and experimentation results.

6

LOCAL STIFFNESS CONTROL STRATEGY FOR PEDAL WAVE LOCOMOTION ON SURFACES WITH IRREGULARITIES

6.1 Introduction

Although pedal wave locomotion on smooth surfaces can be generated using a pre-defined gait pattern with a fixed set of parameters (see Figure 5.1), such a strategy without being accompanied by environmental sensory data is not very effective on uneven terrain. Taking advantage of the snake robot with SEAs, it is possible to use the torque signal measured with the elastic element as an environmental feedback signal and incorporate it into the snake robot controller to achieve effective pedal wave motion on surfaces with irregularities.

However, designing a control concept enabling effective incorporation of this feedback signal into the snake robot controller is challenging.

In this chapter, a straight-forward method based on admittance control concept is introduced to incorporate the motor torque signal into the snake robot controller for producing pedal wave motion on surfaces with irregularities. Employing this distributed admittance controller, it will be shown that the robot joint stiffness can be controlled using motor torque feedback signals measured by the elastic elements enabling active control of the dynamics of the interaction between the robot and the environment. Finally, we experimentally investigate the effectiveness of such control scheme and evaluate its efficacy for achieving adaptive pedal wave motion to climb over a step-like obstacle.

6.2 Local Stiffness Control Strategy: Motivation

In contrast to lateral undulation, in which the robot body is always in contact with the ground, in pedal wave motion and sidewinding [111] (3D generalization of pedal wave motion), the robot lifts its body sections periodically off the ground and pushes against the ground using the rest of its body to move forward. The fact that the robot lifts its body makes pedal wave motion an ideal locomotion pattern for climbing over an obstacle located on the robot path as a very common scenario in real word environments.

Figure 6.1 illustrates the body shape of a 2D snake robot with five joints, performing pedal wave motion at a particular instance in time, where X, Z are the global coordinate frames, α_is are the relative joint angles, l_i is the i^{th} body link, $l_{2,6}$ are assumed to be in contact with the ground at points $p_1$and p_2, (x_c, z_c) locates the centre of mass of the robot

and there is a stair-like obstacle on the robot path, which the robot should climb over to move forward.

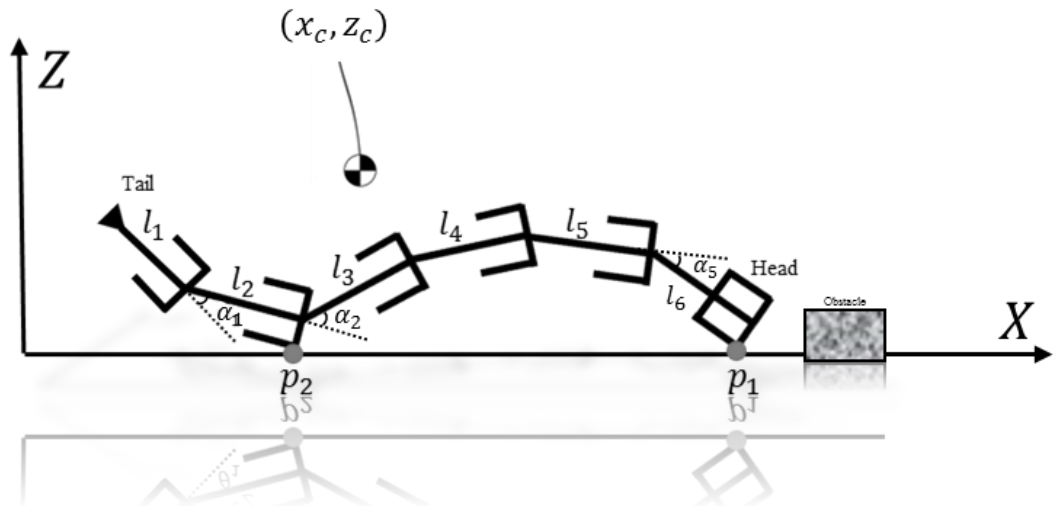

Figure 6.1. Body shape of a six link snake robot during pedal wave motion.

This locomotion mechanism has some similarities with legged locomotion, in which the foot comes into contact with the ground and normal reaction and friction forces are the main propulsive forces, moving the robot forward. However, unlike locomotion on smooth surfaces, achieving such motion patterns on uneven surfaces is challenging. Because the robot might be stuck, when the environmental forces in *X* direction partially cancel each other or might roll-over to one side when the projection of the centre of mass along the direction of gravity leaves the convex hull of the contact points.

Recently, it has been shown that human runners, can control their leg stiffness in response to varying terrain conditions for disturbance rejection [27] passive stability [112] and higher efficiency [113]. The analogy between the human walking and pedal wave motion of snake robots, suggests that stiffness control strategy can also be useful for achieving pedal wave locomotion on surfaces with irregularities using the designed snake robot with SEAs presented in this thesis. Employing such a strategy, it is possible to actively

control the interaction between the robot links and the environment using motor torque feedback signal and achieve compliant motion on uneven surfaces. This makes such strategy a straightforward method to incorporate the torque signal measured with the elastic element into the snake robot controller to modulate the joint angle position references and achieve pedal wave motion on surfaces with irregularities.

6.3 Local Stiffness Control Design for Modular Snake Robots with SEAs

Considering the output torque feedback signal, measured by the SEA, it is possible to control the dynamical relation between the joint positions and the applied external forces to the environment [114]. This can be achieved employing a cascade controller, where the outer control loop modulates the reference for the inner control loop using motor torque feedback signal. If the inner control loop is a position/force controller and the outer control loop is chosen to be a force/position controller, the resulting control structure is called admittance/impedance control [115]. This means that, instead of pure position or force control, such structure controls the relationship between these two quantities to impose a certain behavior, such as a spring with desired stiffness. This can be extremely useful in a snake robot pedal wave locomotion to achieve effective motion by actively controlling the dynamical interaction between the robot and the environment.

To design a stiffness controller for the snake robot to achieve pedal wave motion on surfaces with irregularities, we propose a local stiffness control strategy, i.e. the position control loop is closed at motor angle level, with the block diagram shown in Figure 6.2, where K_d is the desired stiffness of the joints, C_p is the PD position controller (4.39), K is

the stiffness of the elastic element, $\boldsymbol{\beta} = [\beta_1, \beta_2, \dots, \beta_{N-1}]^{\mathrm{T}}$ is the vector of relative rotor angles, $\boldsymbol{\alpha}^d$is the is the vector of desired relative link angles generated by gait equation (4.38), $\boldsymbol{\alpha}_s = \frac{\mathrm{K}-K_d}{K_d}\,\boldsymbol{\tau}_J$ representing the desired admittance, $\boldsymbol{\alpha}$ is the is the vector of relative joint angles and $\boldsymbol{\tau}_J$ is the vector of servo motors measured output torque signal.

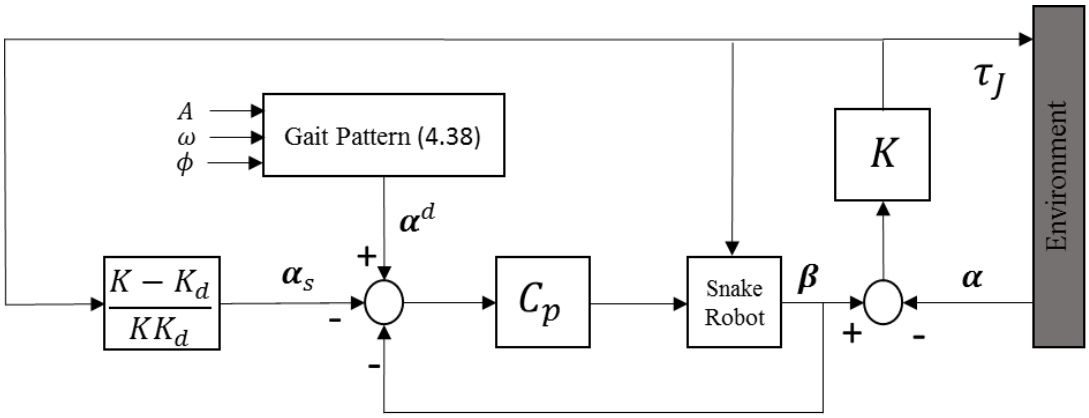

Figure 6.2. Snake robot local stiffness control block diagram.

As it can be seen in Figure 6.2, gait pattern (4.38) is still used to generate the desired joint angles. The reason is that although predefined gait patterns are not useful on uneven surfaces, considering the complexity of the motion and hyper redundancy of the snake robot, such gait pattern can be used to efficiently generate the desired joint angles. However, unlike controller (4.39), which was a pure position controller, the controller in Figure 6.2 uses the measured motor torque $\boldsymbol{\tau}_J$ in the outer force control loop to modulate the reference position of the inner position control loop depending on the value of control gain K_d, i.e. the desired stiffness.

Another important consideration about the controller in Figure 6.2, is the bound on K_d , which should be imposed to guarantee the stability of the closed loop system. To obtain such a bound, it is enough to check the passivity of the impedance relation, $Z(s) = \frac{-\boldsymbol{\tau_J}}{\dot{\boldsymbol{\alpha}}}$,

making sure the output energy of the system will not become greater than its input energy [114]. For the snake robot with identical joints, we can obtain such condition for one joint and consider the whole system as the connection of passive elements. Hence, it is possible to use the well-known stability condition of admittance controllers stating that the desired stiffness must be higher than the stiffness of the attached elastic element (i.e. K_d <K). Otherwise, it behaves as a spring with negative spring constant, which is not physically possible.

6.4 Experimental results for local stiffness control strategy

To better show how the proposed controller works in practice, the controller structure shown in Figure 6.2, was implemented on the snake robot. C_p was chosen to be the controller in (4.38) and $\boldsymbol{\alpha}^d$ was generated as follows:

$$\boldsymbol{\alpha}^d = \boldsymbol{A}\, sin(\omega t) \tag{6.1}$$

where $\boldsymbol{A} = \left[0,0,\dots,0,\frac{\pi}{4}\right]_N^T$, $N = 5$, $\omega = \pi\ rad.s^{-1}$. Hence, only the head module oscillates and other joints will remain stationary enabling investigation of the effect of stiffness control (varying K_d) on a single joint of the robot. (See Appendix C, Supplementary Material C.2 showing the experiments for a single joint with $\boldsymbol{A} = [0,0,\dots,0,0]_N^T$).

As shown in Figure 6.3.b the joint will be at rest on the ground when $\alpha_5 = 0$, is free to move when $\alpha_5 > 0$ and will push against the ground (i.e. reaction force $\boldsymbol{\tau_J}$ will be exerted on the link) when $\alpha_5 < 0$. During the test, the values of K_d was changed, after five complete cycles while the joint was in motion to collect enough samples to investigate the effect of varying joint stiffness on the joint angle. The measured motor angle then recorded while sampled at 1KHz as shown in Figure 6.3.b.

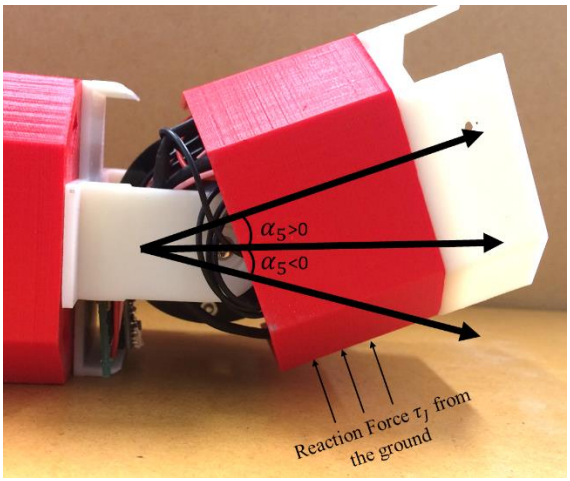

(a) Experiment setup

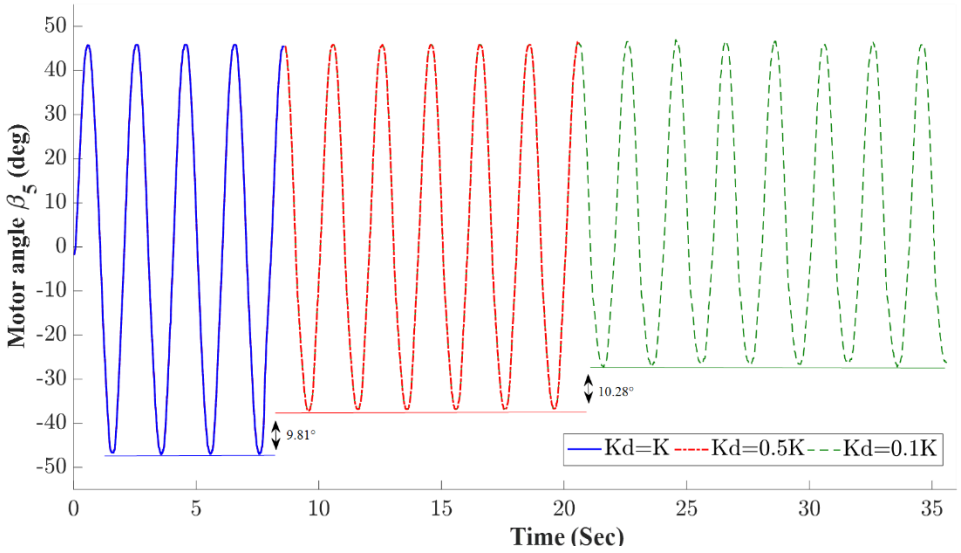

(b) Effect of $\boldsymbol{K_d}$ on joint angle β_5.

Figure 6.3. The effect of varying joint stiffness on motion of the head module.

As can be seen from Figure 6.3.b, the servo motor starts to oscillate with $K_d = \mathrm{K} = 1.75$ while successfully tracking the commanded motor angle. This means that at the beginning of the experiment, where $K_d = \mathrm{K}$, the robot pushes against the ground and no matter how much is the reaction force, the servo motor is only in position control mode and $\boldsymbol{\alpha}^d \cong \boldsymbol{\alpha} = \boldsymbol{\beta}$. On the other hand, when the value of K_d changes to 0.5K, the joint still tracks the commanded trajectory when there is no environmental torque, however when $\alpha_5 < 0$,

the joint pushes against the ground and because $\boldsymbol{\tau_J} \neq 0$ the admittance control comes into effect and depending on the value of K_d the actual joint angle deviates from the commanded trajectory, thus $\boldsymbol{\alpha}^d \neq \boldsymbol{\alpha} \neq \boldsymbol{\beta}$. Consequently, this experiment shows that by changing the joint stiffness, the joint angle can adaptively change during the motion of the robot based on the contact forces from the environment even when $\boldsymbol{\alpha}^d$ (i.e. gait parameters) remain constant.

To examine the effect of stiffness control strategy shown in Figure 6.2, on the pedal wave motion of the robot, another experiment is designed. In this experiment, C_p is chosen to be the controller in (4.38) and $\boldsymbol{\alpha}^d$ is generated based on the pedal wave motion pattern (4.38) with $A = \frac{\pi}{4} rad$, $\omega = \pi\, rad.s^{-1}$ and $\phi = \frac{-2\pi}{5} rad$ to enable the robot to move over an obstacle with height 36mm and width 107mm located on the robot path as shown in Figure 6.4. The experiment was conducted on the robot starting from a same initial position relative to the obstacle and repeated five times with $K_d = \mathrm{K}, \frac{\mathrm{K}}{2}, \frac{\mathrm{K}}{3}, \frac{\mathrm{K}}{4}, \ldots, \frac{\mathrm{K}}{10}$, (K is the stiffness of the elastic element) to investigate the effect of varying joint stiffness.

As a result of the test, the control strategy with K_d =K (without stiffness control) proved to be totally ineffective in every trial, due to the robot getting stuck or the whole robot "rolling-over" to one side. On the other hand, the stiffness control strategy with $K_d = \frac{\mathrm{K}}{6}$ proved to be effective and enabled the robot to traverse over the obstacle in every five trials, where by average it took 24.6s for the whole robot to move over the obstacle (See Appendix C, Supplementary Material C.3).

Figure 6.4 shows this experiment, where the robot successfully moves over a stair-type obstacle with the height of 55% of the diameter of snake robot modules, where the blue plate attached to the top of the obstacle is only for higher friction and to avoid slipping and

was consistent for every experiments. As can be seen in Figure 6.4, the robot is actually touching the obstacle and moving over it, instead of trying to avoid collision. Moreover, the robot was not provided with any information about the position or dimension of the obstacle or any other type of feedback signal other than the motor output torque. Hence, the side stability is achieved only because of the compliance of the joints. However, it should be mentioned that, in case the amplitude of the wave, i.e. A, is small compared to the height of the obstacle, visual feedback from the head module camera should be combined with the presented method to increase the amplitude of the wave if necessary.

(a) $t = 0$ (b) $t = 3$s

(c) $t = 6$s (d) $t = 9$s

(e) $t = 12$s (f) $t = 15$s

(g) $t = 18$s (h) $t = 21$s

(i) $t = 22$s (j) $t = 24$s

Figure 6.4. The robot climbing over an obstacle

The compliance of the joints in this experiment plays the most important role to achieve adaptability. In this test, once the robot touches the obstacle, the motor torque signal, measured by the elastic element will be treated as a feedback signal, as shown in Figure 6.2 to alter the commanded joint angles, this is also evident in the experiment shown in Figure 6.3.b where changing the joint stiffness resulted in adaptation of the joint trajectory. Hence, as the result of using this control strategy the robot joints behave like a virtual spring (in response to external forces), for which stiffness can be varied actively.

An important result of this experiment was that side stability is the most critical issue limiting the capabilities of the snake robot pedal wave motion on surfaces with irregularities. This experiment showed that on uneven surfaces the robot can easily roll over to one side when moving over the obstacle because of the lack of side stability due to narrow width of the robot links and uneven distribution of the mass within each link. This was not an issue with the pedal wave motion on a smooth surface, because the robot traverses on a straight line and the centre of mass of the robot will be located inside the convex hull of the contact points. However, on surfaces with irregularities, this is a major concern, which the proposed stiffness control strategy partially address by decreasing the amplitude of the oscillation of the joints as shown in Figure 6.3. Hence, the centre of mass of the robot (located approximately in the middle of the robot) remains closer to the ground compared to the open-loop control strategy, which increases the side stability in return.

Although local stiffness control strategy partially solved side instability issue, further experimentation proved that side stability in more challenging environments needs to be addressed more effectively. In these environments, the robot could be in contact with several surfaces, i.e., the ground, sides of the obstacles and top of the obstacles at the same time. Hence, even using the local stiffness control strategy, the snake robot can easily roll over to

one side (See Appendix C, Supplementary Material C.4). This suggests that, further research leading to the design of an effective controller enabling the robot to deal with single and multiple obstacles is still required. These developments will be discussed in more details in the next chapter.

6.5 Summary

As a straightforward method to incorporate the measured motor torque signal and inspired by human walking, we proposed the local stiffness control method for effective pedal wave motion on surfaces with irregularities. To investigate the effectiveness of such active stiffness control strategy, an admittance controller was designed and implemented, and its effect studied in a single joint of the robot, which showed that by changing joint stiffness, the trajectory of the joint can be changed in response to external forces. Such a controller was implemented on the snake robot, which enabled the robot to successfully climb over an obstacle with the height of 55% of the diameter of snake robot modules, which was not possible with open loop controller. This showed that compliance is indeed an effective strategy for generating effective pedal wave motion for climbing over a single obstacle. Experimentations were also conducted to examine the effect of such control strategy in environments with multiple obstacles, which suggested that the proposed controller needs to be modified to make sure it can be employed in more challenging environments.

7

TAIL-LEADING STIFFNESS CONTROL STRATEGY FOR PEDAL WAVE LOCOMOTION ON SURFACES WITH IRREGULARITIES

7.1 Introduction

The local stiffness control discussed in the previous chapter was designed with the use of local torque feedback signals and an admittance control scheme, which enabled the robot to climb over a single obstacle. However, experimentation showed that using this strategy the snake robot cannot effectively deal with multiple obstacles due to the robot rolling over to one side. This suggested that more effective control strategies enabling the robot to perform pedal wave motion in environments with multiple obstacles are required to be designed.

In the local stiffness control discussed in Chapter 6, the motion of each joint was generated independent of the motion of other modules. Hence, the motor output torque measured by the elastic element at each joint could only modulate the corresponding joint reference position. However, it is possible to use the vector of joints measured position and propagate it along the snake robot body (with the use of CAN bus system) to potentially generate more effective pedal wave motion in environments with multiple obstacles. Thus, in this chapter, we propose an extended stiffness control scheme by establishing a feedback connection between the consecutive joints and present simulation and experimental results to analyse and examine this strategy.

7.2 Tail-Leading Stiffness Control (TSC) Strategy

In the local stiffness controller proposed in the previous chapter, the measured motor torque signal was only used in the controller of the same joint. Moreover, in this controller, the reference joint angles were generated by a gait pattern without any feedback connection. Thus, there was no coordination between the oscillations of each joint. However, coordination between the joints motion while traversing the obstacles can potentially improve the performance of the robot on surfaces with irregularities as the joints receive information about the environment through the position feedback connection between the joints.

To overcome the aforementioned issues, we propose an extended stiffness controller, named Tail-Leading Stiffness Control (TSC). In this strategy, the joint reference angle for the servo motor at the tail module is generated based on the following sinusoidal wave:

$$\alpha_1^d = A\,sin(\omega t) \tag{7.1}$$

where A is the amplitude and ω is the frequency of the wave, which similar to (4.38), doesn't require any environmental feedback signal.

However, in TSC strategy the position reference for j^{th} joint is designed to be generated based on the following differential equation:

$$M_d\ddot{\alpha}_j^d + D_d\dot{\alpha}_j^d + K_d\left(\alpha_j^d - \alpha_{j-1}\right) = -K_\tau\tau_j \tag{7.2}$$

where $j = 2, 3, \dots, N-1$, α_j^d is the reference angle for j^{th} joint, α_{j-1} is the measured joint angle of the previous joint, M_d, D_d and K_d are the desired inertia, damping and stiffness, respectively, and K_τ is the controller gain to be chosen.

From (7.1), it can be seen that, the first joint reference angle (tail module), is being generated based on a sinusoidal wave, without any feedback from the neighbouring joints or the environment. However, the reference joint angle of other joints (α_j^d) is being generated based on (7.2) with a feedback from measured joint angle of their preceding joint (α_{j-1}). This means that for $j = 2, 3, \dots, N-1$, (7.2) generates α_j^d (the desired joint angle), by tracking α_{j-1}. However, this is a special tracking controller, which also uses the motor torque signal τ_j to modulate the reference joint angle. This view of (7.2) suggests that M_d, D_d and K_d should be tuned to avoid undesirable behaviours, such as overshoot, steady state error and large settling time to make sure each joint can track the joint angles of the previous joint to generate desired net motion.

Equation (7.2) can also be seen as an admittance controller [116]. Hence, M_d, D_d and K_d are desirable inertia, damping and stiffness. This view, which is more in harmony with

the local stiffness control method presented in the previous chapter, suggests that by changing M_d, D_d and K_d, it is possible to control the dynamics of interaction between the joints and the environment. For example by increasing K_τ, while keeping K_d constant the joint will become more compliant, because the measured feedback τ_j, causes the generated joint position to deviate more from its reference position. The block diagram of this controller is shown in Figure 7.1.

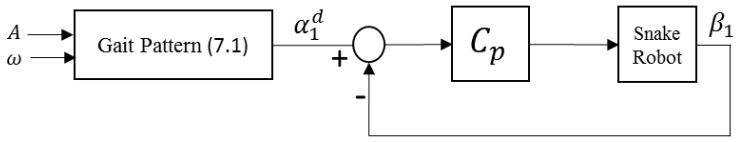

(a) The designed controller for the tail module (first module).

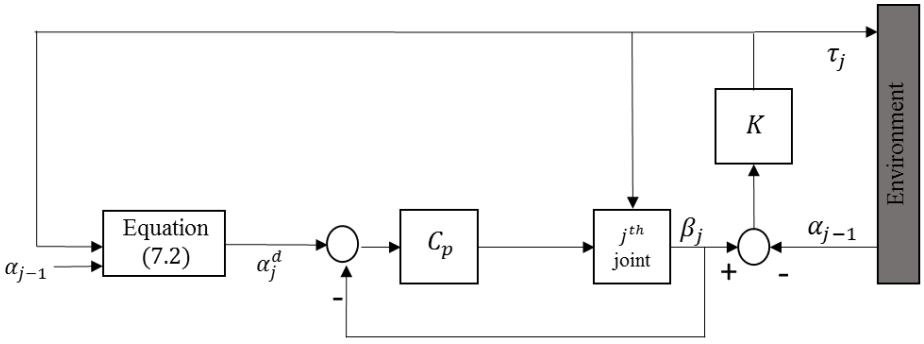

(b) The designed controller for j^{th} joint, where $j = 2, 3, \dots, N-1$.

Figure 7.1. The block diagram of Tail-Leading Stiffness Control (TSC) strategy.

As can be seen in Figure 7.1, the measured motor torque signal is fed into (7.2) to modulate the reference for the inner position control loop, similar to a conventional admittance control scheme. Moreover, as shown in Figure 7.1 the reference joint angle (α_j^d) is generated using the feedback from the previous-joint position (α_{j-1}), employing a same type of controller. Hence, TSC strategy allows the joint angles modulated by the torque feedback signal to be propagated from the tail to head using a position feedback from

consecutive joints. Appendix C, Supplementary Material C.5, shows the external force exerted on a single joint of the robot modulates the position of that joint, which also propagates along the snake robot body.

7.3 TSC Strategy: Simulation-based Analysis

The presented dynamical model in (4.35) is an effective tool allowing to investigate the fundamentals of TSC strategy on surfaces with irregularities (See Figure 4.4, showing how the proposed contact model can be employed to model these environments). To achieve this goal, TSC strategy is implemented on the robot in the simulation environment with an obstacle with the height of 36mm and width 107mm located 150mm away from the tip of the head module with the simulation parameters presented in Table 5.1. To better examine the fundamentals of the TSC strategy with combined stiffness control and position feedback, the open-loop controller based on gait pattern (4.38) is also implemented on the simulated snake robot. The parameters of these controllers are shown in Table 7.1 and the resulted motions are shown in Figure 7.2.

Table 7.1 The parameters of the tested controllers. (All units are in SI, unless specified)

Controller	Parameters
Open-loop controller based on gait pattern (4.38)	$A = \frac{\pi}{6}$ $\omega = \pi$ $\phi = \frac{-2\pi}{5}$
TSC strategy	$A = \frac{\pi}{6}$ $\omega = \pi$ $M_d = 1$ $D_d = 4$ $K_d = 12$

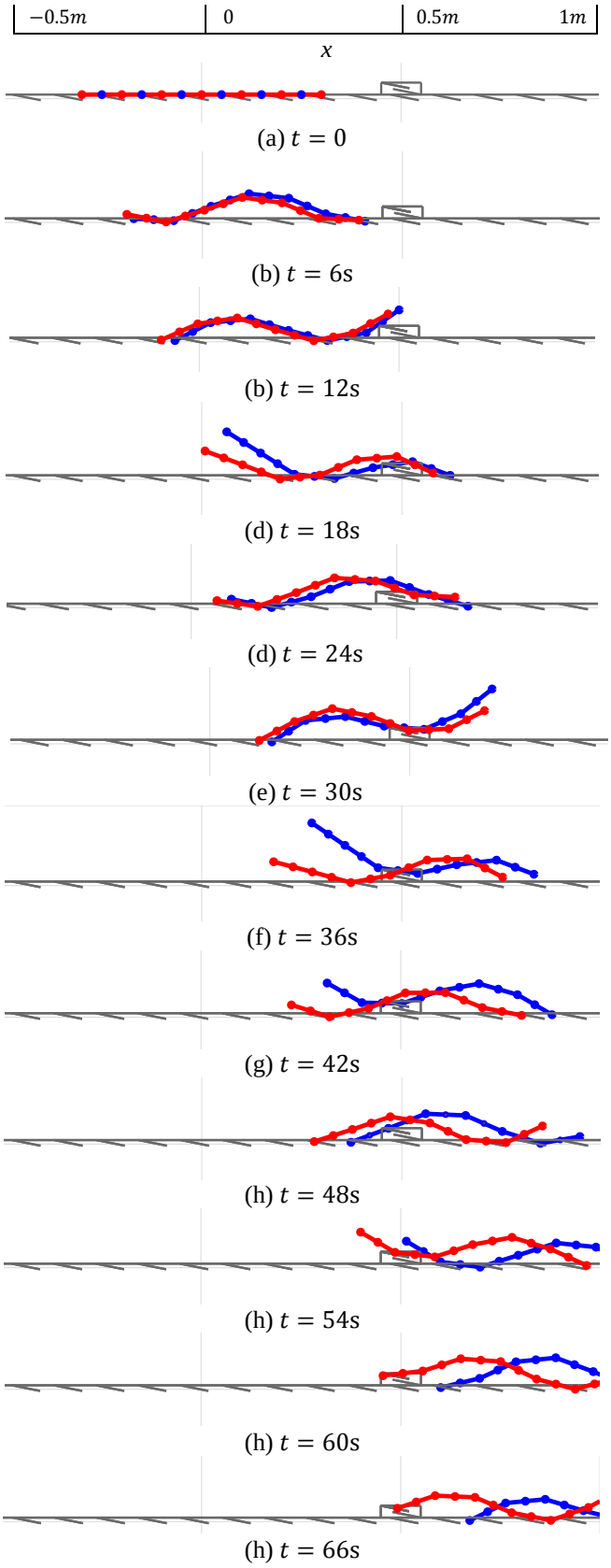

Figure 7.2. Comparison between pedal wave motions generated by TSC strategy (blue) and Open-loop controller based on gait pattern (4.38) (red).

Figure 7.2 shows the pedal-wave motion of the snake robot climbing over the obstacle with TSC strategy (blue) and the open-loop controller based on gait pattern (4.38) (red) with the parameters shown in Table 7.1 As it can be seen from the results, the simulated robot has successfully climbed over the obstacle with the use of both control strategies, where the amplitude and the time frequency of the generated waves were the same. However, TSC strategy with the specified control gains, enabled the robot to climb over the obstacle with 25.6% higher average speed compared to open-loop controller based on gait pattern (4.38).

Figure 7.3 is provided, which shows the joint angles of three joints of the robot (for t between 0 to $25sec$) compared to the open-loop controller. As it can be seen in Figure 7.3 using both TSC strategy and the open loop controller the motor angle of the first joint (Tail module) remains unchanged as it generates the oscillatory motion to be propagated along the body. However, the motor angle of the third and the head module generated based on TSC strategy differ from the ones generated by the open loop controller in terms of the amplitude and phase shift of the waves, which shows that in TSC strategy both the amplitude and the phase shift of waves are modulated.

As it can be seen in Figure 7.2, it is possible to divide the total locomotion time into three intervals,T_1, T_2 and T_3 to compare the effect of TSC strategy on the snake robot before touching the obstacle, while in the contact with the obstacle and when it has completely climbed over the obstacle. As it can be seen in Figure 7.4, during T_1 and T_3, when the robot is moving on a smooth surface, each cycle of the periodic motor torque signal is identical to other cycles within that interval. However, during T_2, which at least one link is in contact with the obstacle, it can be seen that the measured motor torque signal is no longer similar to the measured motor signal during T_1 and T_3.

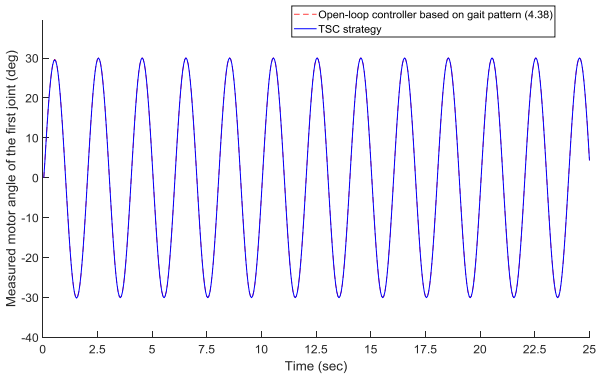

(a) Measured motor angle of first joint (Tail module).

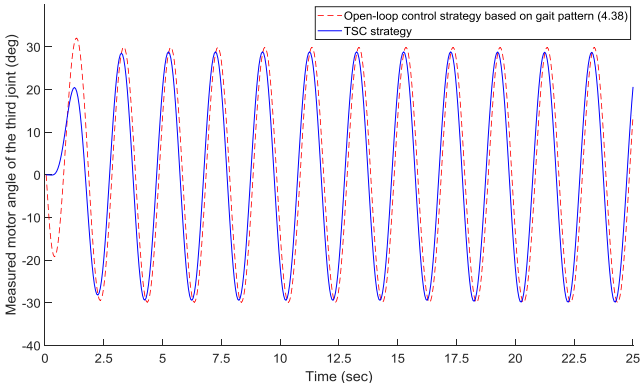

(b) Measured motor angle of third joint.

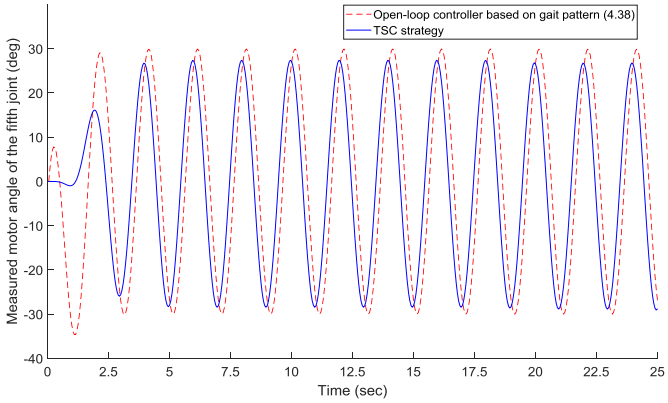

(c) Measured motor angle of fifth joint (Head module).

Figure 7.3. Comparison between the joint motion generated by TSC strategy and open-loop controller based on gait pattern (4.38).

This means that the reference joint angles generated based on (7.2), will be similar during T_1 and T_3 (on a smooth surface) and will adaptively change during T_2, when the

robot is in contact with the obstacle. This is also shown in Figure 7.5, where the motor joint angle of the joint 5 (head module) is presented and intervals T_1, T_2 and T_3 are specified.

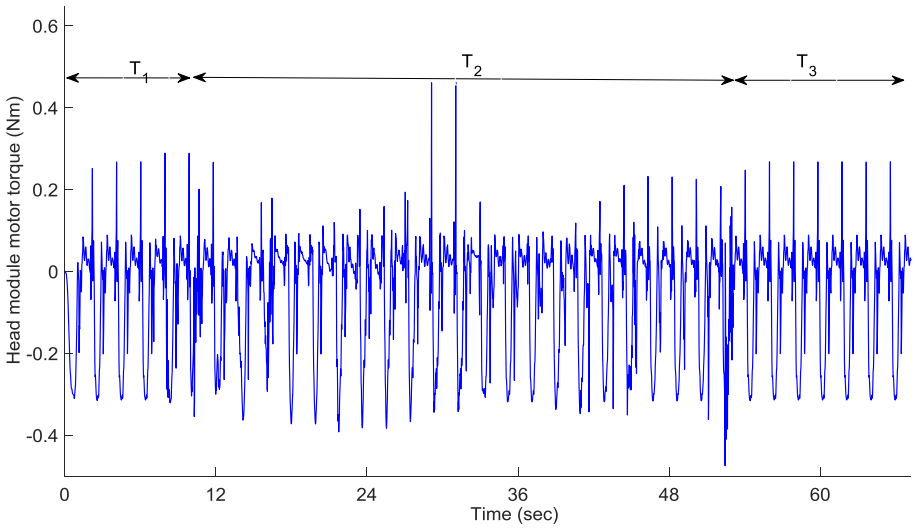

Figure 7.4. The motor torque signal measured by the elastic element at the head module for the generated pedal wave motion shown in Figure 7.2.

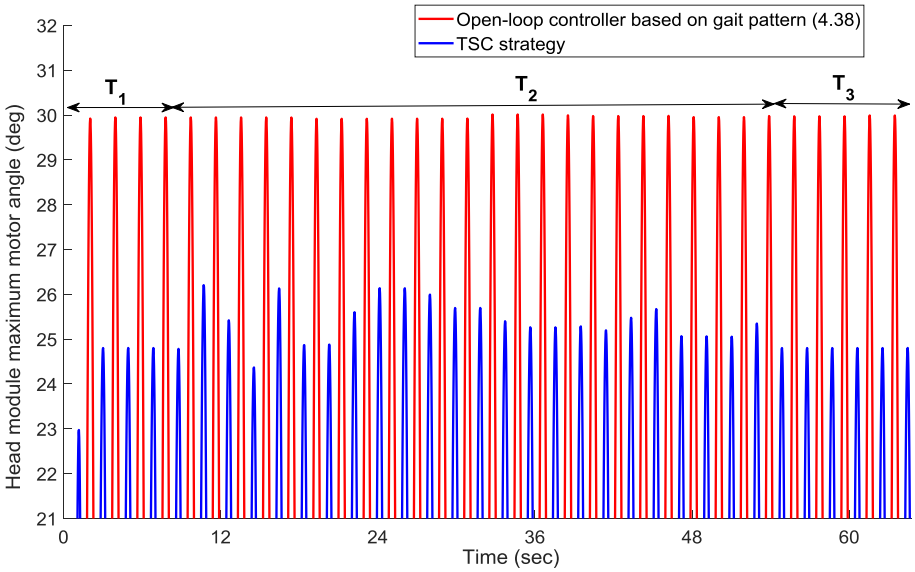

Figure 7.5. The variation of the maximum measured joint 5 motor angle for the generated pedal wave motion shown in Figure 7.2.

As it can be seen from the results, when the robot is moving on a smooth surface, the motor signal will be the same in each cycle because the environmental conditions are not

changing and therefore controller (7.2) generates the same reference angles (in steady-state). However, once the robot encounters an obstacle, there will be irregularities in the measured torque signal of each joint, which modulates the reference angles of every joints of the robot.

7.4 TSC Strategy: Experimentation Results

Although the simulation-based analysis described the fundamentals of the TSC strategy, experiments enable to investigate the effectiveness of the proposed TSC strategy implemented on the physical robot. One of the main motivations for experimentation is that the presented modelling framework only describes the motion in XZ plane and lateral forces in Y direction cannot be taken into account. This was not an issue, when simulating the pedal wave motion on smooth surfaces. However, on uneven terrain, uneven distribution of the mass of the robot within the links and other un-modelled external forces, might cause the robot to roll over, which cannot be modelled using the simulation framework.

The designed experiment required the snake robot to climb over a single obstacle, to be repeated five times as shown in Figure 7.6. The results showed that the robot can successfully climb over a single obstacle with the height of 36mm and width 107mm located 100mm away from joint 5 (head module) with the use of the TSC strategy (with $A = \frac{\pi}{6} rad$, $\omega = \pi\, rad.s^{-1}$, $M_d = 1N.m.s^2.rad^{-1}$, $D_d = 10N.m.s.rad^{-1}$, $K_d = 17.5N.m.rad^{-1}$ and $K_\tau = 6$) in every five trials, where one of these successful attempts is shown in Figure 7.6. Experimental results also showed that, local stiffness controller (with $A = \frac{\pi}{6} rad$, $\omega = \pi\, rad.s^{-1}$, $\phi = \frac{-2\pi}{5} rad$, $\frac{\mathrm{K}-K_d}{K_d} = 6$) enables the robot to climb over the obstacle. However, the open-loop controller based on gait pattern (4.38) (with $A = \frac{\pi}{6} rad$, $\omega =$

$\pi\ rad.s^{-1}$, $\phi = \frac{-2\pi}{5} rad$) is totally ineffective because as expected, the robot rolled over to one side in every five trials due to side instability (See Appendix C, Supplementary Material C.6).

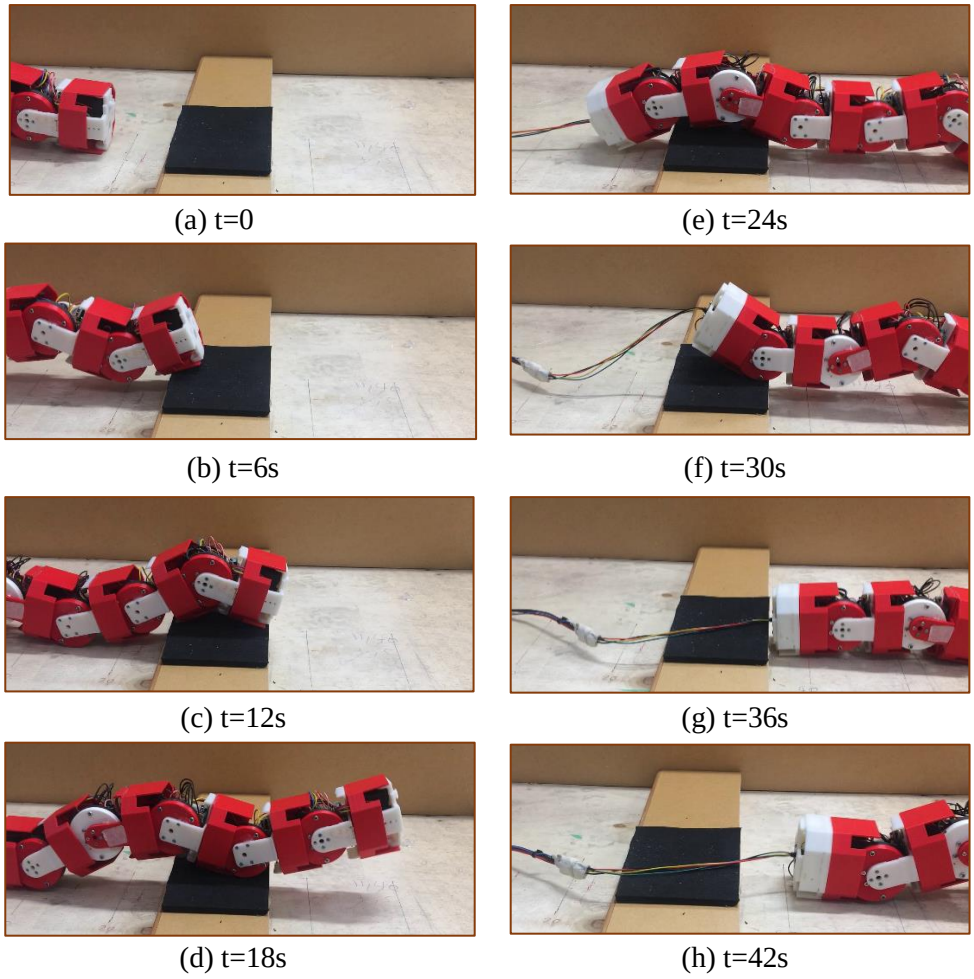

(a) t=0 (e) t=24s

(b) t=6s (f) t=30s

(c) t=12s (g) t=36s

(d) t=18s (h) t=42s

Figure 7.6. Snake robot climbing over a single obstacle with the use of TSC strategy with $A = \frac{\pi}{6}\ rad$, $\omega = \pi\ rad.s^{-1}$, $M_d = 1\ N.m.s^2.rad^{-1}$, $D_d = 10 N.m.s.rad^{-1}$, $K_d = 17.5\ N.m.rad^{-1}$ and $K_\tau = 6$.

To better show the effect of TSC strategy on the snake robot measured motor torque, Figure 7.7 is provided, which shows the motor torque signal measured by the elastic element at the third and fifth joint of the robot with $K_\tau = 6$. As can be seen in Figure 7.7, during the first stage of the motion, the robot is moving on a smooth surface and each cycle of the

motor torque signal remains similar to other cycles. However, as the robot touches the obstacle (at $t = 4s$), the motor torque values at each cycle no longer have any similarity. Hence, the adaptive strategy comes into effect when the robot is in contact with the obstacle and on smooth surfaces, where the torque signals at each cycle are the same the parameters of the oscillatory motion of the joints generated from (7.2) remain almost constant.

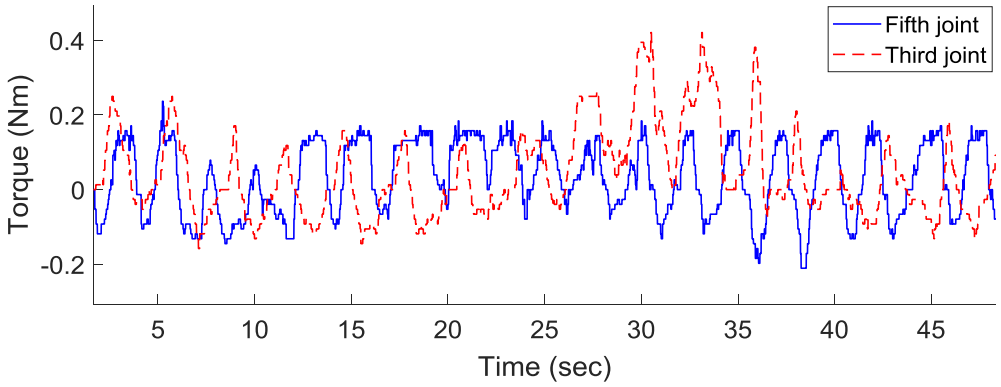

Figure 7.7. Motor torque signal measured by the elastic element for TSC strategy with $K_\tau = 6$.

As shown in Figure 7.7, similar to the local stiffness controller (also enabled the robot to climb over the single obstacle), in TSC strategy the motor torque of the joint closer to the middle of the robot (the centre of mass) is higher. Consequently, due to the stability of the admittance controller the amplitude of the motion of the middle joints becomes smaller compared to the joints far from the centre of mass, which positively affect the stability of the robot because the center of mass of the robot remain close to the ground.

7.4.1 The effect of position feedback in TSC strategy

To investigate the effect of position feedback in TSC strategy, another experiment is carried out in the same environment as shown in Figure 7.6 with $K_\tau = 0$ (other control parameters remained unchanged). This allows to investigate the effect of position feedback

on the robot motion as torque feedback will not have any effect on the motion, however the joints still receive the position feedback signal form the neighbouring joints.

The results showed that TSC strategy even with $K_\tau = 0$, enables the robot to completely climb over the obstacle with the average time of 40.1s (4.6% faster compared to the case with $K_\tau = 6$). This showed that the position feedback between the joints even without a torque feedback provides some degree of adaptability because unlike the open-loop gait based controller the snake did not roll over to one side. This experimentation showed that, the position feedback between the joints is also a critical factor enabling the snake robot to climb over the obstacle without rolling over to one side. When the snake robot climb over the obstacle, it will be in contact with different surfaces constraining the motion of the robot modules. Hence, the joint motion rarely matches with the commanded motion. In TSC strategy each joint follows the joint angle of the previous module. Hence, any unexpected changes in the joints motion due to environmental constraints (the obstacle) propagates along the body affecting the phase shift between the joints, which has improved the side stability of the robot in this experiment.

To better show the effect of position feedback in TSC strategy, Figure 7.8 shows the measured motor angle of the third and fifth joint of the robot using TSC strategy with $K_\tau = 0$ (without torque feedback) and $K_\tau = 6$ (both enabled the robot to successfully climb over the obstacle). As can be seen in Figure 7.8, varying K_τ changes the maximum amplitude and the phase difference between the generated oscillatory motions of the joints. Additionally, each cycle of the oscillatory joint motion is almost similar to the other cycles when the robot is moving on a smooth surface during the first ($t = 0 - 4s$) and the last stage of the motion ($t = 36 - 45s$). However, the parameters of the joint motion are

modulated based on the torque signal when the robot is in contact with the obstacle ($t = 4 - 36s$).

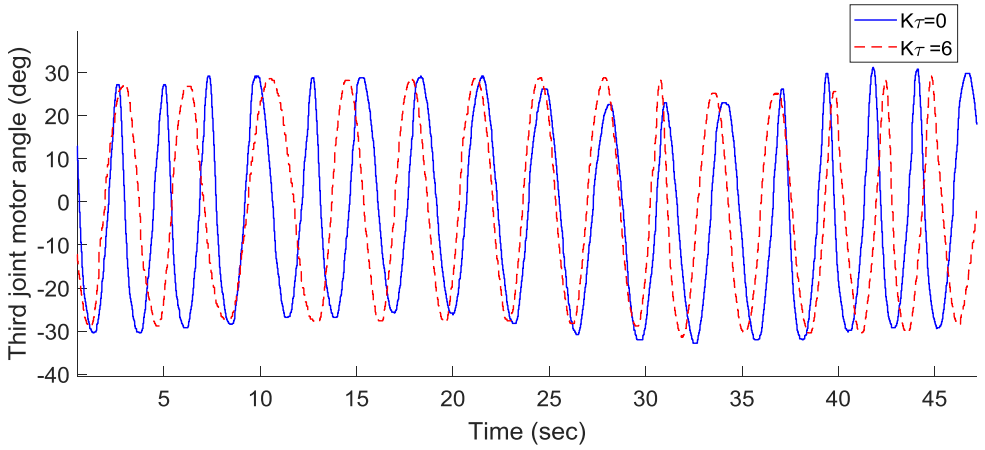

(a) Measured motor angle of the third joint.

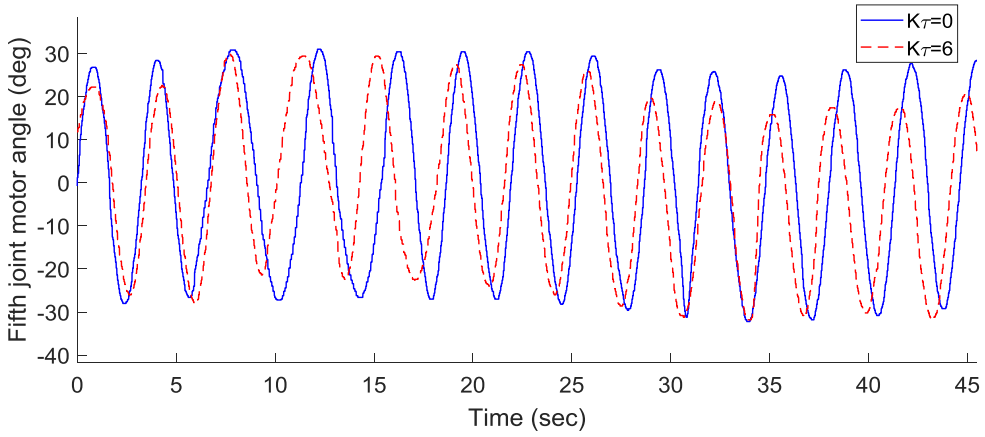

(b) Measured motor angle of the fifth joint.

Figure 7.8. Measured motor angle of the third and fifth joint of the snake robot while climbing over the obstacle shown in Figure 7.6.

Experimental results in Figure 7.8 showed that even for the case with $K_\tau = 0$, there is a difference between the motion of the joints at each cycle because of the position feedback between the joints. This suggests that TSC strategy even with $K_\tau = 0$ (without torque feedback) shows some degree of adaptability because of the position feedback connection between the joints.

7.4.2 TSC Strategy in environments with multiple obstacles

Experimentation in the previous section showed that TSC strategy with $K_\tau = 0$ (without torque feedback) and $K_\tau = 6$ enables the robot to climb over a single obstacle with the given dimensions. Moreover, as expected the local stiffness control also enabled the robot to climb over the obstacle. Hence, to investigate the importance of torque feedback and the possible superiority of the TSC strategy compared to local stiffness control, experiments in more challenging environments should be conducted.

For this purpose, the TSC strategy with $A = \frac{\pi}{6} rad$, $\omega = \pi\, rad.s^{-1}$, $M_d = 1N.m.s^2.rad^{-1}$, $D_d = 10N.m.s.rad^{-1}$, $K_d = 17.5N.m.rad^{-1}$, $K_\tau = 0$ (no torque feedback) and local stiffness control with ($A = \frac{\pi}{6} rad$, $\omega = \pi\, rad.s^{-1}$, $\phi = \frac{-2\pi}{5} rad$, $\frac{K - K_d}{K_d} = 6$) were implemented on the robot, where the snake robot was in contact with multiple obstacles. The results showed that the local stiffness control and the TSC strategy without torque feedback cannot enable the robot to climb over two obstacles and the robot rolls over to one side in very five trials (See Appendix C, Supplementary Material C.7). However, the TSC strategy with $K_\tau = 6$ (other control parameters remained unchanged), enabled the robot to climb over the obstacles within the average time of 27.4s. Figure 7.9, shows the snake robot climbing over two obstacles with the specified dimension using the TSC strategy with $K_\tau = 6$.

The results of this experiment showed that the promising performance of the TSC strategy is not only due to the position feedback between the joints. And the torque feedback is also a critical ingredient of TSC strategy. This is a very important result, because in less challenging environments (single obstacles) the experiments showed that TSC strategy without torque feedback also enables the robot to climb over the obstacle. However, the

results in environments with multiple obstacles confirmed that TSC strategy without torque feedback is no longer suitable and torque feedback should also be incorporated.

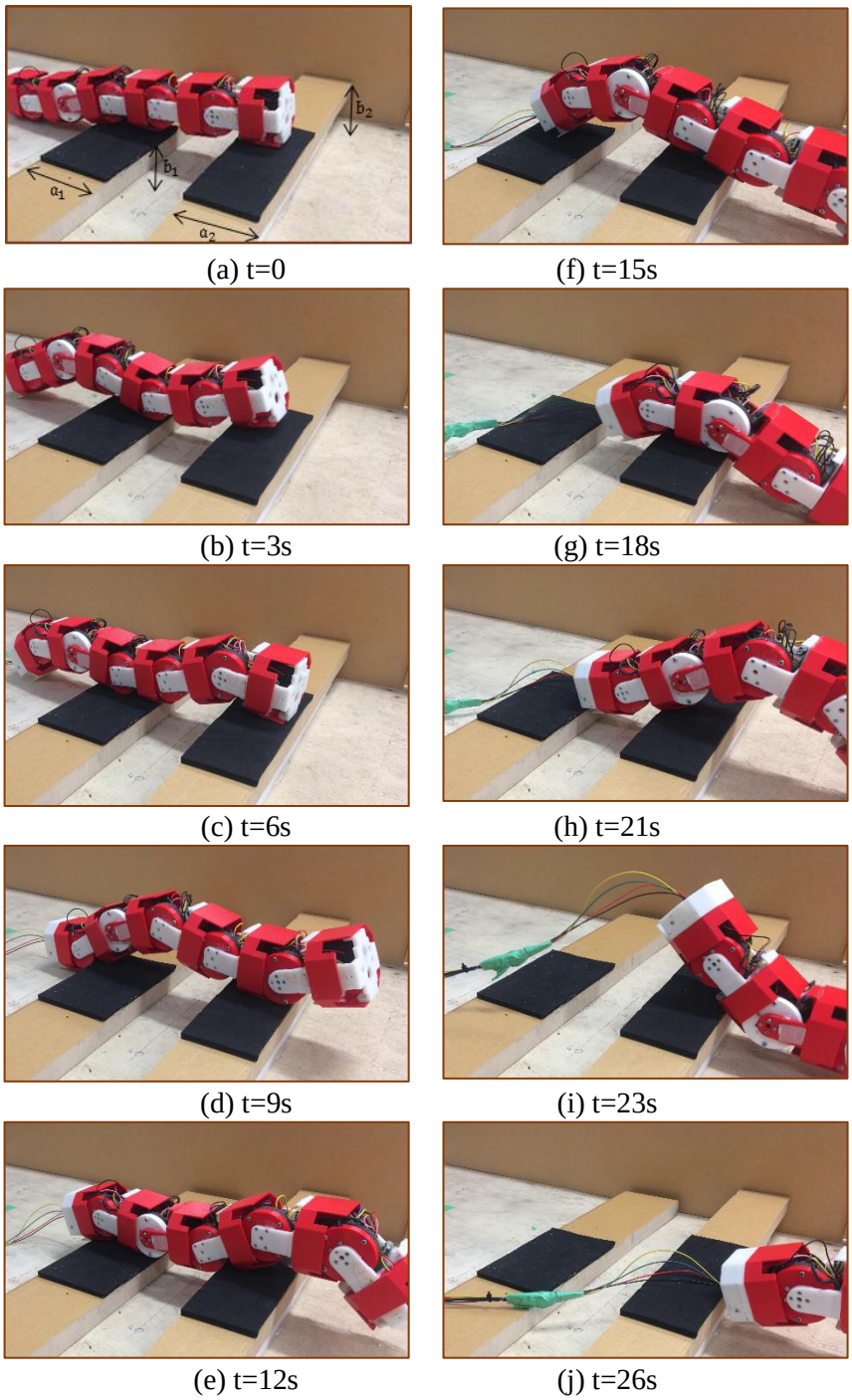

Figure 7.9. Snake robot climbing over multiple obstacle with the use of TSC strategy with $K_\tau = 6$. (Obstacle 1: $\mathfrak{b}_1$ =36mm, $\mathfrak{a}_1$ =107mm; Obstacle 2:$\mathfrak{b}_2 = 53mm, \mathfrak{a}_2 = 75mm$)

The results also showed unlike TSC strategy, the local stiffness control cannot enable the robot to deal with multiple obstacles, where the robot can easily roll over to one side. This showed that in addition to the stiffness control concept, which both methods take advantage of, position feedback between the joints is also a critical ingredient of an effective pedal wave motion on surfaces with irregularities.

Finally, Supplementary Material C.8 is provided showing the snake robot successfully climbing over two obstacles, where the dimensions and locations of the obstacles were the same as of the experiment shown in Figure 7.9. In this experiment, the snake robot begins the motion 100mm away from the first obstacle and successfully climbs over them without changing the control parameters. Similar to the previous experiments the amplitude of the oscillation of the first joint should be high enough to enable climbing over the obstacles. However, this is more critical in this experiment as low amplitude might cause the robot head module to get stuck in the gap between the obstacles. This suggests that for fully autonomous control of the robot in such challenging environments visual feedback from the camera should be incorporated in the controller.

Overall, the results in this chapter showed that the TSC strategy, which is based on a closed-loop control concept is an effective strategy for achieving pedal wave motion in environments with irregularities. This strategy with the use of the position and torque feedback between the joints enabled the robot to climb over single (Figure 7.6) and multiple obstacles (Figure 7.9) with the same control parameters, which was not possible with open-loop gait based controllers or the local stiffness control strategy. Unlike the open-loop gait based controller, the TSC strategy used the feedback from the measured torque signal to locally modulate the joints motion. This allowed propagation of position feedback signal, which as shown in Figure 7.6, enabled the robot to climb over single obstacle by increasing

the side stability of the robot. Moreover, unlike local stiffness control, where the phase difference between the oscillatory motions of the joint can only be changed manually, the results in Figure 7.8 showed that the TSC strategy can modulate both the phase shift and the amplitude of the oscillatory motion of the joints with the use position and torque feedback signals. Hence, unlike local stiffness control strategy, which was only effective for climbing over single obstacle, TSC strategy proved to the most effective strategy proposed in this thesis enables the robot to achieve effective pedal wave motion in challenging environments, without using a pressure sensor [74] or prior information about the environment [13].

TSC strategy with the discussed characteristics enabled the snake robot to use pedal wave motion for locomotion on surfaces with irregularities. The robot lifted its body part to climb over obstacles with the height of more than 55% of the modules by using on-board sensing devices and successfully traversed over multiple obstacles. These showed the great capabilities of such wheel-less modular snake robot mechanisms for applications, where high adaptability, agility and manoeuvrability is required.

7.5 Summary

In this chapter the extended stiffness controller, named Tail-leading Stiffness Control (TSC) strategy, was presented and tested. The block diagram of this strategy was presented showing that unlike local stiffness strategy, in the TSC strategy there is a position feedback between the consecutive joints, which allows the measured position signals to be propagated along the body. A simulation based analysis of the TSC strategy was also conducted and a detailed description of the fundamentals of this method was provided. Experimentation on the snake robot was also conducted, which showed that unlike open-loop controller based

on gait pattern (4.38), the TSC strategy enables the robot to climb over an obstacle with the height of more than 55% of the diameters of the robot joints. Experimentation in an environment with multiple obstacles were also conducted, which showed that the snake robot with local stiffness control cannot climb over two obstacles. However, TSC strategy with the same parameters but with torque and position feedback enables the robot to effectively move forward in this environment. Overall, the TSC strategy was shown to be an effective method enabling the snake robot with SEAs to climb over single and multiple obstacles.

8
CONCLUSIONS AND RECOMMENDED FUTURE RESEARCH WORKs

8.1 Introduction

In this thesis, design, modelling and control of a modular, wheel-less snake-like robot with SEAs for effective pedal wave locomotion on surfaces with irregularities were studied. The presented materials in this work can be categorized into three major topics as follows:

- The design and development of a cost-effective modular snake robot with torque measurement mechanism (SEA) for reliable and robust environmental sensing.

- Dynamical modelling of modular 2D snake robots with SEAs in the vertical plane for the simulation of pedal wave motion on surfaces with irregularities.
- Control design based on torque and position feedback for achieving effective pedal wave locomotion on surfaces with irregularities.

8.2 Conclusions

As the result of the research conducted on design, modelling and control of the modular snake robots with SEAs, the following conclusions can be drawn:

(i) A Polyurethane-based elastic element was designed and attached between the servo motor and the load to turn the servo motor into a SEA. Calibration results showed that the proposed design manufactured with a water-jet cutter allows measurement of a maximum applied torque of $0.8\,N.m$ with the resolution of $0.01\,N.m$, where the stiffness of the element obtained to be $1.74\,N.m.rad^{-1}$.

(ii) Using a cost-effective 3D printer with ABS as the raw material is an effective methodology for manufacturing a modular snake robot with SEAs, enabling the manufacture of a six-link robot with the overall weight of 956 g and a single module cost of 37 USD.

(iii) The designed snake robot with 3D printed modules and the Polyurethane based elastic element attached between the joints and the servo motors can generate snake-like pedal wave motion (rectilinear motion) on smooth

surfaces with $A = \frac{\pi}{6}\ rad,\ \omega = \pi\ rad.s^{-1}$ and $\phi = \frac{-2\pi}{5}\ rad$ based on the gait pattern (4.38). This showed that the robot can successfully lift its body and push against the ground to move forward with the average velocity of 2.8 $cm.s^{-1}$, which demonstrated the effectiveness of the design.

(iv) The Euler-Lagrange method was used to obtain the equations of motion of the designed snake robot with SEAs. Simulation results showed that the proposed methodology, with Kelvin-Voigt contact model, is an effective approach enable successful simulation of the pedal wave motion of the snake robot. The results showed that the correlation coefficient, R, between the torque signals obtained from the simulation and experimentation is 0.8336, verifying the reliability of the developed dynamical model.

(v) The effect of changing friction on the pedal wave motion of the snake robot was investigated, which supported by the experimentation results, showed that the forward velocity of the pedal wave motion of the snake robot on a surface with $\mu_C = 0.82$ is at least 13.7% higher than the surface with $\mu_C = 0.40$. This result showed that the robot average speed is positively correlated with the friction coefficient of the surface, where the maximum possible speed will be limited due to other factors, such as the length of the links and the maximum motor output torque.

(vi) The effect of the parameters of (4.38) on the forward speed of the robot was investigated. The comparison between the simulation and experimental results showed that the average velocity of the robot predicted by the simulation model is close to the experimentation results with some expected

error, as the maximum error obtained to be 38.7% and the average error calculated to be 22.2%. From the results, it could be seen that increasing the amplitude of the wave, the speed of the robot increases. The results suggested that the pedal wave motion can be viewed as the motion of a wheeled mobile robot along a straight line, where the number of wheels depends on ϕ, the radius of wheels depends on A and the rotational velocity of the wheels depends on ω.

(vii) Local stiffness control strategy, with the use of an admittance controller was designed and implemented, and its effect was studied in a single joint of the robot, which showed that by changing the stiffness, the trajectory of the joint can be changed in response to external forces. The proposed controller enabled the robot to successfully climb over an obstacle with the height of 55% of the diameter of snake robot modules, which was not possible with the open loop controller due to rolling over to one side. This showed that joint stiffness control is indeed an effective strategy for generating pedal wave motion on surfaces with irregularities.

(viii) Tail-Leading Stiffness Control strategy (TSC), was proposed and implemented on the simulated snake robot. The proposed controller enabled the position feedback signal measured at each joint to be propagated along the snake robot body. Simulation results showed that TSC strategy with given parameters as Table 7.1, enables the robot to generate 25.6% faster pedal wave motion compared to the open-loop controller based on gait pattern (4.38), showing the effectiveness of the proposed controller.

(ix) The TSC strategy with given parameters in Table 7.1, was implemented on the physical snake robot, which showed that the robot can successfully climb over a single obstacle with the given dimensions located 100 mm away from the joint 5 (head module) with the use of the TSC strategy, which was not possible with the use of the open-loop gait based controller due to the robot rolling to one side. Moreover, experimental results showed that the adaptability of the TSC strategy stems from the position feedback between the consecutive joints combined with the stiffness control strategy as the TSC strategy with $K_\tau = 0$ also enabled the robot to climb over a single obstacle but failed on a surface with multiple obstacles similar to the local stiffness strategy.

(x) From the experimentation and simulation results presented in Chapter 7, it could be concluded that TSC strategy with position and torque feedback is an effective strategy for achieving pedal wave motion in environments with irregularities. The results showed that, this strategy with the use of position feedback between neighbouring joints and the stiffness control strategy increases the side stability of the robot, therefore enables the robot to climb over multiple obstacles, which was not possible with open-loop gait based controllers and local stiffness strategy presented in Chapter 6.

(xi) Overall, the presented thesis expanded the body of research on modular snake robots for locomotion on surfaces with irregularities (Appendix D gives the list of publications). The presented cost-effective snake robot design enabled to examine adaptive control strategies on uneven terrain. The

novel dynamical model allowed modelling the snake robot on uneven surfaces provided valuable insight about pedal wave motion on surfaces with irregularities. The closed-loop motion generation strategy based on position and torque feedback provided valuable information regarding adaptive snake locomotion. Consequently, these proved the great capabilities of wheel-less modular snake robot mechanisms for applications, in which high adaptability, agility and manoeuvrability is required.

8.3 Future Work Suggestions

(i) The time required to assemble each module of the snake robot developed with the 3D printer was high, which made maintenance of the robot very time consuming. Design and development of a robust, easy to maintain modular snake robot can be considered as a valuable contribution to the field. Moreover, design of a modular snake robot allowing to easy change of the configuration of the robot to generate various 2D and 3D motions is another interesting future research path.

(ii) The proposed dynamical model (4.35) allowed simulation of the pedal wave motion of the snake robot with the use of Kelvin-Voigt contact model. Such a modelling framework can easily be used to model snake-like locomotion inside a pipe, where the reaction force from the environment is the main propulsive force. Moreover, the proposed dynamical model can be extended to model 3D snake-like locomotion patterns, such as sidewinding, which has a same locomotion mechanism as pedal wave motion [78]. These models can

also be used for the design, motion optimization and investigation of environmental factors, such as friction on the robot motion.

(iii) In the simulation environment, only $2N + 1$ points (the centre of mass of the links, robot joints, tip of the head and the tail) on the robot body were checked at each time step to determine the contact points and calculate the external forces. In environments with sharp edged obstacles, there is a high possibility that the links touch the obstacle at the points other than these $2N + 1$ points. This problem can be addressed by considering more candidate contact points to be checked at each time step, which increases the computation burden of the simulation model in return. Further research can be conducted to develop more efficient collision detection methods (See [117] for more details about the collision detection problem in simulation environments).

(iv) Although the joint compliance proved to be an effective strategy for climbing over the stair type obstacle, in real world applications, one can consider varying the joint stiffness to increase the stiffness of the joint on smooth terrain for higher forward speed and decrease the stiffness to achieve higher adaptability based on visual feedback or other environmental information. Development of a new method to actively control the stiffness control the stiffness of the joint while the robot is in motion could be a promising research direction to follow.

(v) The proposed controllers (TSC strategy and the local stiffness control) in this thesis were designed based on the torque feedback measured by the elastic element and the joint angle encoders. More research on the effect of

incorporation of additional sensory information into the proposed controller can be conducted. Such sensory systems, such as IMUs [68], tactile sensors [118] and cameras [16] can gather more information from the environment to achieve more agile pedal wave motion. For example, in case the amplitude of the wave in the local stiffness control is not high enough to enable the robot to climb over the obstacle, visual feedback from the head module camera should be combined with the presented method to increase the amplitude of the wave if necessary.

(vi) The results in chapter 7 showed that the robot shows some level of adaptability even without a torque feedback (i.e. $K_t = 0$). Further research to investigate adaptive locomotion strategies with only position feedback could be an interesting research path leading to design and development of less complicated but still effective control strategies.

(vii) The provided results in this thesis were obtained when considering the obstacles with its surface parallel to the ground. More research can be conducted while considering more complex environments, where the obstacles are placed with some kind of inclination: both on the direction of the movement (climbing or descending) and in the perpendicular direction (falling to the right or to the left) to further investigate the effectiveness of the proposed controller in such environments.

APPENDIX A

A modular snake robot with N identical links and $N-1$ actuators with the same gear ratio of n attached in series with a spring to the corresponding link, can be illustrated as shown in Figure 4.1. Considering that θ_i^l and θ_j^r are the absolute link and rotor angles, respectively, $\alpha_j = \theta_j^l - \theta_{j+1}^l$ is the angle between the consecutive links j and $j+1$, $\beta_j = \theta_j^l - \theta_j^r$ is the j^{th} rotor angle relative to its stator reflected through the link side, $[x_i^l, z_i^l]^{\mathrm{T}}$ and $[x_j^r, z_j^r]^{\mathrm{T}}$ are the position of the centre of mass of link l_i and rotor r_j in the global coordinate frame, respectively and $[p_x, p_z]^{\mathrm{T}}$ denotes the centre of mass of the robot, the equations of motion of the robot in vertical plane can be obtained as follows:

$$\begin{bmatrix} \mathbb{M}(\boldsymbol{q_1}) + \mathbb{S}_1 & \mathbb{S}_2 \\ \mathbb{S}_2^{\mathrm{T}} & \mathbb{S}_3 \end{bmatrix} \ddot{\boldsymbol{q}} + \begin{bmatrix} \mathbb{C}(\boldsymbol{q_1}, \dot{\boldsymbol{q}}_1) \\ \boldsymbol{0} \end{bmatrix} + \boldsymbol{\mathcal{G}} + K_E \boldsymbol{q} - \boldsymbol{Q}^c = \mathbb{B} \tag{A.1}$$

where $\mathbb{M}(\boldsymbol{q_1})_{(N+2)\times(N+2)}$ is a positive definite inertia matrix, $\mathbb{C}(\boldsymbol{q_1}, \dot{\boldsymbol{q}}_1)_{(N+2)}$ is the vector of Coriolis and centrifugal terms, $\boldsymbol{\mathcal{G}}$ is a column vector of gravitational forces, $\mathbb{B} = \begin{bmatrix} \boldsymbol{0}_{1\times(N+2)} & | & \boldsymbol{U}^{\mathrm{T}} \end{bmatrix}^{\mathrm{T}}$, $\boldsymbol{U}$ is the column vector of $N-1$ control inputs (motor torques), $\boldsymbol{Q}^c$ is the vector of non-conservative contact forces, $\boldsymbol{q}_1 = [\alpha_1, \dots, \alpha_{N-1}, \theta_N^l, p_x, p_z]^{\mathrm{T}}$ and

$$\mathbb{M}(\boldsymbol{q_1}) = M^L(\boldsymbol{q_1}) + M^R(\boldsymbol{q_1}) \tag{A.2}$$

where

$$M^L(\boldsymbol{q_1}) = \left(\mathcal{B}_1^l + \mathcal{A}^l \mathcal{S}_\theta \mathcal{C}\right)^T \mathcal{M}^l \left(\mathcal{B}_1^l + \mathcal{A}^l \mathcal{S}_\theta \mathcal{C}\right) + \left(\mathcal{B}_2^l - \mathcal{A}^l \mathcal{C}_\theta \mathcal{C}\right)^T \mathcal{M}^l \left(\mathcal{B}_2^l - \mathcal{A}^l \mathcal{C}_\theta \mathcal{C}\right) + \mathcal{C}^T \mathcal{J}^l \mathcal{C}$$

$$M^R(\boldsymbol{q}) = (\mathcal{B}_1^r + \mathcal{A}^r \mathcal{S}_\theta \mathcal{C})^T \mathcal{M}^r (\mathcal{B}_1^r + \mathcal{A}^r \mathcal{S}_\theta \mathcal{C}) + (\mathcal{B}_2^r - \mathcal{A}^r \mathcal{C}_\theta \mathcal{C})^T \mathcal{M}^r (\mathcal{B}_2^r - \mathcal{A}^r \mathcal{C}_\theta \mathcal{C})$$

Moreover, the matrix of centripetal forces $\mathbb{C}(\boldsymbol{q_1}, \dot{\boldsymbol{q}}_\mathbf{1})$ can be found as below :

$$\mathbb{C}(\boldsymbol{q_1}, \dot{\boldsymbol{q}}_\mathbf{1}) = \boldsymbol{C}^R(\boldsymbol{q_1}, \dot{\boldsymbol{q}}_\mathbf{1}) + \boldsymbol{C}^L(\boldsymbol{q_1}, \dot{\boldsymbol{q}}_\mathbf{1}) \tag{A.3}$$

where

$$\boldsymbol{C}^L(\boldsymbol{q}, \dot{\boldsymbol{q}}) = \boldsymbol{CC}\left(\mathcal{B}_1^l, \mathcal{B}_2^l, \mathcal{A}^l, \mathcal{M}^l, \boldsymbol{q_1}, \dot{\boldsymbol{q}}_\mathbf{1}\right)$$

$$\boldsymbol{C}^R(\boldsymbol{q}, \dot{\boldsymbol{q}}) = \boldsymbol{CC}(\mathcal{B}_1^r, \mathcal{B}_2^r, \mathcal{A}^r, \mathcal{M}^r, \boldsymbol{q_1}, \dot{\boldsymbol{q}}_\mathbf{1})$$

and

$$\boldsymbol{CC}\left(\mathcal{B}_1^l, \mathcal{B}_2^l, \mathcal{A}^l, \boldsymbol{q_1}, \dot{\boldsymbol{q}}_\mathbf{1}\right) =$$

$$\begin{aligned}
&\Big\{\mathcal{B}_1^{l^T}\mathcal{M}^l\mathcal{A}^l\mathcal{C}_\theta diag\left(\dot{\boldsymbol{\theta}}^l\right)\mathcal{C} + \mathcal{C}^T\mathcal{C}_\theta diag\left(\dot{\boldsymbol{\theta}}^l\right)\mathcal{A}^{l^T}\mathcal{M}^l\mathcal{B}_1^l \\
&\quad + \mathcal{C}^T\mathcal{S}_\theta\mathcal{A}^{l^T}\mathcal{M}^l\mathcal{A}^l\mathcal{C}_\theta diag\left(\dot{\boldsymbol{\theta}}^l\right)\mathcal{C} \\
&\quad + \mathcal{C}^T\mathcal{C}_\theta diag\left(\dot{\boldsymbol{\theta}}^l\right)\mathcal{A}^{l^T}\mathcal{M}^l\mathcal{A}^l\mathcal{S}_\theta\mathcal{C} + \mathcal{B}_2^{l^T}\mathcal{M}^l\mathcal{A}^l\mathcal{S}_\theta diag\left(\dot{\boldsymbol{\theta}}^l\right)\mathcal{C} \\
&\quad + \mathcal{C}^T\mathcal{S}_\theta diag\left(\dot{\boldsymbol{\theta}}^l\right)\mathcal{A}^{l^T}\mathcal{M}^l\mathcal{B}_2^l - \mathcal{C}^T\mathcal{C}_\theta\mathcal{A}^{l^T}\mathcal{M}^l\mathcal{A}^l\mathcal{S}_\theta diag\left(\dot{\boldsymbol{\theta}}^l\right)\mathcal{C} \\
&\quad - \mathcal{C}^T\mathcal{S}_\theta diag(\dot{\boldsymbol{\theta}}^l)\mathcal{A}^{l^T}\mathcal{M}^l\mathcal{A}^l\mathcal{C}_\theta\mathcal{C}\Big\}\dot{\boldsymbol{q}}_\mathbf{1}
\end{aligned}$$

$$+\begin{bmatrix} \dot{\boldsymbol{q}}_\mathbf{1}^T\boldsymbol{B_1}^T\boldsymbol{\mathcal{M}}^l\boldsymbol{\mathcal{A}}^l\boldsymbol{\mathcal{C}}_\theta\boldsymbol{diag}(\boldsymbol{C_1})\dot{\boldsymbol{\theta}}^l \\ \dot{\boldsymbol{q}}_\mathbf{1}^T\boldsymbol{B_1}^T\boldsymbol{\mathcal{M}}^l\boldsymbol{\mathcal{A}}^l\boldsymbol{\mathcal{C}}_\theta\boldsymbol{diag}(\boldsymbol{C_2})\dot{\boldsymbol{\theta}}^l \\ \vdots \\ \dot{\boldsymbol{q}}_\mathbf{1}^T\boldsymbol{B_1}^T\boldsymbol{\mathcal{M}}^l\boldsymbol{\mathcal{A}}^l\boldsymbol{\mathcal{C}}_\theta\boldsymbol{diag}(\boldsymbol{C_{2N+1}})\dot{\boldsymbol{\theta}}^l \end{bmatrix} + \begin{bmatrix} \dot{\boldsymbol{\theta}}^{l^T}\boldsymbol{\mathcal{C}}_\theta\boldsymbol{diag}(\boldsymbol{C_1})\boldsymbol{\mathcal{A}}^{l^T}\boldsymbol{\mathcal{M}}^l\boldsymbol{\mathcal{B}}_\mathbf{1}^l\dot{\boldsymbol{q}}_\mathbf{1} \\ \dot{\boldsymbol{\theta}}^{l^T}\boldsymbol{\mathcal{C}}_\theta\boldsymbol{diag}(\boldsymbol{C_2})\boldsymbol{\mathcal{A}}^{l^T}\boldsymbol{\mathcal{M}}^l\boldsymbol{\mathcal{B}}_\mathbf{1}^l\dot{\boldsymbol{q}}_\mathbf{1} \\ \vdots \\ \dot{\boldsymbol{\theta}}^{l^T}\boldsymbol{\mathcal{C}}_\theta\boldsymbol{diag}(\boldsymbol{C_{2N+1}})\boldsymbol{\mathcal{A}}^{l^T}\boldsymbol{\mathcal{M}}^l\boldsymbol{\mathcal{B}}_\mathbf{1}^l\dot{\boldsymbol{q}}_\mathbf{1} \end{bmatrix}$$

$$+\begin{bmatrix} \dot{\boldsymbol{\theta}}^{l^T}\left(\boldsymbol{\mathcal{C}}_\theta\boldsymbol{diag}(\boldsymbol{C_1})\boldsymbol{\mathcal{A}}^{l^T}\boldsymbol{\mathcal{M}}^l\boldsymbol{\mathcal{A}}^l\boldsymbol{\mathcal{S}}_\theta + \boldsymbol{\mathcal{S}}_\theta\boldsymbol{\mathcal{A}}^{l^T}\boldsymbol{\mathcal{M}}^l\boldsymbol{\mathcal{A}}^l\boldsymbol{\mathcal{C}}_\theta\boldsymbol{diag}(\boldsymbol{C_1})\right)\dot{\boldsymbol{\theta}}^l \\ \dot{\boldsymbol{\theta}}^{l^T}\left(\boldsymbol{\mathcal{C}}_\theta\boldsymbol{diag}(\boldsymbol{C_2})\boldsymbol{\mathcal{A}}^{l^T}\boldsymbol{\mathcal{M}}^l\boldsymbol{\mathcal{A}}^l\boldsymbol{\mathcal{S}}_\theta + \boldsymbol{\mathcal{S}}_\theta\boldsymbol{\mathcal{A}}^{l^T}\boldsymbol{\mathcal{M}}^l\boldsymbol{\mathcal{A}}^l\boldsymbol{\mathcal{C}}_\theta\boldsymbol{diag}(\boldsymbol{C_2})\right)\dot{\boldsymbol{\theta}}^l \\ \vdots \\ \dot{\boldsymbol{\theta}}^{l^T}\left(\boldsymbol{\mathcal{C}}_\theta\boldsymbol{diag}(\boldsymbol{C_{2N+1}})\boldsymbol{\mathcal{A}}^{l^T}\boldsymbol{\mathcal{M}}^l\boldsymbol{\mathcal{A}}^l\boldsymbol{\mathcal{S}}_\theta + \boldsymbol{\mathcal{S}}_\theta\boldsymbol{\mathcal{A}}^{l^T}\boldsymbol{\mathcal{M}}^l\boldsymbol{\mathcal{A}}^l\boldsymbol{\mathcal{C}}_\theta\boldsymbol{diag}(\boldsymbol{C_{2N+1}})\right)\dot{\boldsymbol{\theta}}^l \end{bmatrix}$$

APPENDIX B

The correlation coefficient, R, indicates the similarity between two signals. For two signals X and Y having the same number of samples n, the correlation coefficient, R can be calculated as follows [119]:

$$R = \frac{n(\sum XY) - (\sum X)(\sum Y)}{\sqrt{[n\sum X^2 - (\sum X)^2][n\sum Y^2 - (\sum Y)^2]}}, \quad \text{(B.1)}$$

which is always bounded between -1 to +1.

The correlation coefficient of +1 means that X and Y have a very strong positive relationship (i.e., X=Y) and correlation coefficient of -1 means that X and Y have a very strong negative relationship (i.e., X=-Y). Hence, if the value of R is calculated to be close to +1, this can be interpreted as an indication of similarity between the tested signals.

APPENDIX C

The supplementary materials for this thesis are listed as follows:

Supplementary Material C.1: Shows the simulated and physical snake robot progression with pedal wave motion with $A = \frac{\pi}{6} rad, \omega = \pi\ rad.s^{-1}$ and $\phi = \frac{-2\pi}{5}\ rad$. This video can be found in this address: https://youtu.be/9e4waEODcQY

Supplementary Material C.2: The effect of stiffness control strategy on a single joint of the robot, with $K_d = K/5$. This video can be found in this address: https://youtu.be/Z420uPWq0dA

Supplementary Material C.3: The snake robot climbing over a single obstacle (also shown in Figure 6.4) employing open-loop gait based control and the local stiffness control strategy with $A = \frac{\pi}{4} rad, \omega = \pi\ rad.s^{-1}, \phi = \frac{-2\pi}{5} rad$ and $K_d = \frac{\mathrm{K}}{6}$. This video can be found in this address: https://youtu.be/F9I4eDMvhfA

Supplementary Material C.4: Showing the snake robot rolls over to one side when climbing over two obstacles with the use of local stiffness control strategy with $A = \frac{\pi}{6} rad$, $\omega = \pi\ rad.s^{-1}$, $\phi = \frac{-2\pi}{5}$ and $K_d = \frac{\mathrm{K}}{6}$. This video can be found in this address: https://youtu.be/GgbktXboJEY

Supplementary Material C.5: Showing the effect of the manually applied external force which propagates along the snake body when TSC strategy with $A = 0\ rad$, $M_d = 1\ N.m.s^2.rad^{-1}, D_d = 10\ N.m.s.rad^{-1}$, $K_d = 17.5\ N.m.rad^{-1}$ and $K_\tau = 6$ is

implemented on the snake robot. This video can be found in this address: https://youtu.be/XVfNx64xEIc

Supplementary Material C.6: Showing the snake robot climbing over a single obstacle with the height of 36mm and width 107mm located 100mm away from the joint 5 (head module) with the use of TSC strategy with $A = \frac{\pi}{6} rad$, $\omega = \pi\, rad.s^{-1}$, $M_d = 1\ N.m.s^2.rad^{-1}$, $D_d = 10\ N.m.s.rad^{-1}$, $K_d = 17.5\ N.m.rad^{-1}$ and $K_\tau = 6$, the open-loop gait based control (4.38) with $A = \frac{\pi}{6} rad$, $\omega = \pi\, rad.s^{-1}$, $\phi = \frac{-2\pi}{5} rad$ and the local stiffness control strategy with $A = \frac{\pi}{6} rad$, $\omega = \pi\, rad.s^{-1}$, $\phi = \frac{-2\pi}{5} rad$, $\frac{K - K_d}{K_d} = 6$. This video can be found in this address: https://youtu.be/CZZDmO6MFhc

Supplementary Material C.7: Showing the snake robot climbing over multiple obstacles with the use of TSC strategy with $A = \frac{\pi}{6} rad$, $\omega = \pi\, rad.s^{-1}$, $M_d = 1N.m.s^2.rad^{-1}$, $D_d = 10N.m.s.rad^{-1}$, $K_d = 17.5N.m.rad^{-1}$ and $K_\tau = 0$ and $K_\tau = 6$ and the local stiffness control strategy with $A = \frac{\pi}{6} rad$, $\omega = \pi\, rad.s^{-1}$, $\phi = \frac{-2\pi}{5} rad$, $\frac{K - K_d}{K_d} = 6$. This video can be found in this address: https://youtu.be/7t-13E1tvw8

Supplementary Material C.8: Showing the snake robot climbing over two obstacles staring 100mm before the first obstacle with the use of TSC strategy with $A = \frac{\pi}{6} rad$, $\omega = \pi\, rad.s^{-1}$, $M_d = 1N.m.s^2.rad^{-1}$, $D_d = 10N.m.s.rad^{-1}$, $K_d = 17.5N.m.rad^{-1}$, $K_\tau = 6$ video can be found in this address: https://youtu.be/DWzO-DS5Jp0

APPENDIX D

The following articles are published as the result of the research work presented in this thesis:

Journal Articles:

Koopaee, M. J., Classens, K., Pretty, C., & Chen, X. (2019). Dynamical Modelling and Control of Modular Snake Robots with Series Elastic Actuators for Pedal Wave Locomotion on Uneven Terrain. *Journal of Mechanical Design*, (Accepted).

Koopaee, M. J., Bal, S., Pretty, C., & Chen, X. (2019). Design and Development of a Wheel-less Snake Robot with Active Stiffness Control for Adaptive Pedal Wave Locomotion. *Journal of Bionic Engineering*, 16(4), 593-607.

Book Chapter:

Koopaee, M. J., Gilani, C., Scott, C., & Chen, X. (2018). Bio-Inspired Snake Robots: Design, Modelling, and Control. *In Handbook of Research on Biomimetics and Biomedical Robotics* (pp. 246-275). IGI Global.

Conference Papers:

Koopaee, M. J., Classens, K., Pretty, C., & Chen, X. (2019). Dynamical Modelling and Control of Snake-like Motion in Vertical Plane for Locomotion in Unstructured Environments. *The ASME 2019 International Design Engineering Technical Conferences & Computers and Information in Engineering Conference (IDETC/CIE 2019)*, Anaheim, California, USA, (Accepted).

Koopaee, M. J., Van Huijgevoort, B., Pretty, C., & Chen, X. (2018). Parameters tuning of snake robots sidewinding gait using Bayesian optimization. *The IEEE* 2018 *International Conference on Control, Automation and Robotics (ICCAR 2019)*, Auckland, New Zealand, pp. 43-49.

References

[1] G. Campion, G. Bastin, and B. Dandrea-Novel, “Structural properties and classification of kinematic and dynamic models of wheeled mobile robots,” *IEEE Trans. Robot. Autom.*, vol. 12, no. 1, pp. 47–62, 1996.

[2] N. Chakraborty and A. Ghosal, “Kinematics of wheeled mobile robots on uneven terrain,” *Mech. Mach. Theory*, vol. 39, no. 12, pp. 1273–1287, 2004.

[3] T. Buschmann and B. Trimmer, “Bio-inspired Robot Locomotion,” in *Neurobiology of Motor Control*, , John Wiley & Sons, Inc., Hoboken, NJ, USA, pp. 443–472, 2017.

[4] S. Hirose and H. Yamada, “Snake-like robots,” *IEEE Robot. Autom. Mag.*, vol. 16, no. 1, pp. 88–98, 2009.

[5] T. Baba, Y. Kameyama, T. Kamegawa, and A. Gofuku, “A snake robot propelling inside of a pipe with helical rolling motion,” In Proc. 2010 SICE Annual Conference, 18-21 Aug, Taipei, Taiwan, pp. 2319–2325, 2010.

[6] E. Rohmer, S. P. N. Singh, and M. Freese, “V-REP: A versatile and scalable robot simulation framework,” In Proc. 2013 IEEE/RSJ International Conference on Intelligent Robots and Systems, 3-7 Nov, Tokyo, Japan, pp. 1321–1326, 2013.

[7] S. Chen, X. Li, K. Lu, Y. Fang, and W. Wang, “Gait, Stability and Movement of Snake-Like Robots,” *Int. J. Adv. Robot. Syst.*, vol. 9, no. 5, p. 214, 2012.

[8] S. W. Gart, T. W. Mitchel, and C. Li, “Snakes partition their body to traverse large steps stably,” *J. Exp. Biol.*, p. jeb.185991, 2019.

[9] G. S. Chirikjian and J. W. Burdick, “The Kinematics of Hyper-Redundant Robot Locomotion,” *IEEE Trans. Robot. Autom.*, vol. 11, no. 6, pp. 781-793, 1995.

[10] R. Irani, R. Bauer, L. North, M. Nicholson, D. Nolan, and B. West, “Analysis Of Joint Failures On The Lateral Undulation Gait Of A Robotic Snake,” *Trans. Can. Soc. Mech. Eng.*, vol. 39, no. 2, pp. 253–268, 2015.

[11] D. Rollinson and H. Choset, “Pipe Network Locomotion with a Snake Robot,” *J. F. Robot.*, vol. 33, no. 3, pp. 322–336, 2016.

[12] P. Liljebäck, K. Y. Pettersen, O. Stavdahl, and J. T. Gravdahl, "Experimental investigation of obstacle-aided locomotion with a snake robot," *IEEE Trans. Robot.*, vol. 27, no. 4, pp. 792-800, 2011

[13] H. Yamada and S. Hirose, "Steering of pedal wave of a snake-like robot by superposition of curvatures," In Proc. 2010 IEEE/RSJ International Conference on Intelligent Robots and Systems, 18-22 Oct, Taipei, Taiwan, pp. 419–424, 2010.

[14] S. Hirose, *Biologically inspired robots*. Oxford Univ. Press, NewYork, USA, 1993.

[15] A. A. Transeth, R. I. Leine, C. Glocker, K. Y. Pettersen, and P. Liljebäck, "Snake robot obstacle-aided locomotion: Modeling, simulations, and experiments," *IEEE Trans. Robot.*, vol. 24, no. 1, pp. 88-104, 2008.

[16] M. Mutlu, K. Melo, M. Vespignani, A. Bernardino, and A. J. Ijspeert, "Where to place cameras on a snake robot: Focus on camera trajectory and motion blur," In Proc. 2016 IEEE International Symposium on Safety, Security, and Rescue Robotics, 18-20 Oct. West Lafayette, IN, USA, pp. 1-8, 2016.

[17] P. Liljebäck, K. Y. Pettersen, O. Stavdahl, and J. T. Gravdahl, *Snake robots: modelling, mechatronics, and control*. Springer London Heidelberg, New York, USA, 2012.

[18] A. A. Transeth, R. I. Leine, C. Glocker, and K. Y. Pettersen, "3-D Snake Robot Motion: Nonsmooth Modeling, Simulations, and Experiments," *IEEE Trans. Robot.*, vol. 24, no. 2, pp. 361–376, 2008.

[19] R. Ariizumi and F. Matsuno, "Dynamical analysis of sidewinding locomotion by a snake-like robot," In Proc. 2013 IEEE International Conference on Robotics and Automation, 6-10 May, Karlsruhe, Germany, pp. 5149–5154, 2013.

[20] M. A. J. Koopaee and V. J. Majd, "Controller design with constraint on control input and output for T-S fuzzy systems with nonlinear local model," In Proc. 2015 23rd Iranian Conference on Electrical Engineering, 10-14 May, Tehran, Iran, pp. 876–881, 2015.

[21] M. Maggiore and L. Consolini, "Virtual Holonomic Constraints for Euler-Lagrange

Systems," *IEEE Trans. Automat. Contr.*, vol. 58, no. 4, pp. 1001–1008, 2013.

[22] S. Takaoka, H. Yamada, and S. Hirose, "Snake-like active wheel robot ACM-R4.1 with joint torque sensor and limiter," In Proc. 2011 IEEE/RSJ International Conference on Intelligent Robots and Systems, 25-30 Sept, San Francisco, CA, USA, pp. 1081–1086, 2011.

[23] P. Liljebäck, Ø. Stavdahl, K. Y. Pettersen, and J. T. Gravdahl, "A modular and waterproof snake robot joint mechanism with a novel force/torque sensor," In Proc. 2012 IEEE/RSJ International Conference on Intelligent Robots and Systems, 7-12 Oct, Vila Moura, Portugal, pp. 4898–4905, 2012.

[24] T. Sato, T. Kano, and A. Ishiguro, "A decentralized control scheme for an effective coordination of phasic and tonic control in a snake-like robot," *Bioinspir. Biomim.*, vol. 7, no. 1, p. 016005, 2012.

[25] A. De Luca and W. Book, "Robots with flexible elements," in *Springer Handbook of Robotics*, Springer-Verlag Berlin Heidelberg, Germany, pp. 287–319, 2008.

[26] K. Y. Pettersen, "Snake robots," *Annu. Rev. Control*, vol. 44, pp. 19–44, 2017.

[27] A. E. Kerdok, A. A. Biewener, T. A. McMahon, P. G. Weyand, and H. M. Herr, "Energetics and mechanics of human running on surfaces of different stiffnesses," *J. Appl. Physiol.*, vol. 92, no. 2, pp. 469–478, 2002.

[28] F. Zhou, L. Kang, and X.-H. Wang, "JumpDetector: An automated monitoring equipment for the locomotion of jumping insects," *Insect Sci.*, vol. 1, pp. 1-12, 2019.

[29] J. H. Byrne, *The Oxford Handbook of Invertebrate Neurobiology*. Oxford University Press, New York, NY 10016, USA, 2017.

[30] P. Schiebel et al., "Mechanics of undulatory swimming on the surface of granular matter.," In Proc. 71st Annual Meeting of the APS Division of Fluid Dynamics, Bulletin of the American Physical Society, 18-20 Nov, Atlanta, Georgia, USA, 2018.

[31] H. Date and Y. Takita, "Adaptive locomotion of a snake like robot based on curvature derivatives," In Proc. 2007 IEEE/RSJ International Conference on Intelligent Robots and Systems (IROS), 29 Oct.-2 Nov, San Diego, USA, pp. 3554–3559, 2007.

[32] M. Walton, “The Energetic cost of Limbless Locomotion,” *Science*, vol. 249, no. 4968, pp. 524-527, 1990.

[33] H. F. Hutchinson, “About Snakes,” *Nature*, vol. 20, no. 518, pp. 528–530, 1879.

[34] A. D. Fokker, “De Voortbeweging Der Slangen,” *Phisica*, vol. 7, no. 65, 1927.

[35] W. Mosauer, “On the locomotion of snakes,” *Science*, vol. 76, no. 1982, pp. 583–585, 1932..

[36] A. T. Jones, “The gliding of a snake,” *Physics*, vol. 4, no. 4, pp. 164–165, 1933.

[37] J. GRAY, “The Mechanism of Locomotion In Snakes,” *J. Exp. Biol.*, vol. 23, no. 2, pp. 101-120, 1946.

[38] C. Gans, “Terrestrial locomotion without limbs,” *Am. Zool.*, vol. 2, no. 2, pp. 167–182, 1962.

[39] A. A. Transeth, K. Y. Pettersen, and P. Liljebäck, “A survey on snake robot modeling and locomotion,” *Robotica*, vol. 27, no. 7, pp. 999–1015, 2009.

[40] B. C. Jayne, M. A. Riley, "Scaling of the axial morphology and gap-bridging ability of the brown tree snake, Boiga irregularis." *Journal of Experimental Biology* vol. 210, no, pp. 71148-1160, 2008.

[41] E. Rezapour, P. Liljebäck, "Path following control of a planar snake robot with an exponentially stabilizing joint control law." *IFAC Proceedings* vol. 46, no 10, pp. 28-35, 2013.

[42] F. Dal Corso, D. Misseroni, N. M. Pugno, A. B. Movchan, N. V Movchan, and D. Bigoni, “Serpentine locomotion through elastic energy release,” *J. R. Soc. Interface*, vol. 14, no. 130, p. 20170055, 2017.

[43] D. L. Hu, J. Nirody, T. Scott, and M. J. Shelley, “The mechanics of slithering locomotion,” *Proc. Natl. Acad. Sci.*, vol. 106, no. 25, 2009.

[44] H. Marvi and D. L. Hu, “Friction enhancement in concertina locomotion of snakes,” *J. R. Soc. Interface*, vol. 9, no. 76, pp. 3067-3080, 2012.

[45] W. Mosauer, “A note on the sidewinding locomotion of snakes,” *Am. Nat.*, vol. 64,

no. 691, pp. 179–183, 1930.

[46] C. M. Bogert, “Rectilinear locomotion in snakes,” *Copeia*, vol. 1947, no. 4, pp. 253–254, 1947.

[47] H. W. Lissmann, “Rectilinear locomotion in a snake (Boa occidentalis),” *J. Exp. Biol.*, vol. 26, no. 4, pp. 368–379, 1950.

[48] H. Marvi, J. Bridges, and D. L. Hu, “Snakes mimic earthworms: Propulsion using rectilinear travelling waves,” *J. R. Soc. Interface*, vol. 10, no. 84, p. 20130188, 2013.

[49] J. Hazel, M. Stone, M. S. Grace, and V. V Tsukruk, “Nanoscale design of snake skin for reptation locomotions via friction anisotropy,” *J. Biomech.*, vol. 32, no. 5, pp. 477–484, 1999.

[50] M. J. Benz, A. E. Kovalev, and S. N. Gorb, “Anisotropic frictional properties in snakes,” In Proc. 2012 SPIE Smart Structures and Materials and Nondestructive Evaluation and Health Monitoring, 4 April, San Diego, California, US, pp. 83390X–3390X, 2012.

[51] P. Cuervo, D. A. Lopez, J. P. Cano, J.C. Sánchez, S. Rudas, H. Estupiñán, A. Toro, and H. A. Abdel-Aal, “Development of low friction snake-inspired deterministic textured surfaces,” *Surf. Topogr. Metrol. Prop.*, vol. 4, no. 2, pp. 24013, 2016.

[52] Z. V Guo and L. Mahadevan, “Limbless undulatory propulsion on land.,” *Proc. Natl. Acad. Sci.*, vol. 105, no. 9, pp. 3179–3184, 2008.

[53] M. Walton, “The Energetic cost of Limbless Locomotion,” *Science*, vol. 249, no. 4968, pp. 524-527, 1990.

[54] S. M. Secor, B. C. Jayne, and A. F. Bennett, “Locomotor performance and energetic cost of sidewinding by the snake Crotalus cerastes,” *J. Exp. Biol.*, vol. 163, no. 1, pp. 1–14, 1992.

[55] S. Bennet, T. McConnell, and S. L. Trubatch, “Quantitative analysis of the speed of snakes as a function of peg spacing,” *J. Exp. Biol.*, vol. 60, no. 1, pp. 161–165, 1974.

[56] B. C. Jayne, “Kinematics of terrestrial snake locomotion,” *Copeia*, vol. 1986, no. 4,

pp. 915–927, 1986.

[57] B. R. Moon and C. Gans, “Kinematics, muscular activity and propulsion in gopher snakes,” *J. Exp. Biol.*, vol. 201, no. 19, pp. 2669–2684, 1998.

[58] H. Marvi *et al.*, “Sidewinding with minimal slip: snake and robot ascent of sandy slopes.,” *Science*, vol. 346, no. 6206, pp. 224–229, 2014.

[59] J. Rossiter and S. Sareh, “Kirigami design and fabrication for biomimetic robotics,” In Proc. 2014 Proceedings of SPIE Smart Structures and Materials and Nondestructive Evaluation and Health Monitoring, 4 April, San Diego, California, US, 2014.

[60] I. D. Walker, “Continuous backbone ‘continuum’ robot manipulators,” *Ism Robot.*, vol. 2013, 2013.

[61] S. Manzoor and Y. Choi, “A unified neural oscillator model for various rhythmic locomotions of snake-like robot,” *Neurocomputing*, vol. 173, no. 3, pp. 1112–1123, 2016.

[62] J.-K. Ryu, N. Y. Chong, B. J. You, and H. I. Christensen, “Locomotion of snake-like robots using adaptive neural oscillators,” *Intell. Serv. Robot.*, vol. 3, no. 1, 2009.

[63] C. Gong, M. J. Travers, X. Fu, and H. Choset, “Extended gait equation for sidewinding,” In Proc. 2013 IEEE International Conference on Robotics and Automation, 6-10 May, Karlsruhe, Germany, pp. 5162–5167, 2013.

[64] M. Nakajima, M. Tanaka, K. Tanaka, and F. Matsuno, “Motion control of a snake robot moving between two non-parallel planes,” *Adv. Robot.*, vol. 32, no. 10, pp. 559–573, 2018.

[65] H. Komura, H. Yamada, and S. Hirose, “Development of snake-like robot ACM-R8 with large and mono-tread wheel,” *Adv. Robot.*, vol. 29, no. 17, pp. 1081–1094, 2015.

[66] J. Borenstein, M. Hansen, and A. Borrell, “The OmniTread OT-4 serpentine robot - Design and performance,” *J. F. Robot.*, vol. 24, no. 7, pp. 601-621, 2007.

[67] P. Liljebäck, K. Y. Pettersen, and Ø. Stavdahl, “A snake robot with a contact force

measurement system for obstacle-aided locomotion," In Proc. 2010 IEEE International Conference on Robotics and Automation, 3-7 May, Anchorage, AK, USA, pp. 683–690, 2010.

[68] D. Rollinson *et al.*, "Design and architecture of a series elastic snake robot," In Proc. 2014 IEEE/RSJ International Conference on Intelligent Robots and Systems, 14-18 Sept, Chicago, IL, USA, 2014.

[69] A. Akbarzadeh and H. Kalani, "Design and Modeling of a Snake Robot Based on Worm-Like Locomotion," *Adv. Robot.*, vol. 26, no. 5–6, pp. 537–560, 2012.

[70] C. Gong, R. L. Hatton, and H. Choset, "Conical sidewinding," In Proc. 2012 IEEE International Conference on Robotics and Automation, 14-18 May, Saint Paul, MN, USA, pp. 4222–4227, 2012.

[71] D. Rollinson, A. Buchan, and H. Choset, "Virtual Chassis for Snake Robots: Definition and Applications," *Adv. Robot.*, vol. 26, no. 17, pp. 2043–2064, 2012.

[72] M. F. Fallon *et al.*, "Continuous humanoid locomotion over uneven terrain using stereo fusion," In Proc. 2015 IEEE-RAS International Conference on Humanoid Robots (Humanoids), 3-5 Nov, Seoul, South Korea, pp. 881–888, 2015.

[73] Z. Y. Bayraktaroglu, "Snake-like locomotion: Experimentations with a biologically inspired wheel-less snake robot," *Mech. Mach. Theory*, vol. 44, no. 3, pp. 591–602, 2009.

[74] T. Kano, Y. Watanabe, F. Satake, and A. Ishiguro, "Decentralized-controlled multi-terrain robot inspired by flatworm locomotion," *Adv. Robot.*, vol. 28, no. 7, pp. 523–531, 2014.

[75] S. Ford, D. Rollinson, A. Willig, and H. Choset, "Online calibration of a compact series elastic actuator," In Proc. 2014 American Control Conference, 4-6 June, Portland, OR, USA, pp. 3329–3334, 2014.

[76] D. Rollinson, K. V. Alwala, N. Zevallos, and H. Choset, "Torque control strategies for snake robots," In Proc. 2014 IEEE/RSJ International Conference on Intelligent Robots and Systems, 14-18 Sept, Chicago, IL, USA, pp. 1093-1099, 2014.

[77] G. S. Chirikjian, "Hyper-redundant manipulator dynamics: A continuum approximation," *Adv. Robot.*, vol. 9, no. 3, pp. 217-243, 1994.

[78] R. Ariizumi and F. Matsuno, "Dynamic Analysis of Three Snake Robot Gaits," *IEEE Trans. Robot.*, vol. 33, no. 5, pp. 1075–1087, 2017.

[79] M. P. Do Carmo, *Differential Geometry of Curves and Surfaces*. Prentice-Hall, Inc., New Jersey, USA, 1976.

[80] R. L. Hatton and H. Choset, "Generating gaits for snake robots by annealed chain fitting and keyframe wave extraction," In Proc. 2009 IEEE/RSJ International Conference on Intelligent Robots and Systems, 10-15 Oct, St. Louis, MO, USA, pp.271-281 2009.

[81] G. S Chirikjian, "Theory and applications of hyper-redundant robotic manipulators, " P.h.D. thesis, California Institute of Technology, Pasadena, California, 1992.

[82] P. Liljebäck, K. Y. Pettersen, O. Stavdahl, and J. T. Gravdahl, "Hybrid Modelling and Control of Obstacle-Aided Snake Robot Locomotion," *IEEE Trans. Robot.*, vol. 26, no. 5, pp. 781-799, 2010.

[83] L. Chen, S. Ma, Y. Wang, B. Li, and D. Duan, "Design and modelling of a snake robot in traveling wave locomotion," *Mech. Mach. Theory*, vol. 42, no. 12, pp. 1632–1642, 2007.

[84] S. Ma, Y. Ohmameuda, and K. Inoue, "Dynamic analysis of 3-dimensional snake robots," In Proc. 2004 IEEE/RSJ International Conference on Intelligent Robots and Systems (IROS), *28 Sept.-2 Oct*, Sendai, Japan, pp. 767–772, 2004.

[85] M. Tesch, K. Lipkin, I. Brown, R. Hatton, A. Peck, J. Rembisz, H. Choset, "Parameterized and Scripted Gaits for Modular Snake Robots," *Adv. Robot.*, vol. 23, no. 9, pp. 1131–1158, 2009.

[86] R. L. Hatton and H. Choset, "Generating gaits for snake robots: Annealed chain fitting and keyframe wave extraction," *Auton. Robots*, vol. 28, no. 3, pp. 271-281, 2010.

[87] S. Hasanzadeh and A. Tootoonchi, "Ground adaptive and optimized locomotion of

snake robot moving with a novel gait," *Auton. Robots,* vol. 28, no. 4, pp. 457–470, 2010.

[88] A. J. Ijspeert, "Central pattern generators for locomotion control in animals and robots: a review," *Neural Netw,* vol. 21, no. 4, pp. 642–653, 2008.

[89] N. M. Nor and S. Ma, "Smooth transition for CPG-based body shape control of a snake-like robot," *Bioinspir. Biomim.*, vol. 9, no. 1, p. 16003, 2014.

[90] X. Wu, "Sensor-driven Neural Controller for Self-adaptive Collision-freeBehavior of a Snake-like Robot," In Proc. 2011 IEEE International Conference on Robotics and Automation, 9-13 May, Shanghai, China, pp. 191-196, 2011.

[91] Z. Y. Bayraktaroglu, F. Butel, V. Pasqui, and P. Blazevic, "Snake-like locomotion: integration of geometry and kineto-statics," *Adv. Robot.,* vol. 14, no. 6, pp. 447–458, 2000.

[92] M. Travers, J. Whitman, and H. Choset, "Shape-based coordination in locomotion control," *Int. J. Rob. Res.*, vol. 37, no. 10, pp. 1253-1268, 2018.

[93] M.whit, J. Whitman, P. Schiebel, D. Goldman, and H. Choset, "Shape-Based compliance in locomotion," In Proc. of 2016 Robotic Science and System, June 18 - June 22, Ann Arbor, Michigan, USA, 2016.

[94] Kousuke Inoue, Takaaki Sumi, and Shugen Ma, "CPG-based control of a simulated snake-like robot adaptable to changing ground friction," In Proc. 2007 IEEE/RSJ International Conference on Intelligent Robots and Systems, 29 Oct-2 Nov, San Diego, CA, USA, pp. 1957–1962, 2007.

[95] G. Li, H. Zhang, J. Zhang, and R. T. Bye, "Development of adaptive locomotion of a caterpillar-like robot based on a sensory feedback CPG model," *Adv. Robot.*, vol. 28, no. 6, pp. 389–401, 2014.

[96] I. Tanev, T. Ray, and A. Buller, "Automated evolutionary design, robustness, and adaptation of sidewinding locomotion of a simulated snake-like robot," *IEEE Trans. Robot.*, vol. 21, no. 4, pp. 632–645, 2005.

[97] L. T. Martins, C. A. Arend Tatsch, E. H. Maciel, R. Gerndt, and R. da Silva Guerra,

"A Polyurethane-based Compliant Element for Upgrading Conventional Servos into Series Elastic Actuators," *IFAC-PapersOnLine*, vol. 48, no. 19, pp. 112–117, 2015.

[98] G. Li, W. Li, J. Zhang, and H. Zhang, "Analysis and Design of Asymmetric Oscillation for Caterpillar-Like Locomotion," *J. Bionic Eng.*, vol. 12, no. 2, pp. 190–203, 2015.

[99] G. A. Pratt and M. M. Williamson, "Series elastic actuators," In Proc. 1995 IEEE/RSJ International Conference on Intelligent Robots and Systems. Human Robot Interaction and Cooperative Robots, 5-9 Aug, Pittsburgh, PA, USA, USA, pp. 399–406, 1995

[100] Y. Zhao, N. Paine, S. J. Jorgensen, and L. Sentis, "Impedance Control and Performance Measure of Series Elastic Actuators," *IEEE Trans. Ind. Electron.*, vol. 65, no. 3, pp. 2817–2827, 2018.

[101] D. Accoto, G. Carpino, F. Sergi, N. L. Tagliamonte, L. Zollo, and E. Guglielmelli, "Design and Characterization of a Novel High-Power Series Elastic Actuator for a Lower Limb Robotic Orthosis," *Int. J. Adv. Robot. Syst.*, vol. 10, no. 10, p. 359, 2013.

[102] W. Roozing, "Modeling and Control of Adjustable Articulated Parallel Compliant Actuation Arrangements in Articulated Robots," *Front. Robot. AI*, vol. 5, p. 4, 2018.

[103] M. W. Spong, S. Hutchinson, and M. Vidyasagar, *Robot Dynamics and Control*., John Wiley & Sons, Inc., New York, USA, 2004.

[104] M. Vespignani, K. Melo, S. Bonardi, and A. J. Ijspeert, "Role of compliance on the locomotion of a reconfigurable modular snake robot," In Proc. 2015 IEEE/RSJ International Conference on Intelligent Robots and Systems (IROS), 28 Sept.-2 Oct, Hamburg, Germany, pp. 2238–2245, 2015.

[105] A. Kandhari, Y. Huang, K. A. Daltorio, H. J. Chiel, and R. D. Quinn, "Body stiffness in orthogonal directions oppositely affects worm-like robot turning and straight-line locomotion," *Bioinspir. Biomim.*, vol. 13, no. 2, p. 026003, 2018.

[106] Z. Wang, S. Ma, B. Li, and Y. Wang, "Dynamic modeling for locomotion-manipulation of a snake-like robot by using geometric methods," In Proc. 2009

IEEE/RSJ International Conference on Intelligent Robots and Systems (IROS), 10-15 Oct, St. Louis, MO, USA, pp. 3631-3636, 2009.

[107] R. Lewandowski and B. Chorążyczewski, "Identification of the parameters of the Kelvin–Voigt and the Maxwell fractional models, used to modeling of viscoelastic dampers," *Comput. Struct.*, vol. 88, no. 1–2, pp. 1–17, 2010.

[108] M. W. Spong, "Modeling and Control of Elastic Joint Robots," *J. Dyn. Syst. Meas. Control*, vol. 109, no. 4, p. 310, 1987.

[109] S. Nicosia and P. Tomei, "A PD Control Law for Trajectory Tracking of Flexible Joint Robots," *IFAC Proc. Vol.*, vol. 24, no. 9, pp. 357–362, 1991.

[110] W. Yin, L. Sun, M. Wang, and J. Liu, "Position control of Series Elastic Actuator based on feedback linearization and RISE method," in *2016 IEEE International Conference on Robotics and Biomimetics (ROBIO)*, 3-7 Dec, Qingdao, China, pp. 1203–1208, 2016.

[111] C. Gong, M. Tesch, D. Rollinson, and H. Choset, "Snakes on an inclined plane: Learning an adaptive sidewinding motion for changing slopes," In Proc. 2014 IEEE International Conference on Intelligent Robots and Systems, 4-18 Sept, Chicago, IL, USA, pp. 1114-1119, 2014.

[112] H. Geyer, A. Seyfarth, and R. Blickhan, "Compliant leg behaviour explains basic dynamics of walking and running.," *Proceedings. Biol. Sci.*, vol. 273, no. 1603, pp. 2861–7, Nov. 2006.

[113] J. W. Hurst, "The role and implementation of compliance in legged locomotion," P.h.D. thesis, Carnegie Mellon University, The Robotics Institute, Pittsburgh, Pennsylvania, USA, 2008.

[114] A. Calanca, R. Muradore, and P. Fiorini, "Impedance control of series elastic actuators: Passivity and acceleration-based control," *Mechatronics*, vol. 47, pp. 37–48, 2017.

[115] A. Calanca, R. Muradore, and P. Fiorini, "A Review of Algorithms for Compliant Control of Stiff and Fixed-Compliance Robots," *IEEE/ASME Trans. Mechatronics*,

vol. 21, no. 2, pp. 613–624, 2016.

[116] C. Ott, R. Mukherjee, and Y. Nakamura, "Unified Impedance and Admittance Control," In Proc. 2010 IEEE International Conference on Robotics and Automation *(ICRA)*, 3-7 May, Anchorage, AK, USA, pp. 554–561, 2010.

[117] Y. J. Kim, M. C. Lin, and D. Manocha, "Collision Detection," in *Humanoid Robotics: A Reference*, Springer, Dordrecht, Netherlands, pp. 1–24, 2017.

[118] T. Kano, T. Sato, R. Kobayashi, and A. Ishiguro, "Local reflexive mechanisms essential for snakes' scaffold-based locomotion," *Bioinspir Biomim*, vol. 7, no. 4, p. 46008, 2012.

[119] J. R. Taylor, *An introduction to error analysis : the study of uncertainties in physical measurements*. University Science Books, Sausalito, CA, USA, 1997.